

**I. TEMPERATURES OF POLAR ICE DEPOSITS
ON MERCURY AND THE MOON**

**II. JOVIAN ATMOSPHERIC DYNAMICS
FROM GALILEO IMAGING**

Thesis by

Ashwin R. Vasavada

In Partial Fulfillment of the Requirements

for the Degree of

Doctor of Philosophy

California Institute of Technology

Pasadena, California

1998

(Submitted May 18, 1998)

© 1998

Ashwin R. Vasavada

All rights reserved

Philosophy is written in this grand book -- I mean the universe -- which stands continually open to our gaze, but it cannot be understood unless one first learns to comprehend the language and interpret the characters in which it is written. It is written in the language of mathematics, and its characters are triangles, circles, and other geometrical figures, without which it is humanly impossible to understand a single word of it; without these, one is wandering about in a dark labyrinth.

- Galileo Galilei, *Il Saggiatore*

The heavens are telling the glory of God;
 And the firmament proclaims his handiwork.
 Day to day pours forth speech,
 And night to night declares knowledge.
 There is no speech, nor are there words;
 Their voice is not heard;
 Yet their voice goes out through all the earth,
 And their words to the end of the world.

- from *Psalms 19* (RSV)

When I heard the learned astronomer,
 When the proofs, the figures, were ranged in columns before me,
 When I was shown the charts and diagrams to add,
 divide and measure them,
 When I sitting heard the astronomer where he lectured
 with much applause in the lecture room,
 How soon unaccountable I became tired and sick,
 Till rising and gliding out I wandered off by myself
 In the mystic moist night air, and from time to time,
 Looked up in perfect silence at the stars.

- Walt Whitman, *Leaves of Grass*

Dedicated to the natural philosopher, the priest,
 and the poet -- may we one day share our wonder.

Acknowledgments

The five years I've studied at Caltech have been fast and furious. The intensity of the people and the research here at times has left me exasperated and overburdened, but at other times has brought me great satisfaction and humility. Many people deserve abundant thanks for pushing, pulling, and guiding me through.

I must first thank my parents, whose high expectations were surpassed only by their love and support. Thanks to my sister for being my family in Los Angeles. I credit Andy Ingersoll, my thesis advisor at Caltech, and David Paige, my advisor as an undergraduate at UCLA, with much of who I am as a scientist. Both had unrelenting confidence in me and both pushed me out on the front lines, giving me opportunities to grow inwardly and among the scientific community. Thanks, Dave, for encouraging me to run off to Caltech. Thanks, Andy, for taking me in. During my graduate career, I've also benefited greatly from the insight and prodding of Bruce Murray (thanks for Japan!), the genuine counsel of Dewey Muhleman, and the practical advice of Mike Brown.

I'm indebted to several people for contributing to my research. It's been a pleasure to work with Eric de Jong, a dedicated and generous friend of planetary science. Thanks to Mike Belton for welcoming me among the Galileo SSI Team, and to Peter Gierasch and Don Banfield for collaborating. It's been enriching and fun to work with the "Jupiter Group": James Cho, Adam Showman, and Sarah Stewart. Kay Campbell, Irma Better, and Tammie Henderson deserve countless

thanks for all their administrative help. Thank you, Mike Black, for your friendly and speedy answer to every computing problem -- you are the unsung hero of our option, not to mention the sub-basement.

And finally, many people have made my life outside of research (those few precious minutes) so enjoyable. Thanks to my officemates Hari, Jim, Dave, Liz, Lori, and Charlie. Thanks to my faithful friends and roommates, Craig, Bill, and Stan, and my friends from home. Thanks to the UCLA crew (Steve, Mark, Leslie, Momi, Karen, Asmin, and Debbie) for keeping in touch. A special thanks to the 3:30 coffee break crowd, including Mark, Anton, and Anthony, for the vast improvement to the social atmosphere. Thanks to Bill Bing for your commitment to the Caltech Concert Band. Thanks to Albert and Mary for the food and flying. Finally, thanks to Lee Silver and Bob Sharp for your infectious love of geology, and to Dave Stevenson for two incredible backpacking trips.

Abstract

Locations on Mercury that produce ice-like radar responses lie within impact craters that have very cold, permanently shaded floors. The retention of possible ice deposits is determined largely by their temperature. We present model-calculated temperatures of flat surfaces and surfaces within bowl-shaped and flat-floored polar impact craters. Our model includes appropriate insolation cycles, realistic crater shapes, multiple scattering of sunlight and infrared radiation, and depth and temperature-dependent regolith thermophysical properties. Unshaded water ice deposits are rapidly lost to sublimation on Mercury and the Moon. Meter-thick deposits of water ice are stable to evaporation over the age of the solar system if located in the permanently shaded portions of flat-floored craters within 10° latitude of the poles of either planet. Results for craters associated with radar features on Mercury are consistent with stable water ice deposits if a thin regolith layer thermally insulates the lowest latitude deposits, reducing sublimation rates. A regolith cover also is a diffusion barrier, reduces losses from sputtering, impact vaporization, and exposure to $H\ Ly\alpha$, and is implied independently by the radar observations. Impact craters near the lunar poles contain colder permanently shaded regions than those on Mercury.

During the first six orbits of the Galileo spacecraft's prime mission, the Solid State Imaging system acquired multispectral image mosaics of Jupiter's Great Red Spot, an equatorial belt/zone boundary, a "5- μm hotspot" similar to the Galileo Probe entry site, and two of the classic White Ovals. We present mosaics

of each region approximating their appearance at visible wavelengths and showing cloud height and opacity variations. The local wind field is derived by tracking cloud motions between multiple observations of each region with time separations of roughly one and ten hours. Vertical cloud structure is derived in a companion paper by Banfield *et al.* (1998). Galileo's brief, high-resolution observations complement Earth-based and Voyager studies, and offer local meteorological context for the Galileo Probe results. Images taken one hour apart reveal small, rapidly changing, high cloud features possibly analogous to terrestrial thunderstorms. Our results show that the dynamics of the zonal jets and large vortices have changed little since Voyager, with a few exceptions. We detect a cyclonic current within the center of the predominantly anticyclonic Great Red Spot. The zonal velocity difference between 0°S and 6°S has increased by 20 m s^{-1} . We measure a strong northeast flow approaching the hotspot. This flow indicates either massive horizontal convergence or the presence of a large anticyclonic vortex southeast of the hotspot. The current compact arrangement of two White Ovals and a cyclonic structure greatly perturbs the zonal jets in that region.

Table of Contents

Acknowledgments	iv
Abstract	vi
Chapter 1 Preface	1
Chapter 2 Temperatures of Polar Ice Deposits on Mercury and the Moon	5
I. Introduction and Background	6
II. Thermal Modeling	11
A. Temperatures of Flat Surfaces: 1-D Thermal Model	11
B. Temperatures of Flat Surfaces: Model Results	14
C. Temperatures within Impact Craters: Motivation	20
D. Temperatures within Impact Craters: Scattering Model	24
E. Temperatures within Impact Craters: Results	26
III. Application to the Stability of Ice Deposits	27
A. Temperatures of Flat Surfaces	27
B. Temperatures within Impact Craters	34
C. Comparison with Radar Features on Mercury	49
IV. Subsurface Ice Deposits	52
A. Thermal Protection for Low-Latitude Deposits	52
B. Compatibility with Radar Observations	54
C. Deposition and Burial	55
V. Ice Deposits on Mercury and the Moon	56
VI. Conclusions	59
References	61
Chapter 3 Jovian Atmospheric Dynamics from Galileo Imaging	67
I. Introduction	68
II. Methods of Observation and Analysis	69
A. Imaging Strategy for Jupiter's Atmosphere	69
B. Photometric Calibration, Navigation, and Mapping	70
C. True and False Color Mosaics	74
D. Measuring Wind Velocities	78
III. Appearance and Dynamics	80
A. The Great Red Spot	80
B. The Southern Equatorial Region	86
C. The Northern Equatorial Region	91
D. The White Ovals	95
IV. Discussion and Conclusions	96
References	101

1. PREFACE

Planetary Science is a collection of research loosely unified by its focus on solar system objects and processes. That definition leaves open a broad “parameter space” from which researchers choose their subject and approach. Within that space, my research projects would lie scattered between theoretical modeling and data analysis, surfaces and atmospheres, and Mercury, Earth, the Moon, Mars, and Jupiter. My interests, including the two projects that are described in this thesis, are not easily unified by a theme or technique. Instead, my choice of topics has been opportunistic, reflecting another facet of Planetary Science. The result is a somewhat unconventional thesis containing two unrelated projects addressed with quite different techniques and from quite different viewpoints. The first is a theoretical study of a phenomenon poorly constrained by observations. The second is an analysis of an observed process poorly constrained by theory. In the latter case, my contributions were weighted towards acquiring and reducing the observations themselves. Because each section includes specific background material, I will use the present section to briefly describe the opportunities that led me to study these topics, and their broader scientific scope.

In 1991, the Goldstone-Very Large Array radar experiment led by Martin Slade of the Jet Propulsion Laboratory detected anomalous bright and depolarized echoes from the south pole of Mercury. Their favored explanation of the radar response was the presence of meter-thick water ice deposits hidden in the permanent shadows of polar topography. The relative abundance of water in the

solar system and the extremely slow evaporation rate from a polar cold trap led Caltech researchers to propose as early as 1961 that such deposits may exist on the Moon's poles. The abundance and composition of ice deposits on Mercury or the Moon are important clues towards understanding the rates of volatile delivery and loss in the inner solar system, planetary outgassing, and changes in the planet's orbital elements.

The temperatures of possible polar cold traps are key pieces of information. Because the evaporation rates of ices are strong functions of temperature, knowing the temperature of a cold trap helps limit the composition and age of an ice deposit within it. Because a condensable volatile delivered to a planet's surface will migrate to the coldest available locations, the warmest temperature at which a deposit is observed is a measure of the abundance of that volatile and the availability of possible niches. Temperatures within permanently shaded areas near the poles of Mercury or the Moon currently cannot be measured from Earth or spacecraft, so they are derived using theoretical models. The model described in the next chapter is the state-of-the-art for calculating the temperatures within the permanently-shaded portions of polar impact craters on Mercury and the Moon. I use it to understand the temperature and latitudinal extent of possible cold traps on both planets and to interpret the observed radar features on Mercury. Stephen Wood and Prof. David Paige of UCLA helped define the approach I took when building the model.

With the loss of Mars Observer in 1993, it became apparent that the Galileo mission to Jupiter would be the only major spacecraft mission during my tenure at Caltech. Determined to work with planetary remote sensing data, I took an offer from Andy Ingersoll to help with the analysis of images of Jupiter's atmosphere. The limited downlink rate from Galileo's low-gain antenna significantly restricted the breadth and size of the imaging dataset. Several small regions containing interesting atmospheric features were imaged with spatial, spectral, and temporal resolutions meeting or exceeding those of the Voyager missions. My participation began in December 1995, six months before the start of the orbiter mission. Throughout the last few years, I have devoted a significant fraction of my time towards the planning and processing of the imaging sequences. Because of my interest in deriving winds by precisely tracking the movements of clouds, I became an expert at deriving camera pointing and creating image mosaics. This skill also has helped to constrain the locations of jovian lightning and aurora at visible wavelengths, the latter in three dimensions.

Jovian atmospheric dynamics is a difficult fluid dynamics problem. Unlike thermal modeling, for example, the physics of giant planet atmospheres is still being developed by theorists. The application of theory to observation is limited by the poorly understood relationship between the observed, two-dimensional cloud motions and the planet's interior. First-order questions have yet to be answered: What is the source of energy driving the zonal jets and vortices? How is energy transferred horizontally (e.g., between jets) or vertically? What processes can

account for the variation of certain spots and bands on the order of minutes and also the stability of jets and large vortices over many years? The Galileo imaging data cannot fully answer these questions, but they do provide a new set of clues. The second half of this thesis describes techniques and results of my wind determinations for the first half of Galileo's primary mission. I compare my results to Voyager measurements and describe new phenomenon revealed by the greater time resolution and spectral coverage of Galileo's camera. The large author list includes Galileo imaging team members and operations staff because I completed this work using proprietary data.

**2. TEMPERATURES OF POLAR ICE DEPOSITS
ON MERCURY AND THE MOON**

To be submitted to the *Journal of Geophysical Research* as:

Vasavada, A. R., S. E. Wood, and D. A. Paige 1998. Temperatures
of polar ice deposits on Mercury and the Moon.

I. INTRODUCTION AND BACKGROUND

A relatively old idea in planetary science, that volatiles may be cold trapped in permanently shaded regions near the poles of the Moon and Mercury (Watson *et al.* 1961, Thomas 1974), was revitalized when strong, highly depolarized (circular polarization ratio > 1) radar echoes were received from the poles of Mercury (Slade *et al.* 1992, Harmon and Slade 1992, Butler *et al.* 1993). The anomalous radar response was interpreted to indicate substantial ice deposits by analogy with radar returns from the icy Galilean satellites and Mars' south polar residual ice cap (Goldstein and Morris 1975; Muhleman *et al.* 1991). Water ice is favored because of its relative abundance and thermal stability. The inverted polarization ratio is thought to arise from volume scattering by density variations, voids, or particles within weakly absorbing water ice. The radar beam is deflected 180° by a series of forward scattering events, each of which preserves the sense of polarization. The radar cross section may be enhanced by the coherent backscatter opposition effect (Hapke 1990). Recent observations have shown that terrestrial ice fields produce a similar radar response (Rignot 1995; Haldemann 1997). The exact scattering mechanisms operative in each environment and the physical structures that produce them are still debated (e.g., Hagfors *et al.* 1997).

Two experiments have searched for a similar radar response from the Moon's poles. The Clementine-Deep Space Network bistatic radar experiment claimed to detect a slightly enhanced, slightly depolarized signal from a region near the south pole (Nozette *et al.* 1996). Higher-resolution Arecibo radar observations

found no extensive areas with anomalous radar properties near either pole (Stacy *et al.* 1997). Arecibo did detect ice-like radar properties for several small (~ 1 km) regions, but some of these were in sunlit areas and may be explained better by surface roughness effects. The lunar experiments had a less favorable geometry than the observations of Mercury, but still were capable of probing permanently shaded area. The sub-Earth latitude was $4\text{-}6^\circ$ during the lunar experiments, half that of the Mercury experiments. Including the finite size of the solar disk and each planet's solar obliquity, the edge of the solar disk rises 1.85° above the horizon at the Moon's poles, and 1.6° above Mercury's. Earth-based radar experiments see further into permanently shaded areas on Mercury, but cannot completely probe the polar terrain of either planet. For example, an observer must be 22° above the horizon to see the bottom of a 10 km crater.

Several recent studies have focused on a more detailed understanding of the sources, evolution, and sinks of volatiles (Morgan and Shemansky 1991; Potter 1995; Rawlins *et al.* 1995; Butler 1997; Killen *et al.* 1997). Volatiles are delivered to the surfaces of Mercury and the Moon by impactors and planetary outgassing. Volatiles also are derived from the regolith by impact vaporization, photon-stimulated desorption, and ion sputtering of surface minerals with subsequent chemical reactions. Calculations show that water retained from meteoroid impacts or comet impacts, or water produced through solar wind sputtering alone can produce detectable deposits on either planet. Molecules in sunlit areas will hop in ballistic, collisionless trajectories until lost by photodissociation, photoionization,

other less important exospheric loss processes, or landing in a permanently shaded area. Butler (1997) found comparable timescales for loss by photodestruction and loss by cold trapping for both water and CO₂. Therefore, a fraction of molecules delivered to either planet's surface will survive other loss processes and form polar deposits.

Watson *et al.* (1961) noted that once deposits form, the overall loss rate is no longer controlled by fast exospheric processes, but by the rate of sublimation from the condensed phase. A volatile deposit could survive for an extremely long time if trapped in a sufficiently cold region. Near 112 K, a meter-thick layer of cubic water ice can survive the age of the solar system. Figure 1 shows evaporation rates as a function of temperature for several volatiles. Thermal sublimation dominates other loss processes except at very low temperatures, where loss rates are set by micrometeorite impact vaporization and sublimation from interstellar H Ly α . If covered by a thin regolith layer, deposits would be protected from surface loss processes and peak surface temperatures. Loss would then be controlled by diffusion through the regolith cover. Arguments for deposits composed of volatiles other than cubic water ice can be found in Sprague *et al.* (1995), Butler (1997), and Jenniskens and Blake (1996).

The temperatures of polar surfaces that may act as volatile cold-traps are the key factor that determines where ice deposits will condense, how long deposits will survive, and what their composition may be. Thermal modeling by Paige *et al.* (1992) showed that the temperatures of flat surfaces near Mercury's poles

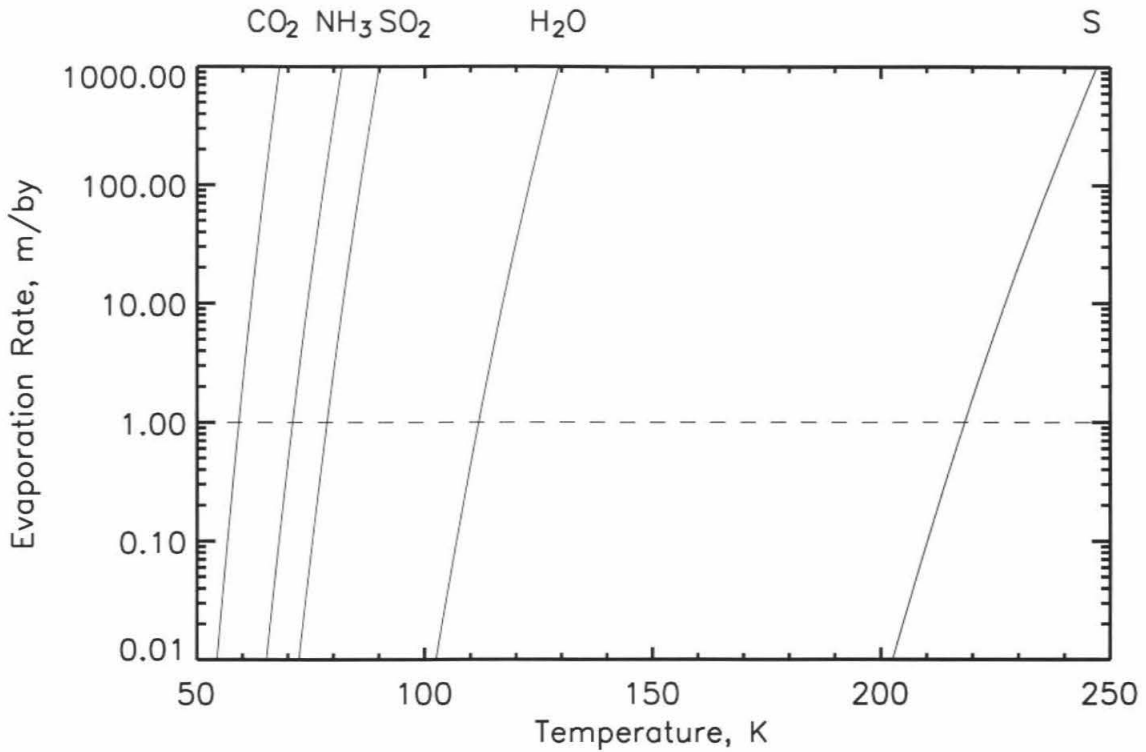


Figure 1. Evaporation rates as functions of temperature for CO₂, NH₃, SO₂, cubic H₂O, and S_α (solid orthorhombic sulfur) ices. Vapor pressure data were taken from the *CRC Handbook of Chemistry and Physics* (Lide 1993), Bryson *et al.* (1974), and Moses and Nash (1991). The calculation of evaporation rates follows Watson *et al.* (1961). The dashed line marks the rate at which a radar-detectable deposit would survive the age of the solar system. The curves cross this line at 59, 71, 78, 112, and 218K.

preclude the stability of exposed water ice deposits (i.e., polar caps) due to high sublimation rates. However, the temperatures within permanently shaded, shallow topographic depressions near the poles permit the stability of meter-thick, cubic water ice deposits over the age of the solar system (Paige *et al.* 1992, Ingersoll *et al.* 1992). Thermal models of the Moon's poles predict that sites capable of sustaining ice deposits should exist there also (Ingersoll *et al.* 1992; Salvail and Fanale 1994).

Arecibo radar maps of Mercury's poles (Harmon *et al.* 1994) place many radar features within polar impact craters observed by Mariner 10. The ice-like radar response of the locations and their correlation with areas of permanent shadow (and thus low temperature) make a compelling case for the presence of ice deposits on Mercury. Previous thermal modeling studies have verified that water ice deposits can survive at these locations. However, the simplifications included in the models, most significantly spherical crater shapes, limit their usefulness when making quantitative comparisons with the radar observations.

In this paper we present a more complete and systematic study of the temperatures near the poles of Mercury and the Moon. We present new model calculations of the surface and subsurface temperatures within bowl-shaped and flat-floored polar impact craters. Our model uses better estimates of surface thermophysical properties and impact crater shapes than previous studies. We also calculate temperatures within craters on Mercury observed to produce anomalous radar responses and within lunar craters recently identified in Clementine imagery

and ground based radar maps. We begin by describing our thermal model for flat surfaces, which then is coupled to a scattering model for impact craters. We then present our results, compare them with the high resolution Arecibo radar maps of Mercury, and discuss several implications for ice deposits on Mercury and the Moon.

II. THERMAL MODELING

A. Temperatures of Flat Surfaces: 1-D Thermal Model

The temperature response of surface and subsurface layers to solar, infrared, and internal energy fluxes is determined by their bulk thermophysical properties, namely their solar albedo, infrared emissivity, density, thermal conductivity, and heat capacity. Previous studies have estimated these properties of the regoliths of Mercury and the Moon from ground based and spacecraft observations and lunar *in situ* and returned sample measurements. The major results are that (i) the near-surface layers on Mercury and the Moon are similar and spatially uniform over large scales, (ii) the mean temperature increases with depth in the top few centimeters because the thermal conductivity is temperature dependent, (iii) the density increases with depth as determined by radio emissions over a range of wavelengths, and (iv) the thermophysical properties change abruptly near the surface, as evidenced by rapid cooling of the uppermost layer just after sunset (or eclipse) followed by slow cooling of the surface during the night. Accordingly, thermal models that best match observations have modeled the regoliths as loosely packed particulate material with temperature and depth-

dependent thermophysical properties (Linsky 1966; Morrison 1970; Keihm and Langseth 1973; Cuzzi (1974); Mitchell and de Pater 1994 and references therein).

Mitchell and de Pater (1994) constructed a 2-layer model that is largely consistent with the variety of lunar measurements and the radiometry of Mercury's surface from Mariner 10. Their model consists of a 2-cm thick top layer that is highly insulating and a lower layer that is more dense and conductive. Thermal radiation between grains, which is strongly temperature dependent, is the dominant form of heat transfer in the top layer at temperatures above ~ 350 K. Solid (phonon) conduction within and between grains dominates in the lower layer. The sizes and packing of grains can account for difference between layers in the dominant form of heat transfer, so a difference in composition is not required. The widespread presence of this stratigraphy can be explained by ubiquitous micrometeorite bombardment that churns the top layer and compresses the lower layer.

Our model, like the model of Mitchell and de Pater (1994), consists of two layers that differ in thermal conductivity and bulk density. The top layer extends from the surface to a depth of 2 cm and has a bulk density of 1300 kg m^{-3} . The lower layer has a bulk density of 1800 kg m^{-3} . The thermal conductivity has the form $k(T) = k_c[1 + \chi(T/350)^3]$, where T is temperature, k_c is the solid conductivity, and χ is the ratio of radiative to solid conductivity at a temperature of 350 K. We chose values of k_c and χ that best represent the range of measured and derived values. Our top layer has the values of a lunar regolith sample from Apollo 12,

with $k_c = 9.22 \times 10^{-4} \text{ W m}^{-1} \text{ K}^{-1}$ and $\chi = 1.48$ (Cremers and Birkebak 1971). Following Mitchell and de Pater (1994), the bottom layer has $k_c = 9.3 \times 10^{-3} \text{ W m}^{-1} \text{ K}^{-1}$ and $\chi = 0.073$. The lower value of χ is primarily due to the larger solid conductivity. In general, radiative heat transfer is less important at depth because the subsurface does not experience the extreme daytime surface temperatures. The temperature dependence of the heat capacity is taken from Ledlow *et al.* (1992). They derived an expression based on lunar sample measurements but applicable to the range of temperatures on Mercury. We assume an albedo of 0.10 and an infrared emissivity of 0.95. The internal heat fluxes of Mercury and the Moon are assumed to be 0.020 W m^{-2} (Schubert *et al.* 1988) and 0.033 W m^{-2} (Langseth *et al.* 1972; 1976), respectively. The albedo, emissivity, and internal heat fluxes are both uncertain and spatially variable. However, reasonable variations in them do not significantly change our calculated temperatures.

We use a time-stepping, finite-difference model to solve the thermal diffusion equation in one dimension. Depending on the assumed thermophysical properties, between 12-30 model layers are used to resolve the shape and depth of the thermal wave in the subsurface. The orbital position and orientation of the planet is updated at each timestep. The size of the solar disk and darkening of the solar limb follow the formulations of Allen (1973). The temperature of the surface (extrapolated from the top three layers to the actual surface using a second-order scheme) is determined by an instantaneous balance of the incident solar, conducted, emitted infrared, and internal energy fluxes. The temperature gradient

at the deepest model layers is forced to equal that produced by the internal heat flux. The model timestep and number of model layers are chosen to resolve the 2-cm physical layer and to extend well below the depth of diurnal temperature variations. The model is run until the bottom layers equilibrate.

B. Temperatures of Flat Surfaces: Model Results

In this section we present model-calculated, surface and subsurface temperatures for Mercury and the Moon. The calculations are relevant for flat surfaces with no energy contribution from surrounding topography. The results constrain the latitude range of surface or subsurface ice deposits unprotected by shadowing (true polar caps). We ran our 2-layer model with the thermophysical properties described above (Model I). In order to cover the range of possible surface properties, we also ran 1-layer models in which all model layers have the properties of the bottom (Model II) or top (Model III) layer of the 2-layer model. All calculations presented in this section neglect the heat flux from the planet's interior. In this case the temperature is constant with depth below the extent of sunlight-driven temperature variations.

Figure 2 shows surface temperature as a function of local time at the equators of Mercury and the Moon. The results of Models I-III are identical during the day, when temperatures are in radiative equilibrium. At night temperatures are determined by the bulk thermal inertia, $(k\rho c)^{1/2}$, of the surface layers. Model II is warmer than Model III throughout the night because of its higher conductivity and density. The 2-layer Model I cools quickly after sunset as

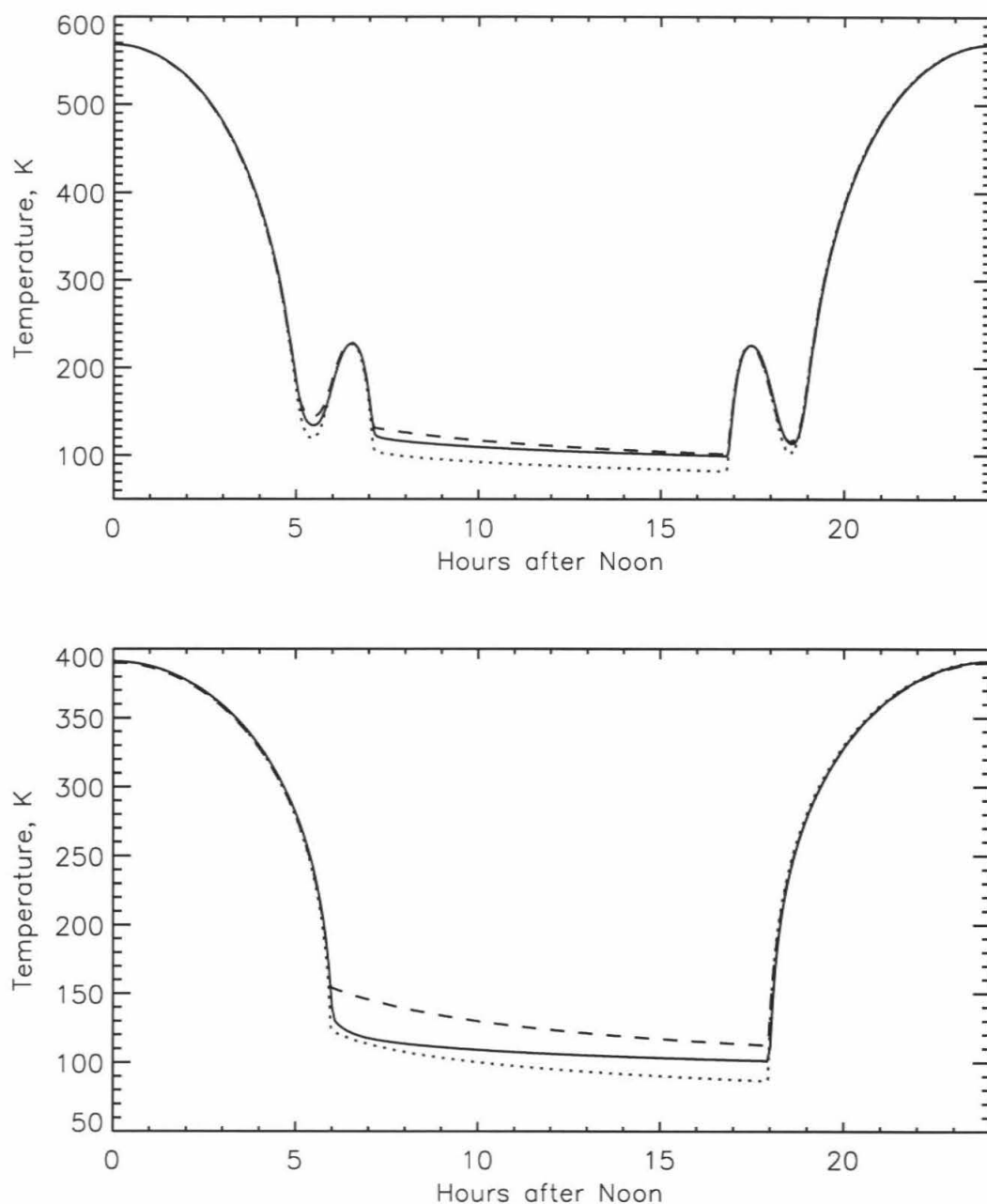


Figure 2. Surface temperature as a function of local time at the equators of Mercury (top) and the Moon (bottom). Results of the 2-layer model (Model I) are plotted as solid lines. The entire surface layer in Model II (dashed) has the thermophysical properties of the bottom layer of the 2-layer model. The entire surface layer in Model III (dotted) has the thermophysical properties of the top layer of the 2-layer model. The Mercury results are for 90°W longitude. During perihelion Mercury's orbital angular velocity briefly exceeds its spin rate, resulting in a brief secondary sunrise and sunset at this longitude.

the top layer loses its heat. Although its bulk thermal inertia is dominated by the lower layer, Model I cools more slowly during the night than Model II because it conducts less efficiently through the top layer and radiates at relatively lower temperatures.

Figure 3 shows the diurnal temperature variation below Mercury's surface at ($0^{\circ}\text{N}, 0^{\circ}\text{W}$) and ($85^{\circ}\text{N}, 0^{\circ}\text{W}$). Because of Mercury's 3:2 spin-orbit resonance, one diurnal period at any point on Mercury's surface is equal to three sidereal days, or two sidereal years, or 176 Earth days. Consequently, longitudes 0° and 180° experience noon at perihelion, while longitudes 90° and 270° experience noon at aphelion. The temperatures of sunlit surfaces are nearly always in radiative equilibrium because of the long diurnal period.

When the radiative (temperature dependent) component of the thermal conductivity is unimportant, such as in Model II, the mean temperature is nearly constant with depth. Heat is conducted with equal efficiency into the subsurface during the day and out of the subsurface at night. When conductivity is a strong function of temperature, such as in Model III, energy conducted downwards along a temperature gradient during the day is released along a larger gradient of opposite sign at night. In this case the mean temperature increases with depth and the equilibrium temperature at depth is accordingly higher. The temperatures at depth in Models II and III are 365 and 463 K, respectively. Below the 2-cm top layer, the temperature profiles of Model I closely resemble those of Model II shifted to higher temperatures by the presence of the top layer. The temperature at

depth in Model I is 427 K, in between that of Models II and III. The top layer significantly affects temperatures at depth even though it is thin compared to the penetration depth of the temperature oscillation.

The temperature variation within the Moon's surface layers has a diurnal and seasonal component. Our lunar model temperatures are output over a span of twelve diurnal periods, or nearly one lunar year. Each diurnal period is 29.5 Earth days. Because the Moon's obliquity with respect to the Sun is only 1.54° , temperatures at low latitudes are determined predominantly by the diurnal period and vary little with season. Temperatures of surfaces very close to the poles have a large seasonal variation.

Figure 4 shows the temperature variation below the Moon's surface at 0°N and 85°N . The increase in mean temperature with depth due to the temperature-dependent conductivity is less prominent than for Mercury because of the lower temperatures on the Moon. Also, temperature oscillations penetrate less deeply into the subsurface because of the shorter diurnal period. The 2-cm top layer is a larger fraction total penetration depth, and temperatures at depth are greatly modified by it. In fact, temperatures at depth in the lunar Model I are very close to those of lunar Model III. The penetration depth of the temperature oscillation is proportional to the square root of the period of the oscillation. The penetration depth increases with latitude on the Moon as the seasonal component of the insolation cycle becomes more significant. At the pole, the temperature oscillation

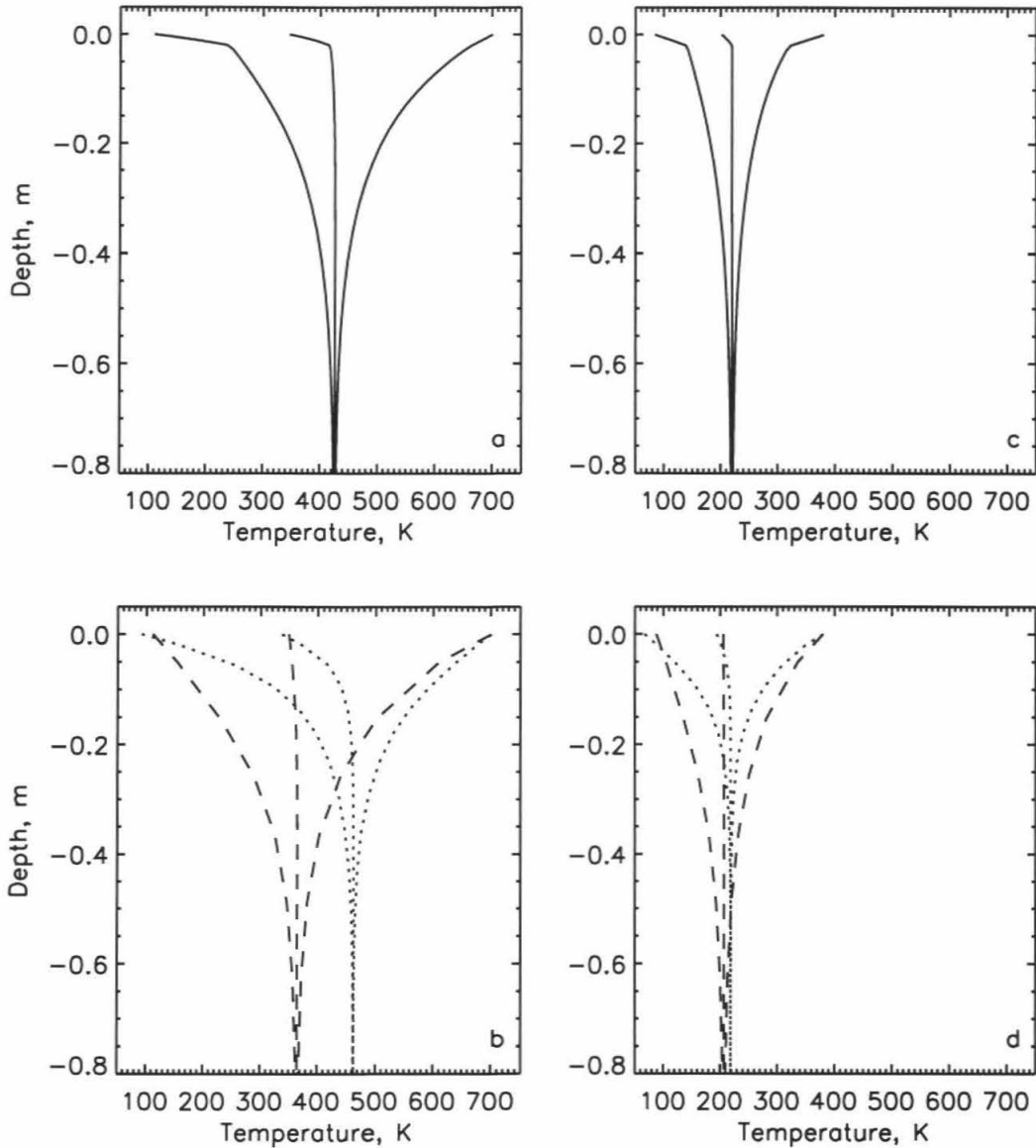


Figure 3. Diurnal minimum, mean, and maximum temperatures as functions of depth on Mercury. These curves represent the extreme and mean temperatures experienced at each depth (they are not instantaneous profiles). (a) Results of our 2-layer model (Model I) at ($0^{\circ}\text{N}, 0^{\circ}\text{W}$). The top, 2-cm layer has a small but strongly temperature-dependent thermal conductivity. The lower layer has a greater conductivity with little temperature dependence. (b) Results from models in which the entire surface layer has the thermophysical properties of the bottom (Model II, dashed) or top (Model III, dotted) layer of the 2-layer model. (c) Model I at ($85^{\circ}\text{N}, 0^{\circ}\text{W}$). (d) Models II and III at ($85^{\circ}\text{N}, 0^{\circ}\text{W}$).

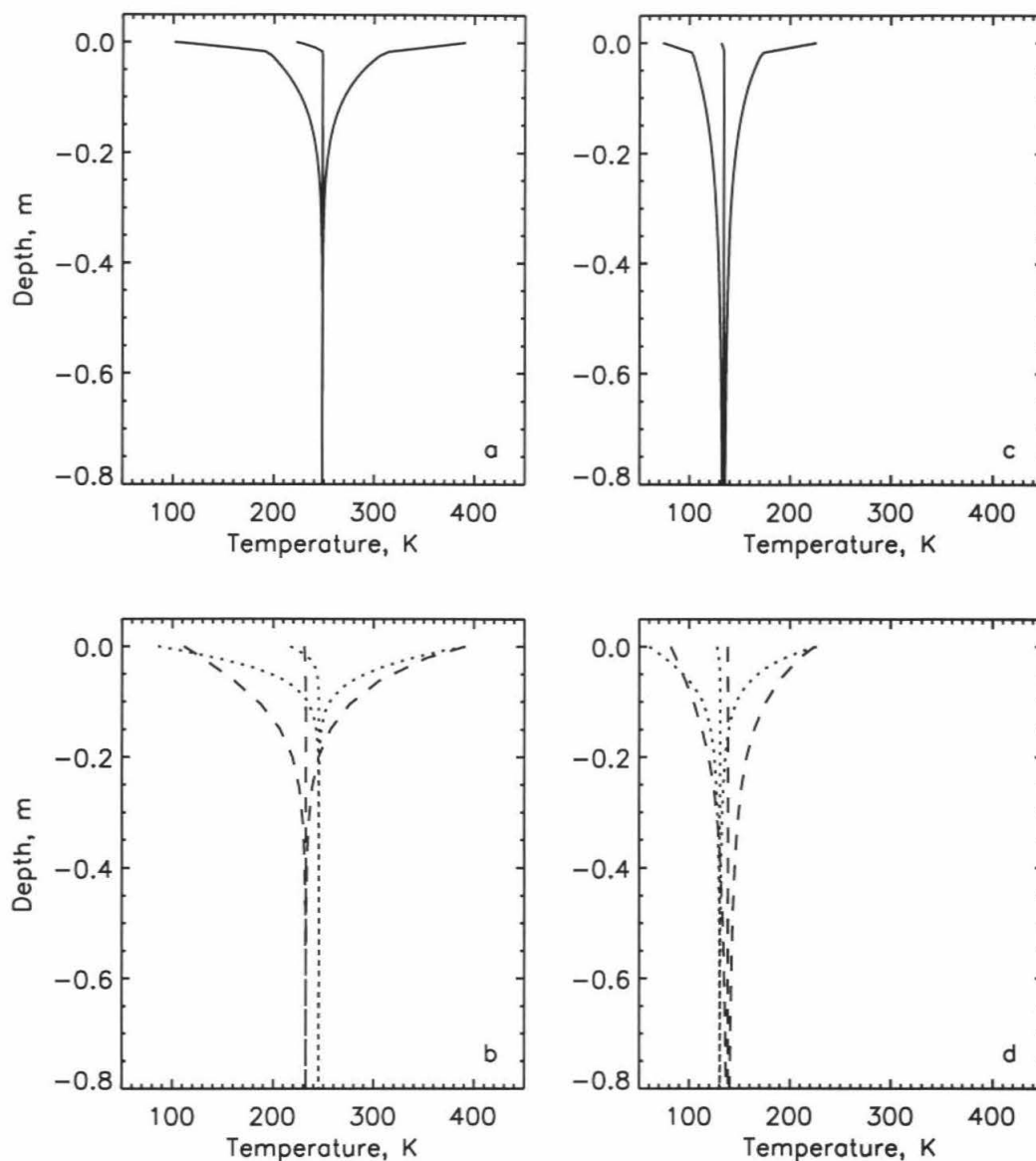


Figure 4. Diurnal minimum, mean, and maximum temperatures as functions of depth on the Moon. These curves represent the extreme and mean temperatures experienced at each depth (they are not instantaneous profiles). (a) Results of our 2-layer model (Model I) at 0°N . The top, 2-cm layer has a small but strongly temperature-dependent thermal conductivity. The lower layer has a greater conductivity with little temperature dependence. (b) Results from models in which the entire surface layer has the thermophysical properties of the bottom (Model II, dashed) or top (Model III, dotted) layer of the 2-layer model. (c) Model I at 85°N . (d) Models II and III at 85°N .

penetrates approximately $12^{1/2}$ or 3.5 times deeper into the regolith than at the equator.

Surface and subsurface temperatures as functions of latitude on Mercury and the Moon are shown in Fig. 5. The maximum surface temperature and the temperature at depth are plotted for Models I-III described above. Maximum surface temperatures are radiative equilibrium temperatures near noon and are independent of surface thermophysical properties for both planets. The results for longitudes 0°W and 90°W on Mercury also represent longitudes 180°W and 270°W , respectively. Because Mercury's eccentricity is large (0.21), the maximum temperature at the equator at 0°W is 130 K higher than that at 90°W . The lunar curves represent all longitudes. Model III has the highest temperatures at depth on Mercury because of the effect of radiative conduction. Differences between models are less at the poles because of overall lower temperatures and smaller diurnal temperature variations. The temperatures at depth for lunar Models I and III are similar because of the greater influence of the 2-cm layer in Model I.

C. Temperatures within Impact Craters: Motivation

We now extend our model to include the effects of topography, specifically impact craters. Positive topography near the poles of a planet with a small obliquity can prevent poleward areas from receiving any direct sunlight. These permanently shaded areas receive only scattered solar and emitted thermal energy from the surrounding topography, and energy from the planet's interior. Permanently shaded surfaces are warmed to the extent that they 'see' hot, sunlit

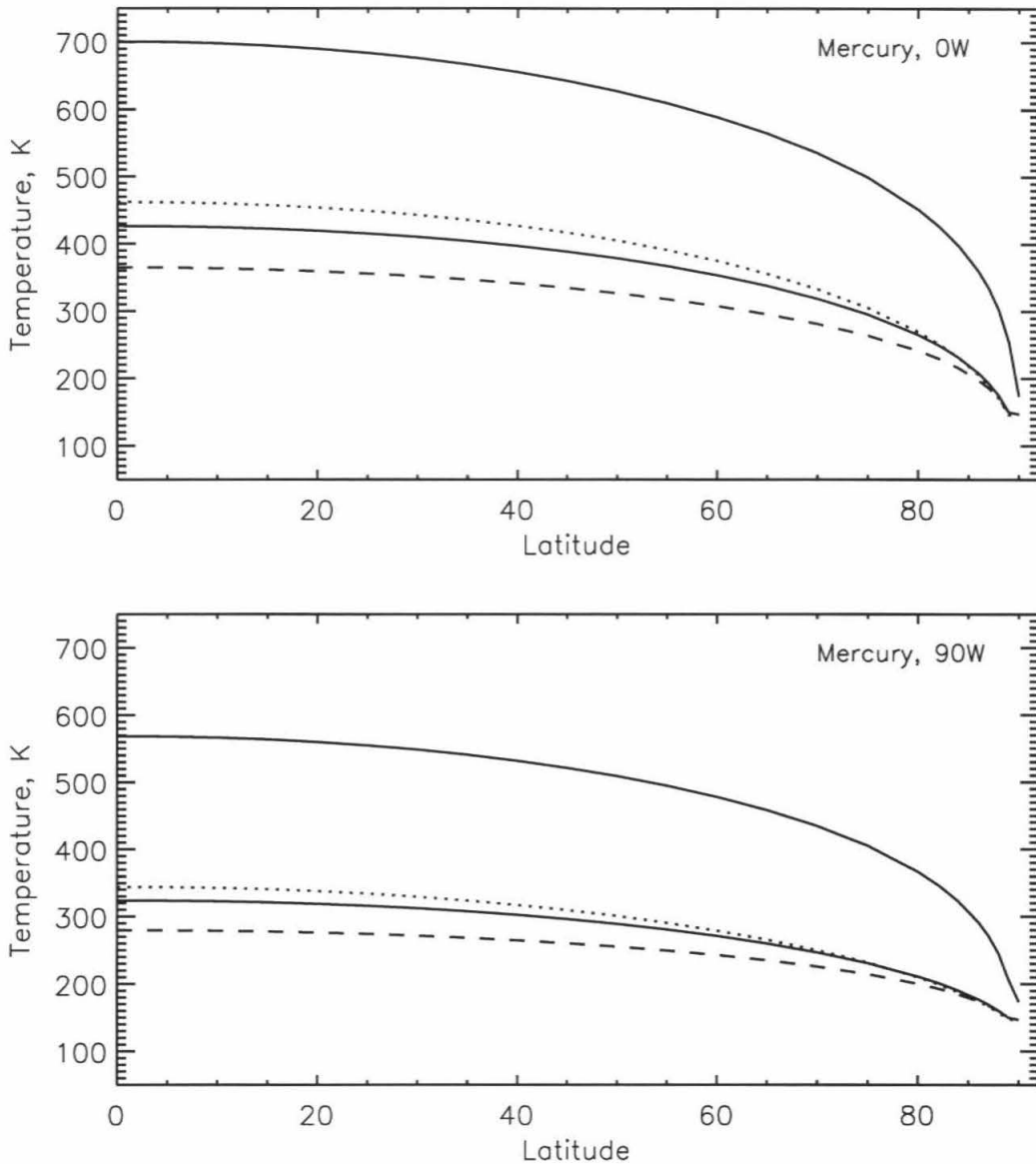


Figure 5a. Maximum surface temperature and temperature at depth as functions of latitude on Mercury. The top and bottom panels represent longitudes on Mercury that experience noon at perihelion and aphelion, respectively. Maximum surface temperatures are radiative equilibrium temperatures at noon and therefore are independent of surface thermophysical properties. Planetary heat flow is neglected, so temperature is constant with depth below the attenuation depth of the surface temperature oscillation. Temperatures at depth are shown for the 2-layer model (Model I, solid), and for models in which the entire surface layer has the thermophysical properties of the bottom (Model II, dashed) or top (Model III, dotted) layer of the 2-layer model.

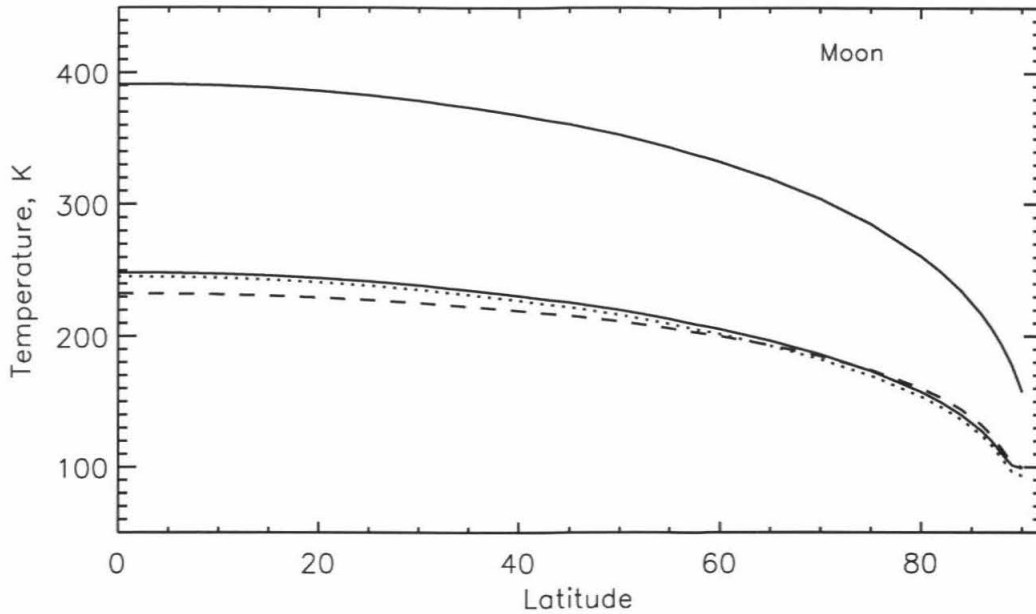


Figure 5b. Maximum surface temperature and temperature at depth as functions of latitude on the Moon. The results are calculated over one year. Maximum surface temperatures are radiative equilibrium temperatures at noon and therefore are independent of surface thermophysical properties. Planetary heat flow is neglected, so temperature is constant with depth below the attenuation depth of the surface temperature oscillation. Temperatures at depth are shown for the 2-layer model (Model I, solid), and for models in which the entire surface layer has the thermophysical properties of the bottom (Model II, dashed) or top (Model III, dotted) layer of the 2-layer model.

areas. Temperatures are therefore sensitive to the orientations of the surface and surrounding topography. We consider the permanently shaded areas within the walls of impact craters because of their association with the radar features on Mercury and the ubiquity of craters on the surfaces of both planets.

The re-distribution of energy within a partially sunlit impact crater takes place within a closed system bounded by the crater walls. Scattering calculations in previous studies were simplified by assuming that impact craters of all sizes were sections of spheres with varying depth-to-diameter ratios (Paige *et al.* 1992, Ingersoll *et al.* 1992). The flux of scattered radiation is constant for all points within such a crater, and the permanently shaded region is isothermal. These calculations showed that water ice is stable to evaporation over billions of years within craters near the poles of Mercury and the Moon, validating the water ice hypothesis. However, the latitudinal extent of the features observed on Mercury is significantly greater than the predictions of these models. A significant source of error in these models is the idealized crater morphology. Only craters with diameters less than 10 km are bowl-shaped. Larger craters have broad, flat floors (Pike 1988) and can have significantly colder permanently shaded regions (Hodges 1980).

In order to calculate the temperatures within craters of arbitrary shape, we have created a finite-element radiative heat transfer model that accounts for the scattering of solar and infrared energy to all orders and coupled it with our flat surface thermal model. The model steps through time, updating the orbital position

and orientation of the planet. The incident solar energy is calculated at each surface element within a bowl-shaped or flat-floored impact crater. We then calculate the multiply-scattered components of the solar energy and the emitted infrared energy. The total energy flux incident on each element is fed into the 1-D thermal model, which is run as described in the previous sections.

D. Temperatures within Impact Craters: Scattering Model

Each impact crater is modeled as a 32×32 square grid of surface elements. The surface area, height, and orientation at the center of each element are calculated from a spherical section for bowl-shaped craters or a truncated cone for flat-floored craters. The depth, floor diameter, rim height, and rim width as a function of crater diameter have been measured from spacecraft images of Mercury and the Moon and are taken from Pike (1988) and Heiken *et al.* (1991), respectively. Craters up to 10 km in diameter have a depth-to-diameter ratio of about 1:5 and are bowl-shaped. Larger craters have relatively more floor area and less steep walls. The depth-to-diameter ratio increases to $\sim 1:25$ for 100-km craters. Craters of a given diameter are slightly shallower on Mercury.

At each timestep, the model finds the direct insolation incident on each element. Elements can be shaded only by the opposite rim of the crater in the direction of the sun. The model accounts for the curvature of the planet when calculating the angle to the horizon (the opposite rim) and the angles between elements. The scattering calculations and resulting temperatures are dependent on the physical size of the crater only through the assumed shape.

Solar and infrared energy scattered between surface elements is calculated following techniques used in thermal engineering and computer graphics for Lambertian surfaces (Siegel and Howell 1981, Goral *et al.* 1984). The energy transferred from surface element i to j can be mathematically described by defining α_{ij} as the fraction of energy emitted by element i that is incident on element j ,

$$\alpha_{ij} = \frac{1}{\pi} \cdot \frac{\cos\theta_i \cos\theta_j dS_j}{d_{ij}^2}$$

where θ_i and θ_j are the angles between the surface normals of elements i and j and the line connecting their centers, d_{ij} is the distance between their centers, and dS_j is the surface area of element j . The factor of $1/\pi$ converts between intensity and flux. If F_j is defined as the flux of energy *leaving* element j , then an equation

$$F_j = A_j \cdot \left(\sum_{i=1}^N F_i \alpha_{ij} + E_j \right)$$

can be written for all $j=1, N$ grid elements inside the crater. When calculating scattered insolation, A_j is the albedo of element j and E_j is the direct insolation incident on element j . When calculating scattered infrared energy, A_j is the infrared emissivity and E_j is the blackbody temperature of element j . Simultaneously solving the N equations yields an F_j for each element. The energy absorbed by each element is F_j/A_j . We employ the iterative Gauss-Seidel method to efficiently reduce the matrix. The factors α_{ij} are calculated only once. The direct insolation, multiply-scattered insolation, and multiply-scattered infrared radiation incident on each

surface element at each timestep are input to a one-dimensional subsurface thermal model.

We validated our scattering model in several ways. Our results for bowl-shaped craters are identical to the analytic solutions of Ingersoll *et al.* (1992) and Paige *et al.* (1992). Our model is a more complete version of Hodges (1980) and produces similar results for lunar flat-floored craters. Temperature results from a model constructed by Salvail and Fanale (1994) are higher than ours and published analytic solutions. One reason may be that they incorrectly used a 59-day diurnal period for Mercury. Doubling the grid size does not change our temperatures. Temperatures are sensitive, of course, to the crater shapes used. A discussion of the errors in the crater shape parameters used can be found in Pike (1988). Other possible sources of error are discussed in a later section.

E. Temperatures within Impact Craters: Results

We modeled 10-km bowl-shaped craters, 40-km flat-floored craters, 100-km flat-floored craters, and specific craters observed near the poles of Mercury and the Moon. For Mercury we modeled the craters observed to contain the radar features that are listed in Harmon *et al.* (1994). We estimated their diameters from Davies *et al.* (1978). Tim Colvin of the RAND Corporation (personal communication) provided new estimates of their locations based on a re-analysis of Mariner 10 imagery (Davies *et al.* 1996). Clementine imagery (Nozette *et al.* 1996) and Arecibo radar maps (Stacy *et al.* 1997) contain the best estimates of the locations of lunar polar craters. Diameters were measured from the Arecibo maps.

Locations were taken from the Arecibo maps after shifting the locations of the lunar poles to match Nozette *et al.* (1996). Recent topographic mapping of the lunar polar regions using delay-Doppler radar techniques (Margot *et al.* 1997) supports the Clementine pole positions (Jean-Luc Margot, personal communication). Craters with degraded rims were excluded. The diameters and locations of all modeled craters are listed in Tables I and II, and shown graphically in Figs. 6 and 7.

Our model output for the 50-km diameter crater C (87.7°N, 171.3°W) on Mercury is shown in Fig. 8 and illustrates features common to many craters. The figure shows the maximum and average temperatures experienced by each surface element over one diurnal cycle. The permanently shaded region is bounded by a steep gradient of both maximum and average temperature. In this example it covers the equatorward interior wall and entire floor of the crater. The coldest surface elements are located on the crater floor adjacent to the equatorward wall.

III. APPLICATION TO THE STABILITY OF ICE DEPOSITS

A. Temperatures of Flat Surfaces

In the following sections we discuss the implications of our thermal modeling results for polar ice deposits. In each case we present the maximum and average surface temperatures over the insolation cycle. Because the vapor pressures of volatiles are exponential functions of temperature, surface loss rates are controlled by maximum temperatures. Average temperatures are relevant for deposits that are protected from extreme daytime temperatures, perhaps by burial

Table I**Diameters and Locations of Mercury's Polar Craters**

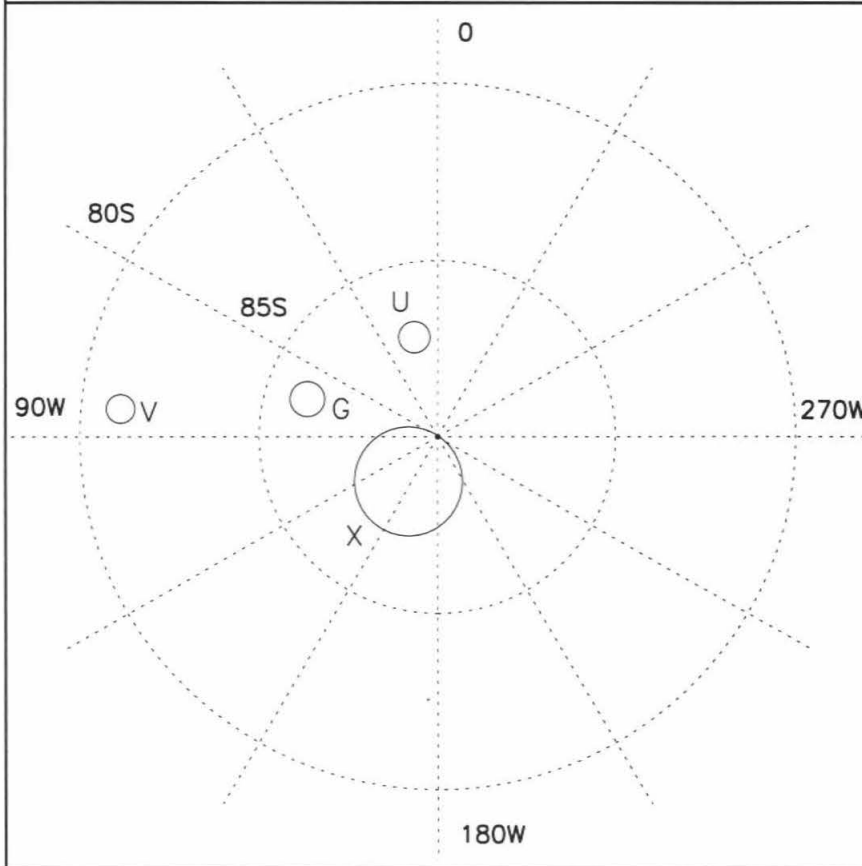
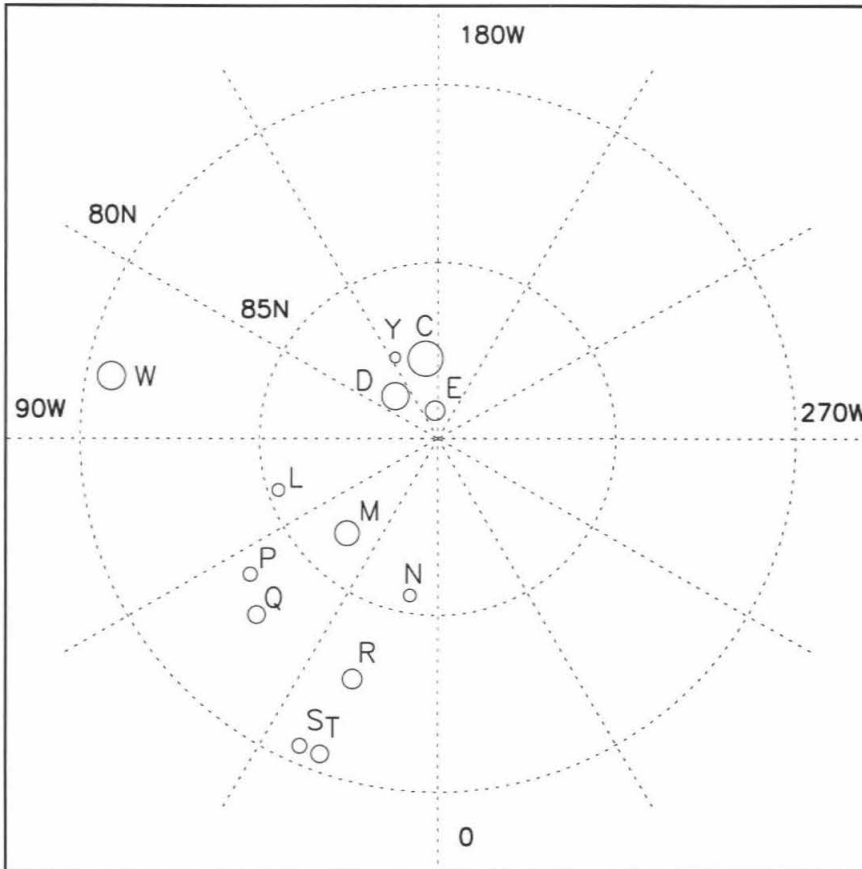
Crater	Diameter (km)	Latitude	Longitude
C	50	87.7 N	171.3 W
D	39	88.3 N	135.4 W
E	28	89.2 N	174.2 W
G	50	86.2 S	73.7 W
L	18	85.3 N	71.9 W
M	35	86.3 N	43.5 W
N	18	85.5 N	10.0 W
P	20	83.5 N	53.9 W
Q	25	82.9 N	45.6 W
R	28	82.8 N	19.4 W
S	21	80.5 N	24.0 W
T	25	80.5 N	20.3 W
U	45	87.1 S	13 W
V	41	81.1 S	84.9 W
W	40	80.7 N	101 W
X	155	88.5 S	147.0 W
Y	15	87.4 N	152.6 W

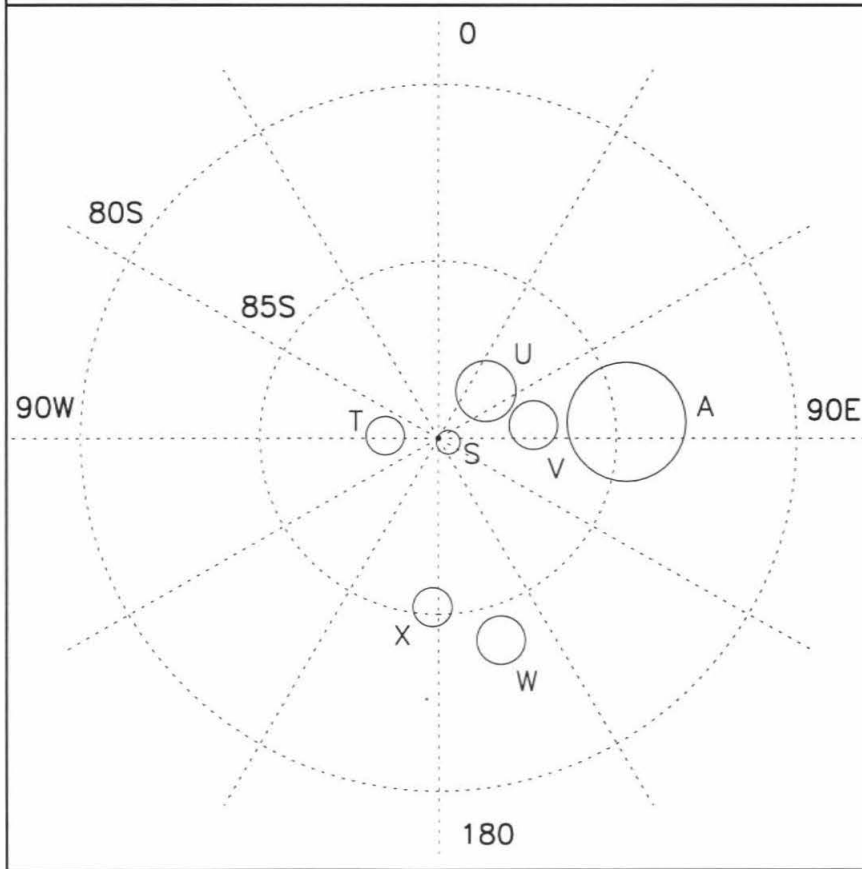
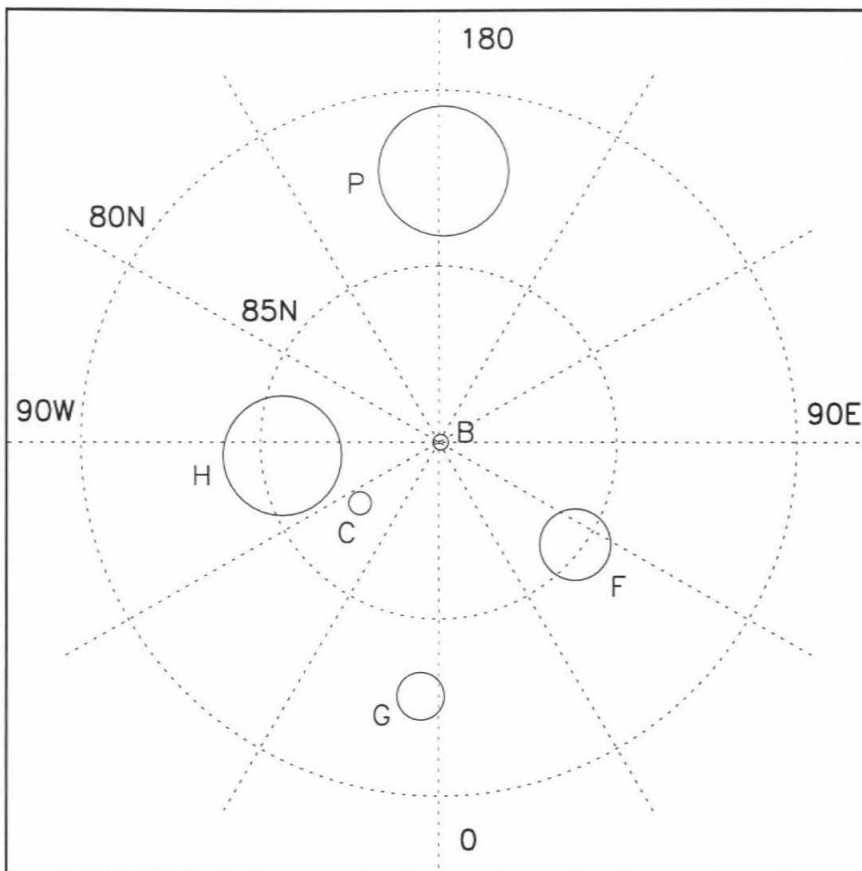
Table II**Diameters and Locations of Lunar Polar Craters**

Crater	Diameter (km)	Latitude	Longitude
A (Amundsen)	100	84.7 S	85 E
B	13	89.9 N	90 E
C	19	87.2 N	52 W
F (Nansen F)	60	85.2 N	53 E
G (Gioja)	40	82.8 N	4 W
H (Hermite)	100	85.6 N	85 W
P (Plaskett)	110	82.3 N	179 E
S (Shackleton)	20	89.7 S	111 E
T	32	88.5 S	87 W
U	51	88.1 S	45 E
V	41	87.3 S	82 E
W (Wiechert)	41	84.0 S	163 E
X	33	85.2 S	178 W

Figure 6 (next page). Locations of impact craters near Mercury's north (top) and south (bottom) poles observed to contain anomalous radar features (Harmon *et al.* 1994). We estimated their diameters from Davies *et al.* (1978). Tim Colvin of the RAND Corporation (personal communication) provided new estimates of their locations based on a re-analysis of Mariner 10 imagery (Davies *et al.* 1996).

Figure 7 (page after next). Locations of impact craters near the Moon's north (top) and south (bottom) poles. Clementine imagery (Nozette *et al.* 1996) and Arecibo radar maps (Stacy *et al.* 1997) contain the best estimates of the locations of lunar polar craters. Diameters were measured from the Arecibo maps. Locations were taken from the Arecibo maps after shifting the locations of the lunar poles to match Nozette *et al.* (1996). Craters with degraded rims were excluded.





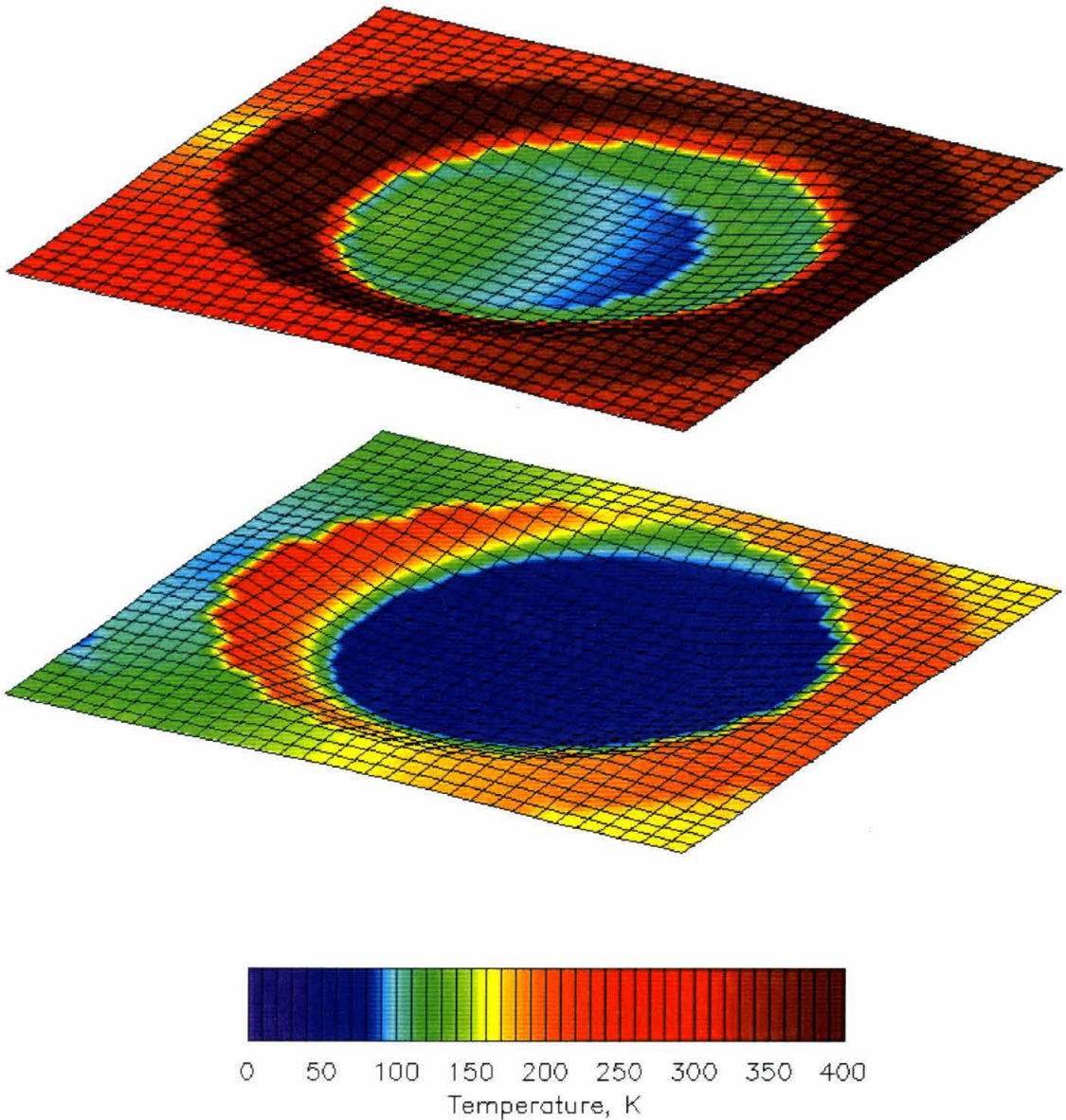


Figure 8. Diurnal maximum (top) and average (bottom) surface temperatures within crater C (87.7N, 171.3W) on Mercury. The colors represent the maximum and average surface temperature of each element over one diurnal cycle. Permanent shadow covers a large fraction of the crater's interior and is bordered by a large gradient in surface temperature. The coldest region is on the crater floor adjacent to the equatorward rim. At noon sunlight comes from the bottom right. North is towards the upper left.

under a regolith layer thicker than the attenuation depth of the surface temperature oscillation (see Section IV).

The results for flat surfaces, shown in Fig. 5, determine whether continuous polar deposits (true polar caps) can exist on or beneath the surfaces of Mercury or the Moon. Thermal sublimation is the primary loss process from condensed ice deposits at all but extremely low temperatures, so we use temperature as a measure of the stability of deposits. Based on the rates shown in Fig. 1, one meter of water ice evaporates in one billion years at a temperature of ~ 112 K. Temperatures of ~ 59 K, ~ 71 K, and ~ 218 K are required to sustain deposits of CO_2 , NH_3 , and S, respectively. The values increase by about 20 K if the timescale is reduced to one million years or if the thickness is increased to 1 km. At the above temperatures, radar-detectable deposits survive the age of the solar system. In addition, Killen *et al.* (1997) estimate that at temperatures less than 112 K, the influx of water from meteorites and asteroids balances or exceeds all losses.

Figure 5 shows that water ice deposits lying exposed on the surface are not stable on either planet. The surface temperatures at the poles are 174 K (Mercury) and 159 K (Moon). A buried water ice deposit is stable within 2° latitude of the lunar pole. Temperatures at the poles below the extent of the temperature oscillation are 147 K (Mercury) and 93 K (Moon). An exposed polar cap composed of sulfur is stable within 1° (Mercury) and 4° (Moon) latitude of the poles, or 4° and 40° if buried.

B. Temperatures within Impact Craters

The maximum and average surface temperatures within impact craters are shown as maps in Figs. 9-13 and plotted as curves in Figs. 14-18. Figure 9 shows the maximum and average surface temperatures within 10-km bowl-shaped craters on Mercury and the Moon for latitudes 70° - 90° . Figures 10 and 11 are similar maps for 40-km and 100-km flat-floored craters. Figures 12 and 13 show our results for specific craters near the poles of Mercury and the Moon. Figures 14-18 present our results in a way that better addresses the thermal stability of ice deposits. Figures 14 and 15 show the diurnal maximum and average temperature experienced by the *coldest* surface element within craters on Mercury. Figures 16 and 17 are similar plots for craters on the Moon. Flat surface temperatures are shown for comparison.

We use Model III for all crater calculations in order to save computing time (the 2-layer model requires a much smaller timestep which makes it prohibitively expensive). The choice of Model III is justified by its small difference from Model I at low temperatures and its relevance for calculating temperatures below a thin regolith cover. To further reduce computing time, temperatures within lunar craters are calculated over one diurnal period at summer solstice and perihelion. The maximum temperatures are the same as if calculated over the full seasonal cycle, but the average temperatures are too large within $\sim 2^{\circ}$ latitude of the pole. A correction can be estimated by comparing the flat surface curves in Fig. 17 with those of Fig. 5. Calculations for hypothetical craters were performed at 0° longitude. Because the internal heat flux is important at the low temperatures

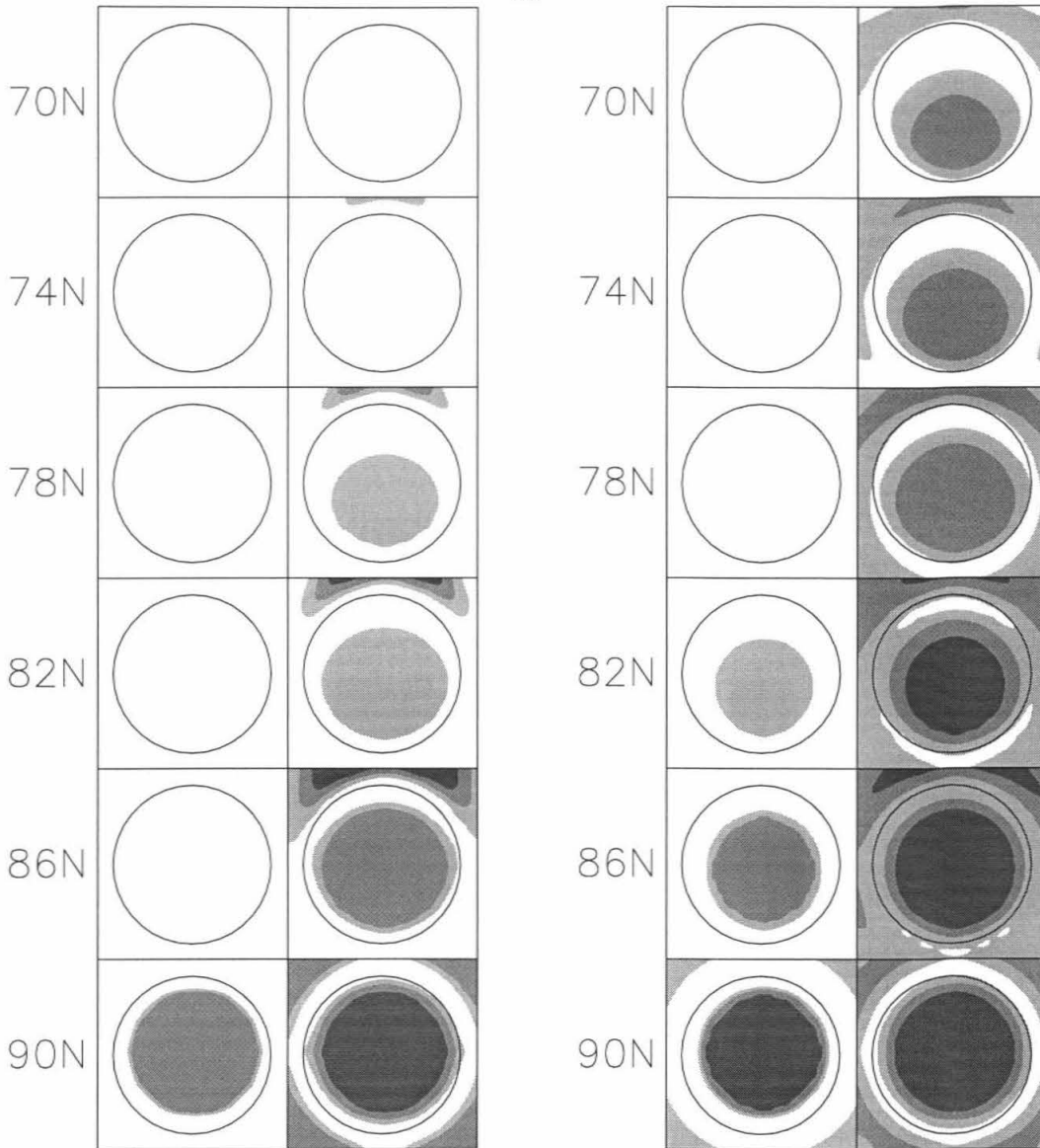
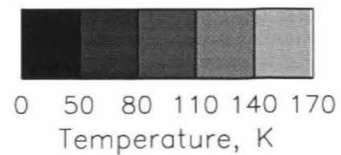


Figure 9. Diurnal maximum and average surface temperatures within 10 km bowl-shaped craters on Mercury (left set of columns) and the Moon (right set of columns). The left column of each set shows maximum temperatures. The right column of each set shows average temperatures. The crater rim is drawn as a solid line.



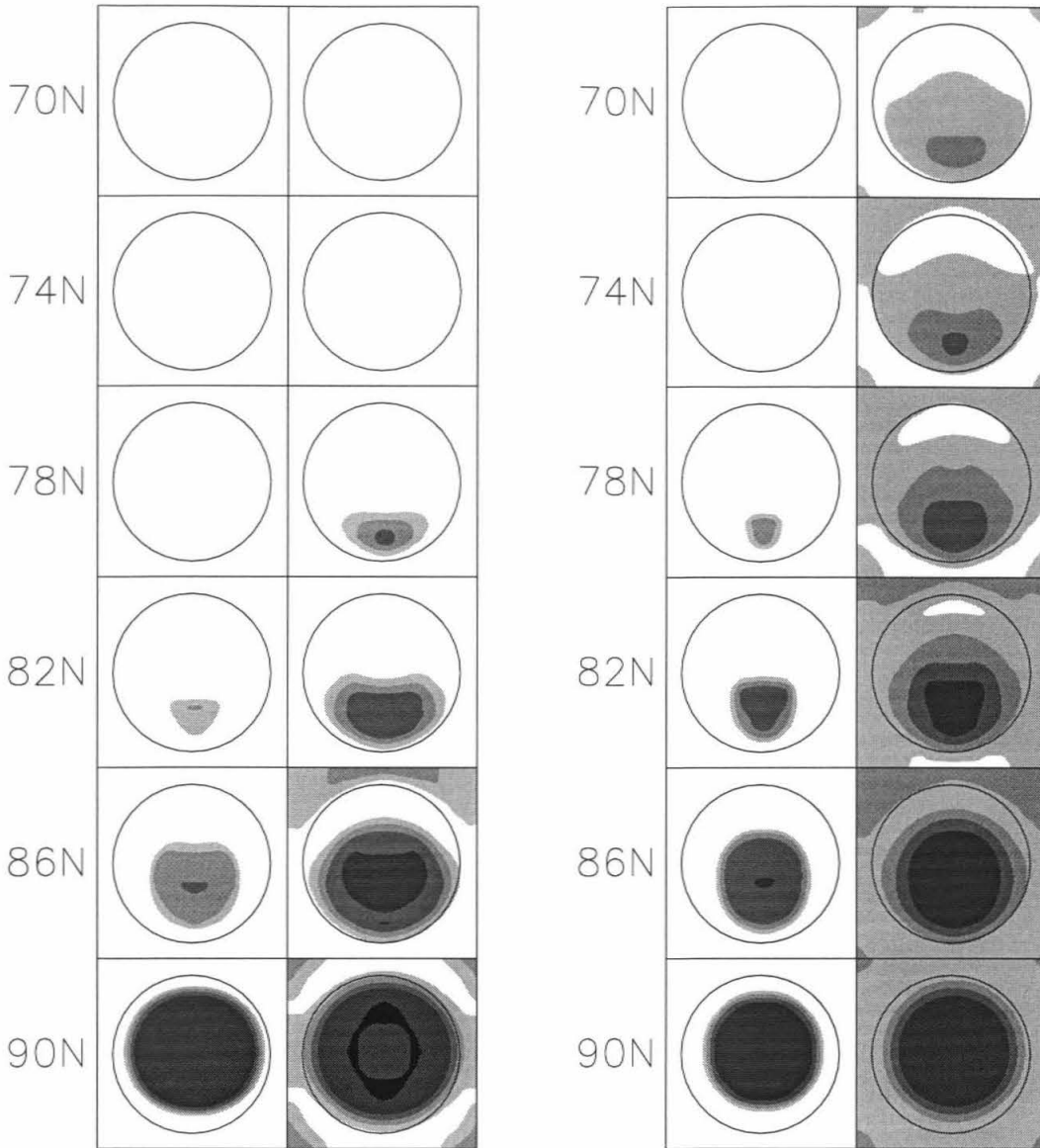
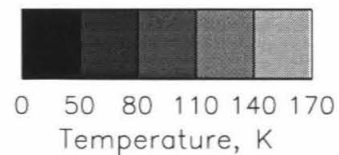


Figure 10. Diurnal maximum and average surface temperatures within 40 km flat-floored craters on Mercury (left set of columns) and the Moon (right set of columns). The left column of each set shows maximum temperatures. The right column of each set shows average temperatures. The crater rim is drawn as a solid line.



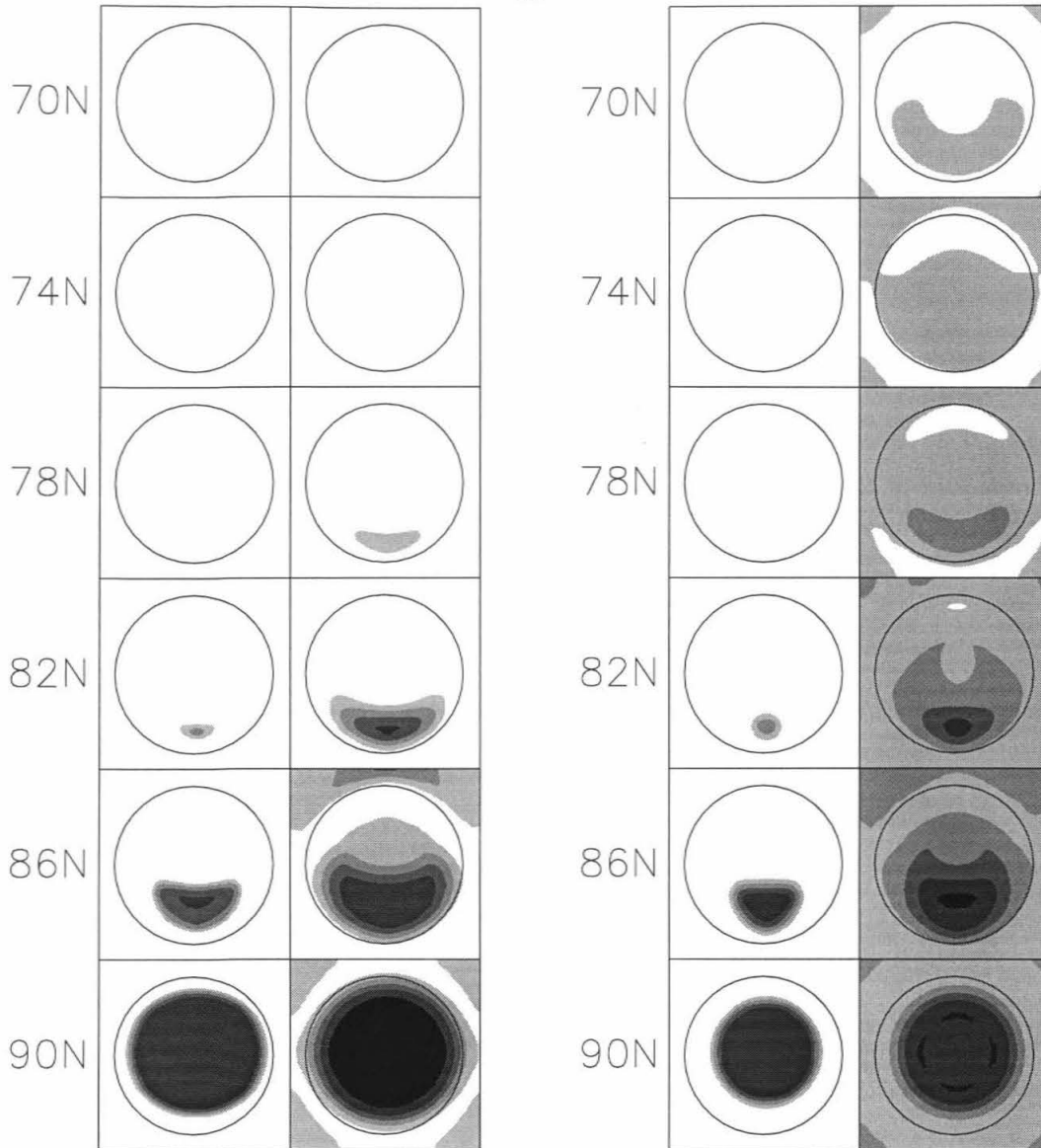


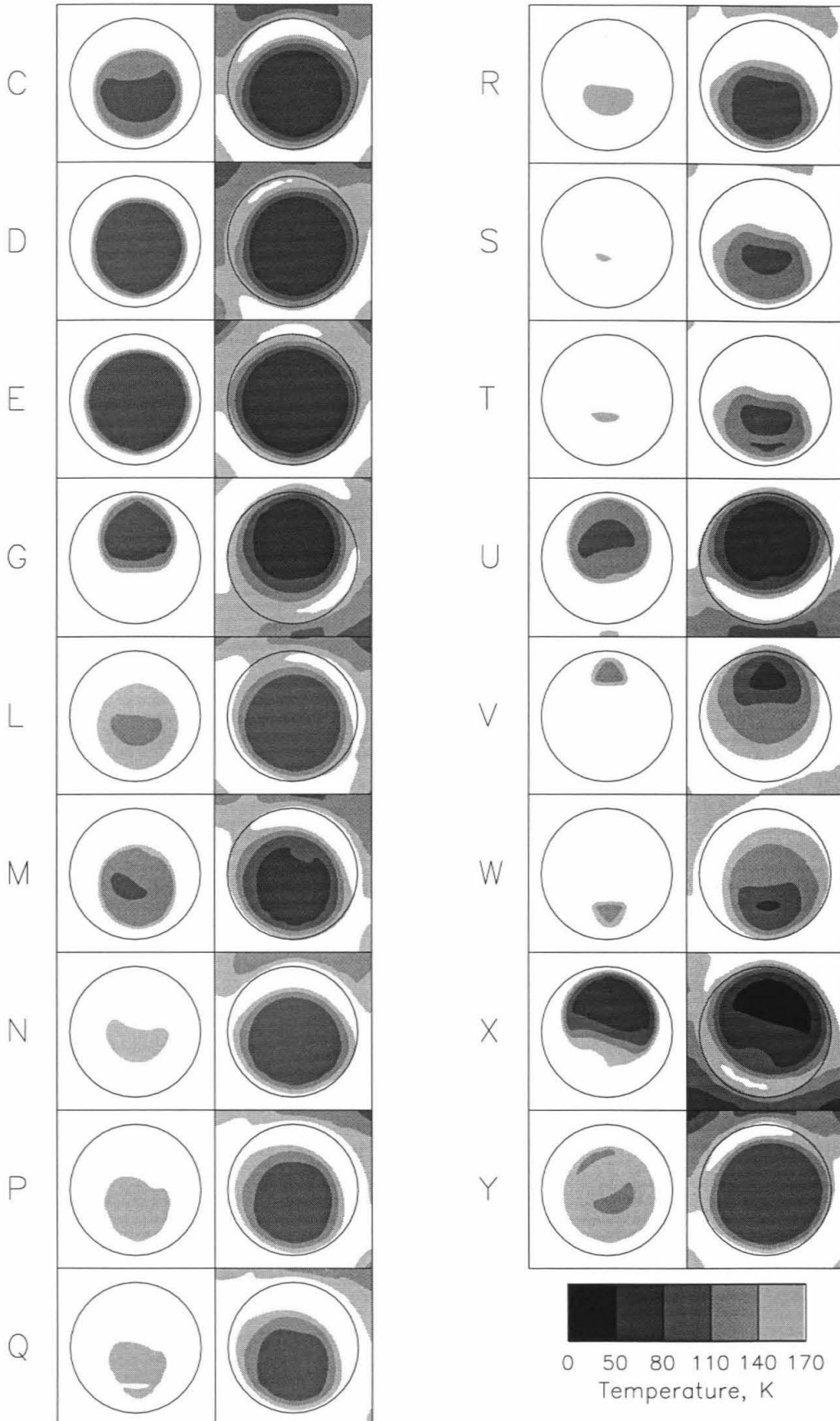
Figure 11. Diurnal maximum and average surface temperatures within 100 km flat-floored craters on Mercury (left set of columns) and the Moon (right set of columns). The left column of each set shows maximum temperatures. The right column of each set shows average temperatures. The crater rim is drawn as a solid line.

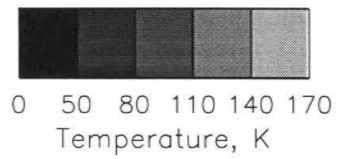
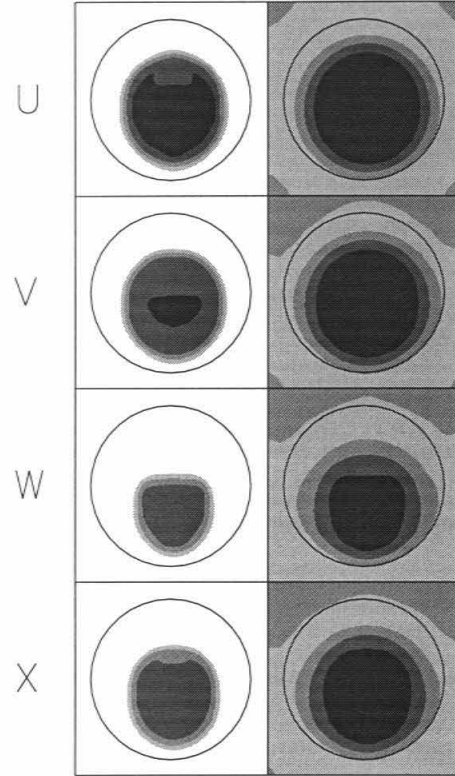
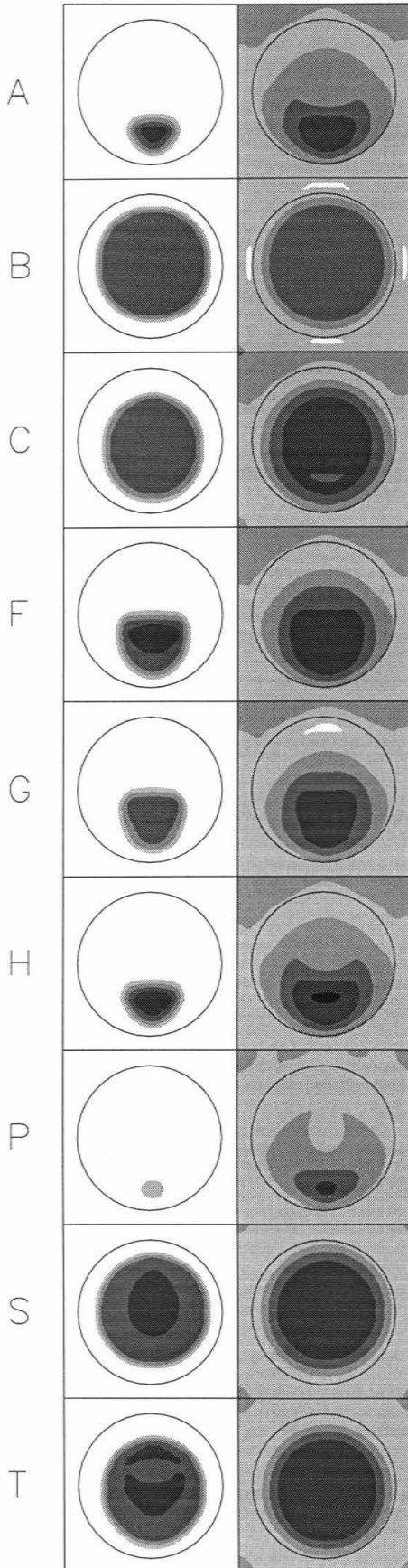


0 50 80 110 140 170
Temperature, K

Figure 12 (next page). Diurnal maximum and average surface temperatures within craters observed near Mercury's poles. The left column of each set shows maximum temperatures. The right column of each set shows average temperatures. The crater rim is drawn as a solid line.

Figure 13 (page after next). Diurnal maximum and average surface temperatures within craters observed near the Moon's poles. The left column of each set shows maximum temperatures. The right column of each set shows average temperatures. The crater rim is drawn as a solid line.





within permanently shaded areas, it is included in these calculations. Consequently, temperature is not constant with depth below the near-surface oscillation, but it increases with depth. At temperatures well below ~ 350 K, the average surface temperature is approximately the temperature just below the attenuation depth of the near-surface oscillation.

The results share some common characteristics. As discussed in previous studies, shallower features contain colder permanently shaded areas. In fact, temperatures depend more strongly on the shape of craters than their latitude. The steeper walls of craters with larger depth-to-diameter ratios receive sunlight at smaller incidence angles and scatter and emit energy more directly towards their interiors. The scattering angle between the poleward sunlit wall and the equatorward shaded floor is larger in flat-floored craters than in bowl-shaped craters with the same depth-to-diameter ratio. However, shallower craters also have less permanently shaded area at a given latitude. The physical size of craters matters only for the largest craters, for which the curvature of the planet decreases the visibility of the sunlit walls from the shaded floors, but increases the amount of sunlit area. The temperature distributions for craters on Mercury may be asymmetric about the north-south axis depending on the time lag between local noon and perihelion.

Figure 14 shows that exposed water ice deposits are not stable within 10-km craters on Mercury. Water ice deposits can survive on the floors of 40-km craters as far as 8° latitude from the poles, beyond which their permanently shaded

area is warmer than 112 K. Water ice is stable in 100-km craters as far as 10° latitude from the poles, beyond which they contain no permanently shaded area. Many, but not all of the craters on Mercury associated with radar features can have stable water ice deposits exposed on their floors. Figure 15 shows that 10-km craters within 2° latitude of Mercury's poles can harbor water ice deposits if the deposits are protected from the extreme surface temperatures. The permanently shaded portions of 40-km craters, 100-km craters, and all observed craters contain regions where average temperatures are below 112 K.

Figure 16 shows that exposed water ice deposits would quickly evaporate within 10-km craters on the Moon. Surface deposits can survive within all 40-km and 100-km craters that contain permanently shaded area, and within all observed craters that were modeled. Thermally protected water ice deposits can survive in 10-km craters within about 10° latitude of the poles, as shown in Fig. 17.

Figure 18 illustrates how the amount of permanently shaded area within craters varies with their diameter and latitude. Very large craters near the Moon's poles have significantly less permanently shaded area than their counterparts on Mercury because of the Moon's greater obliquity. The results shown in Figs. 14-17 predict the sizes of craters and the range of latitudes for which ice deposits are stable. The size of the deposit relative to the size of the crater can then be estimated from Fig. 18.

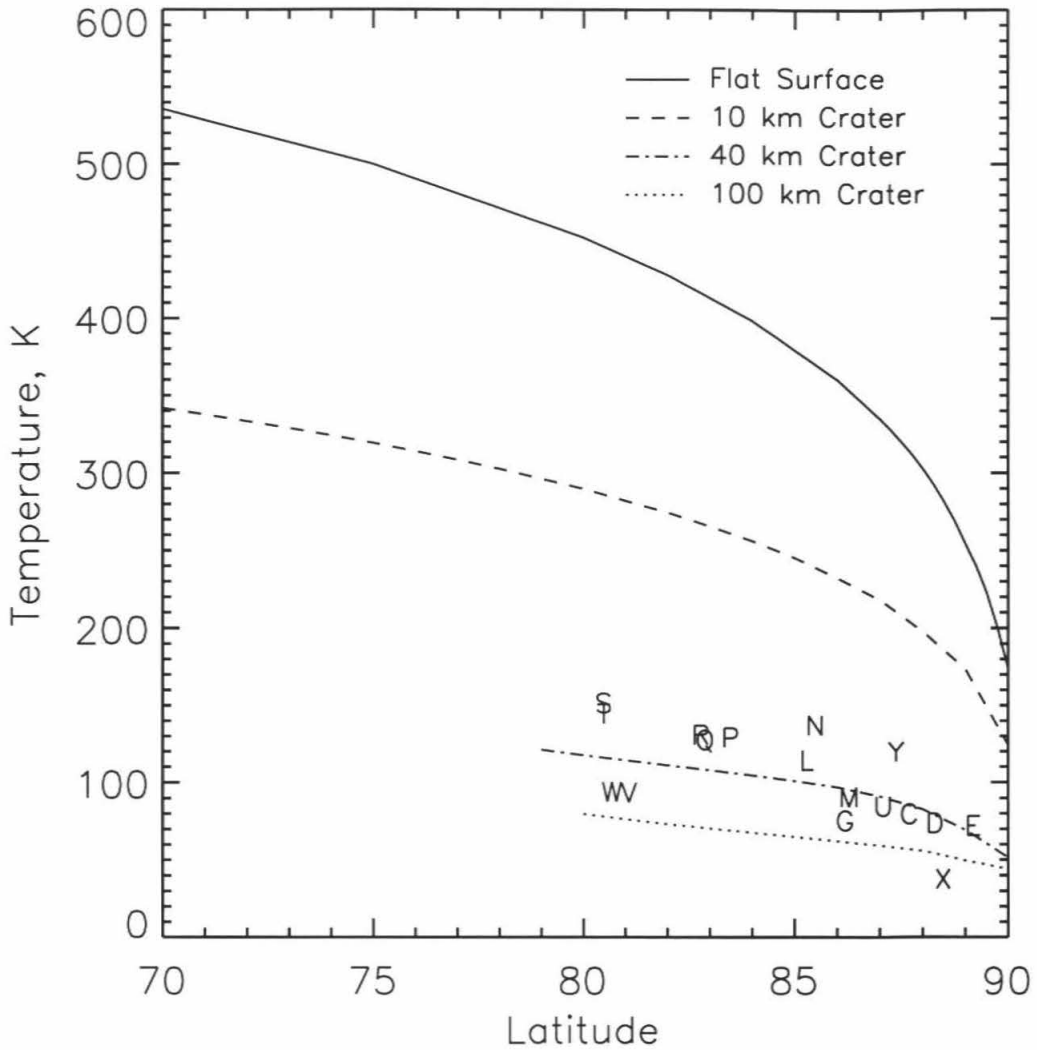


Figure 14. Diurnal maximum surface temperature of the coldest surface element within craters on Mercury. Curves are shown for 10-km bowl-shaped craters (dashed), 40-km flat-floored craters (dash-dot), 100-km flat-floored craters (dotted), and craters observed near Mercury's poles (lettered). The maximum surface temperature of an unshaded surface is shown for comparison.

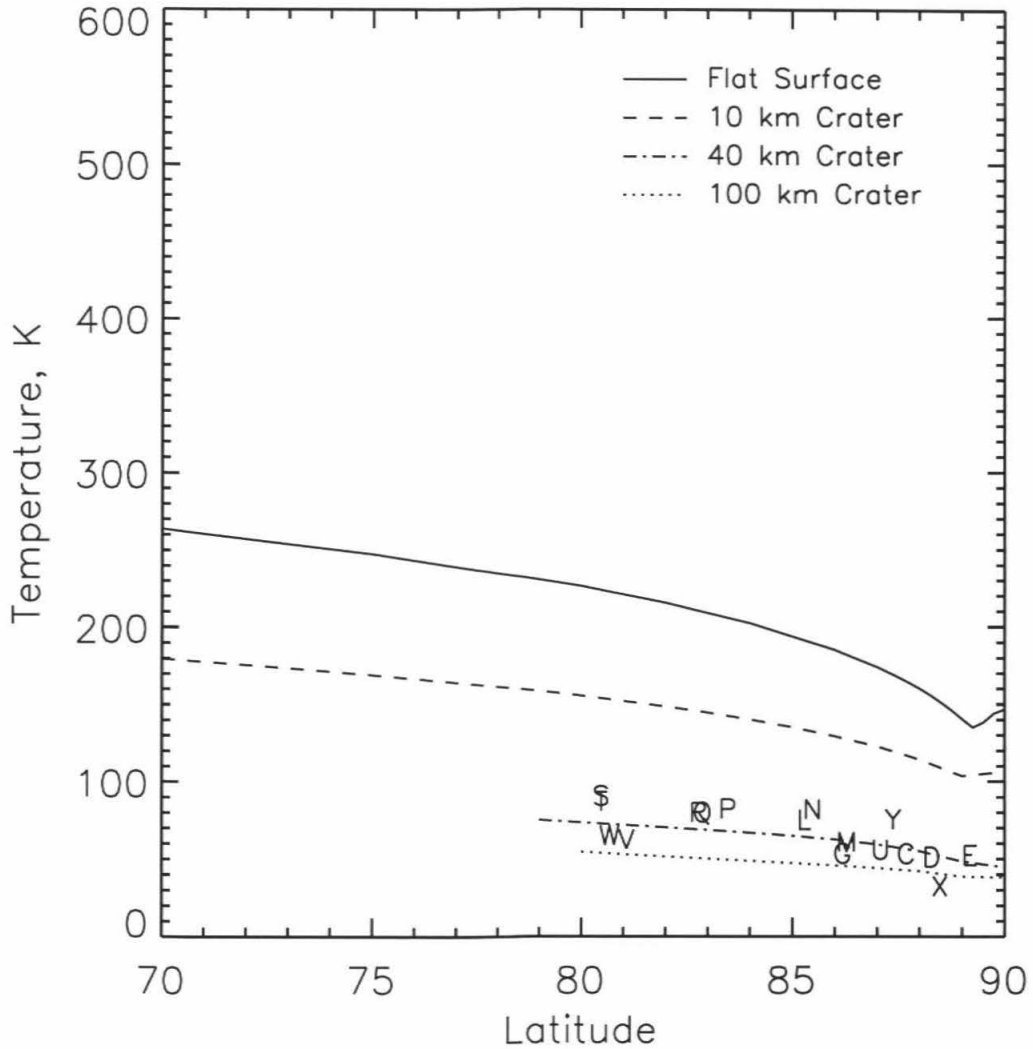


Figure 15. Diurnal average surface temperature of the coldest surface element within craters on Mercury. In shaded regions the average surface temperature is nearly equal to the temperature just below the attenuation depth of the surface temperature oscillation. Curves are shown for 10-km bowl-shaped craters (dashed), 40-km flat-floored craters (dash-dot), 100-km flat-floored craters (dotted), and craters observed near Mercury's poles (lettered). The average surface temperature of an unshaded surface is shown for comparison.

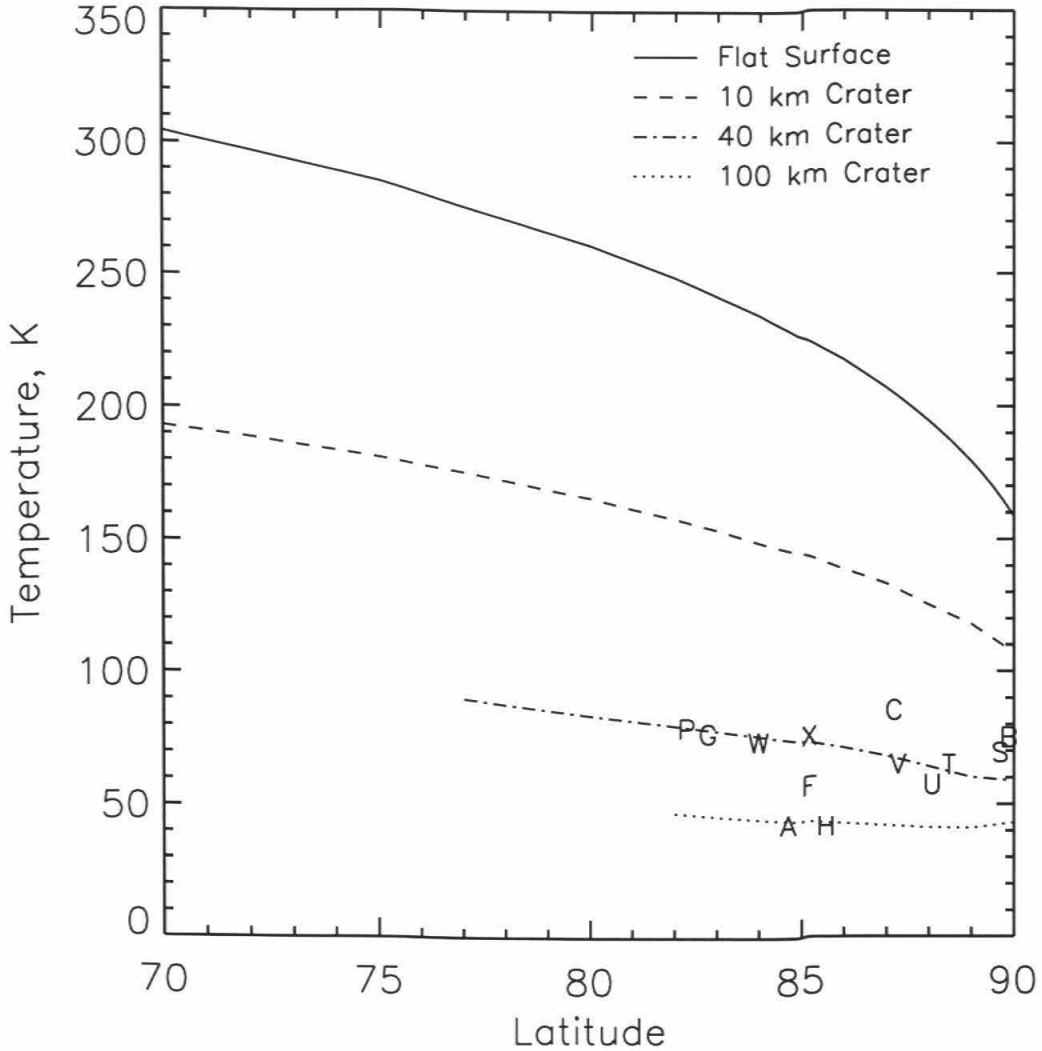


Figure 16. Diurnal maximum surface temperature of the coldest surface element within craters on the Moon. Curves are shown for 10-km bowl-shaped craters (dashed), 40-km flat-floored craters (dash-dot), 100-km flat-floored craters (dotted), and craters observed near the Moon's poles (lettered). The maximum surface temperature of an unshaded surface is shown for comparison.

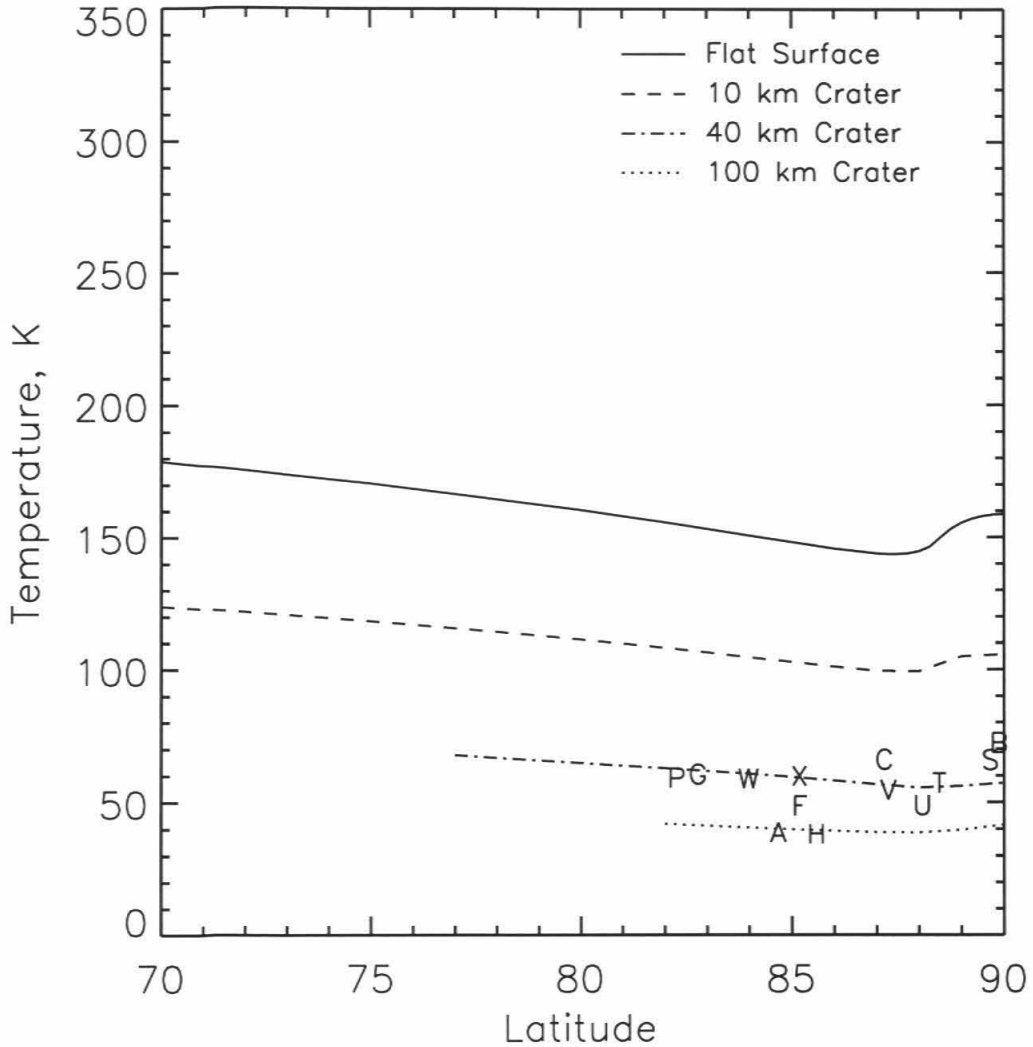


Figure 17. Diurnal average surface temperature of the coldest surface element within craters on the Moon. In shaded regions the average surface temperature is nearly equal to the temperature just below the attenuation depth of the surface temperature oscillation. Curves are shown for 10-km bowl-shaped craters (dashed), 40-km flat-floored craters (dash-dot), 100-km flat-floored craters (dotted), and craters observed near the Moon's poles (lettered). The average surface temperature of an unshaded surface is shown for comparison.

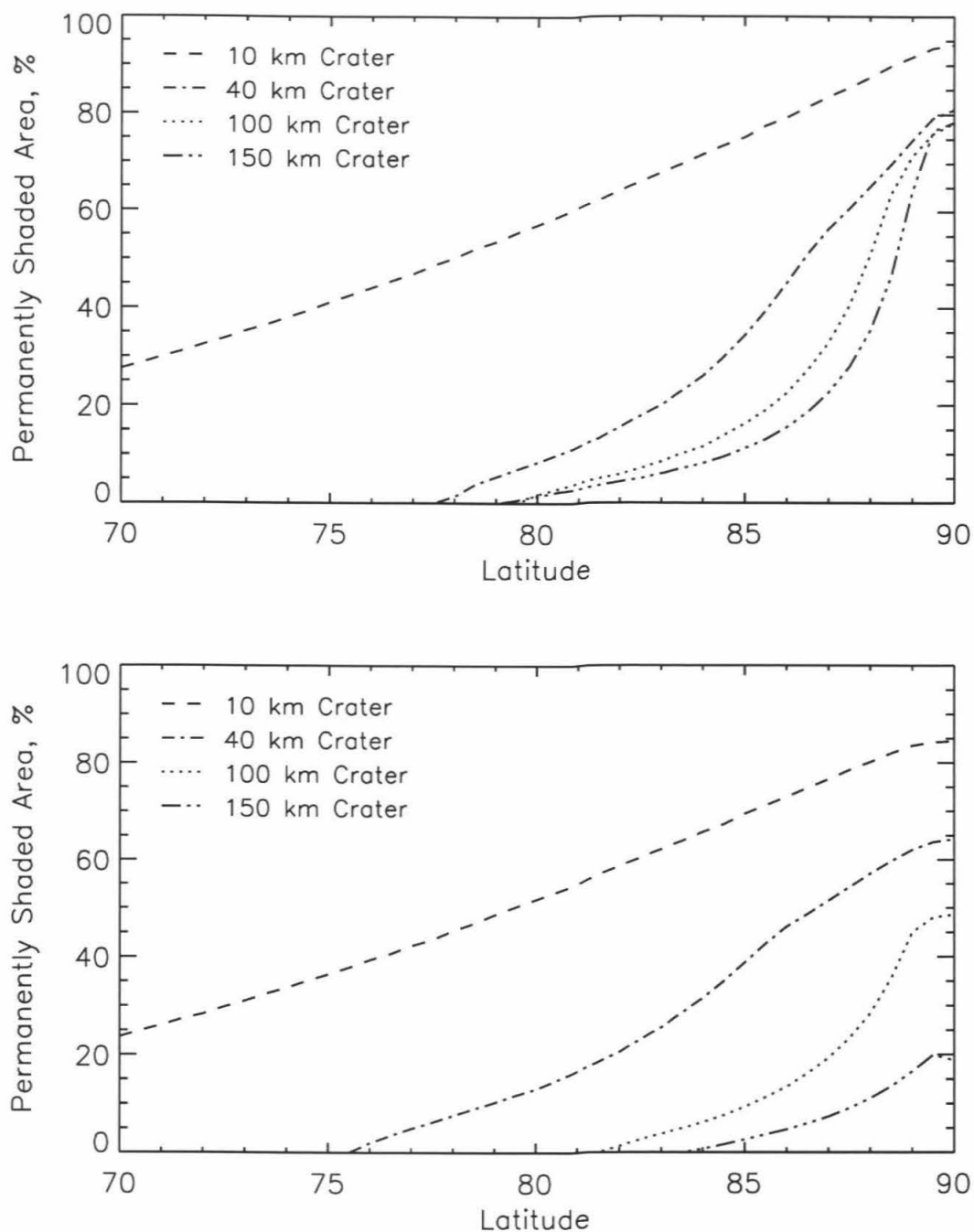


Figure 18. Permanently shaded area as a function of latitude for impact craters on Mercury (top) and the Moon (bottom). At high latitudes, lunar craters have less permanently shaded area than craters of the same size on Mercury because of the Moon's 1.54° solar obliquity.

C. Comparison with Radar Features on Mercury

One of the goals of this study is to better determine the temperatures of surfaces on Mercury that produce ice-like radar responses. Specifically, how do the results of our model compare with the observed sizes and latitudinal distribution of radar features? The radar maps of Harmon *et al.* (1994), shown in Fig. 19, are a compilation of many observations and have a resolution of ~ 15 km. We can make two inferences by comparing our results with specific features. Craters very near the poles of Mercury, such as craters C and D, contain large regions in which surface temperatures never exceed 112 K. The regions where the model predicts stable surface or subsurface ice deposits are consistent with the sizes of the radar features at those locations.

More surprising, radar features are seen within craters where model surface temperatures greatly exceed 112 K, such as craters S and T. The coldest regions within those craters have maximum surface temperatures above 145 K and cover a very small fraction of their crater floors. Most of the floor within each crater is not permanently shaded and experiences much higher temperatures. However, if the stability of these deposits is controlled by the diurnal average surface temperature, our model results are consistent with deposits large enough to produce crater-sized radar features.

The major conclusions of this section are that (i) water ice deposits on unshaded surfaces (polar caps) are not stable to evaporation on either planet over the age of the solar system, (ii) subsurface ice is stable within 2° latitude of the

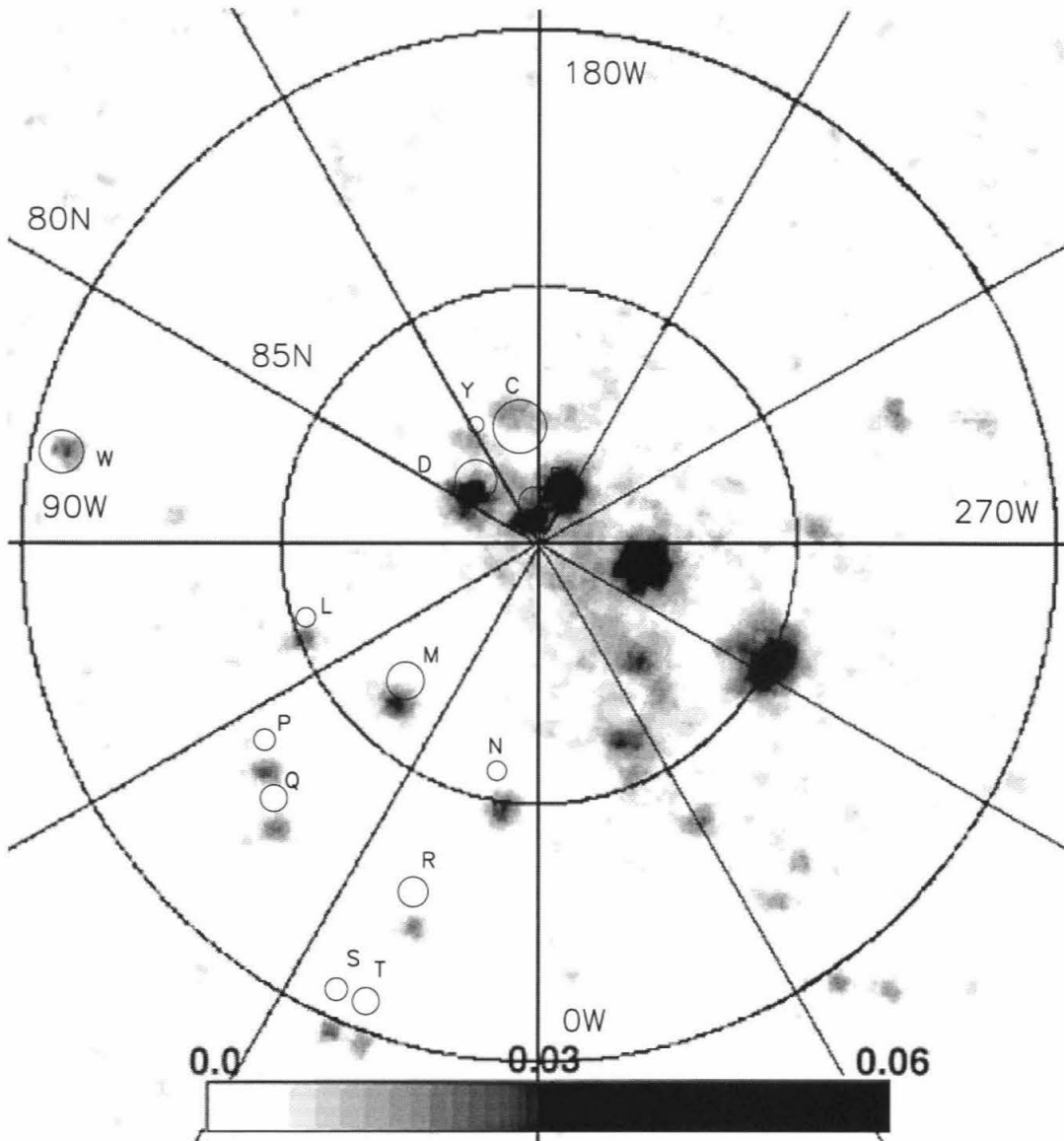


Figure 19a. Arecibo 13.5-cm radar map of Mercury's north pole, after Harmon *et al.* (1994). The gray levels show specific cross section in the depolarized (unexpected) sense of circular polarization. The spatial resolution is ~ 15 km. The locations and sizes of craters observed near Mercury's poles are indicated by the labeled circles. The locations of the circles represent the recent re-analysis of Mariner 10 imagery by Davies *et al.* (1996).

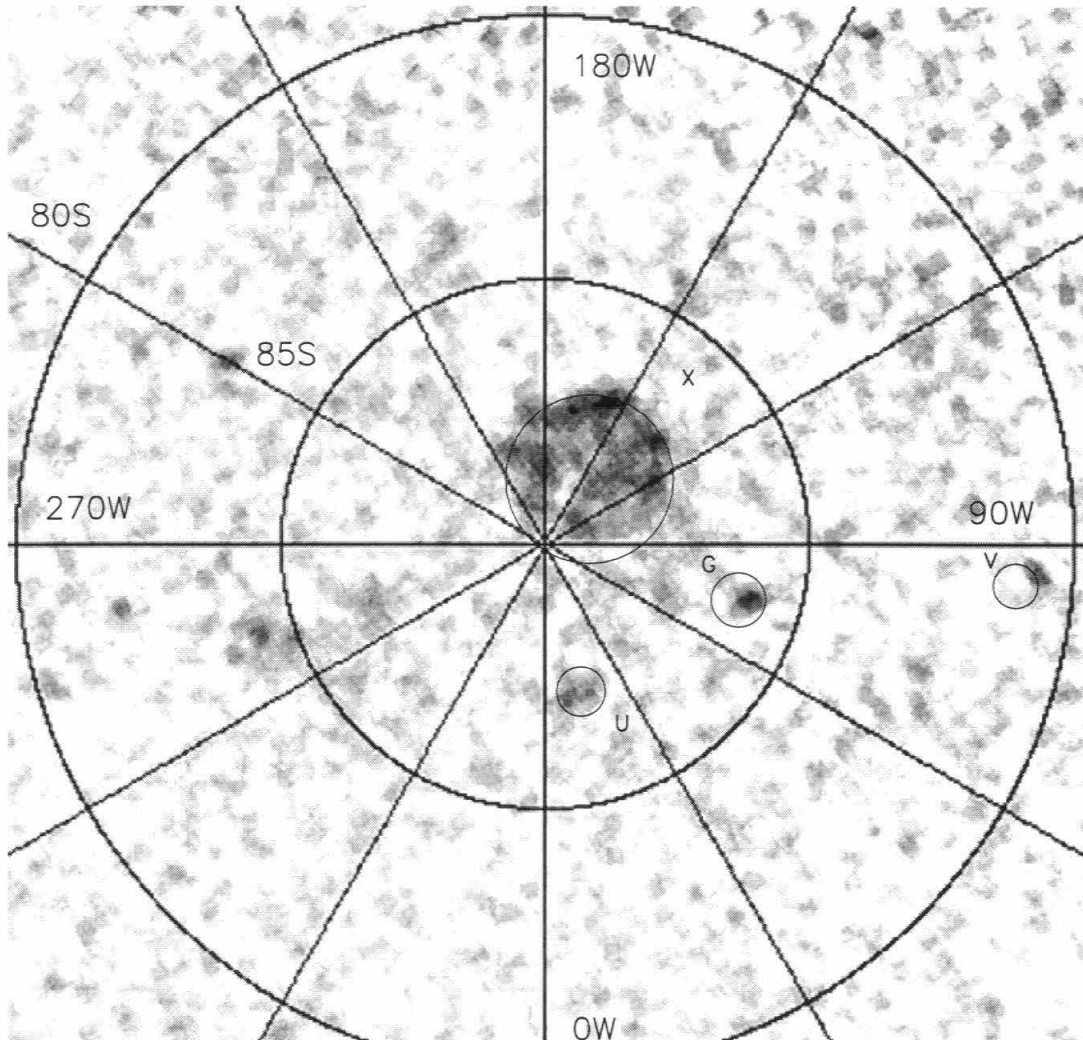


Figure 19b. Arecibo 13.5-cm radar map of Mercury's south pole, after Harmon *et al.* (1994). The gray levels show specific cross section in the depolarized (unexpected) sense of circular polarization. The spatial resolution is ~ 15 km. The south pole data have a lower signal-to-noise ratio. The locations and sizes of craters observed near Mercury's poles are indicated by the labeled circles. The locations of the circles represent the recent re-analysis of Mariner 10 imagery by Davies *et al.* (1996).

lunar pole, (iii) ice deposits within the permanently shaded portions of impact craters are stable as far as 10° and 13° latitude from the poles of Mercury and the Moon, respectively, and (iv) ice deposits are stable within all of the craters observed to produce an ice-like radar response on Mercury, although some deposits must be protected from extreme daytime temperatures. The permanently shaded portions of lunar craters are colder than regions within similar craters on Mercury because of the smaller solar flux at the Moon. The latitudinal extent of permanently shaded regions is similar on Mercury and the Moon because the increased apparent size of the solar disk at Mercury's orbit has a similar effect as the Moon's small obliquity.

IV. SUBSURFACE ICE DEPOSITS

A. Thermal Protection for Low-Latitude Deposits

Model-calculated surface temperatures within craters N, P, Q, R, S, T, and Y on Mercury are significantly above the limit for long-term stability of water ice. Yet these craters contain large radar features on the Arecibo maps. What can account for this discrepancy? Perhaps the craters are uncharacteristically shallow. Their permanently shaded areas would then be colder, but also smaller. This is not a favorable explanation for craters such as S and T which in the present model contain small permanently shaded areas. Another possibility is that our assumed temperature limit should be higher. The limit of 112 K was calculated using vapor pressure data extrapolated by several orders of magnitude beyond lab measurements down to 132 K (Bryson *et al.* 1974). However, the limit would have

to be ~150 K for our model to predict surface ice deposits within all of the observed craters. A limit of ~190 K is more consistent with the sizes of the observed radar features. At 150 K and 190 K, well-determined loss rates are one meter per 10^4 years and one meter per year, respectively, making this explanation implausible. If the deposits are composed of elemental sulfur, the calculated temperature limit is ~218 K. With this limit our model results match the radar features, but as pointed out by Butler (1997), also predict a (sunlit) surface polar cap 1° latitude wide. A polar cap is neither observed in Mariner 10 imagery nor suggested by the Arecibo radar mapping.

These arguments refute the presence of surface ice in the lowest latitude craters that contain radar features. Instead we suggest the following explanation. An ice deposit buried beneath the attenuation depth of sunlight-driven temperature oscillations would remain at a constant temperature nearly equal to the average surface temperature. If we use 112 K as a limit for the *average* surface temperature, our model predicts the sizes and latitudinal distribution of the radar features without also predicting a polar cap on or beneath the surface. A subsurface polar cap would be expected only if the temperature limit were greater than ~130 K. Thermal protection by burial best reconciles model results with observations. Our results are consistent with all deposits on Mercury being buried, or just lower-latitude deposits. We note that a regolith cover also would limit evaporative loss by acting as a barrier to diffusing molecules. This could raise the effective temperature limit by tens of Kelvin, and is discussed in Salvail and Fanale

(1994). A thin regolith cover would also protect the deposits from sputtering by solar wind ions and ablation by interstellar UV.

B. Compatibility with Radar Observations

We have suggested that lower-latitude ice deposits observed on Mercury are thermally protected by a thin regolith layer. In this section we discuss whether this idea is consistent with the radar observations. Although never experimentally demonstrated, it is generally agreed that the unique radar responses from solar system ices arise from volume scattering within a relatively pure, lossless medium (e.g., Butler *et al.* 1993). Rignot (1995) found that parts of the Greenland ice sheet where 'pipes, lenses, and layers' of re-frozen meltwater are embedded in a corn snow matrix produce a similar radar return. Assuming a similar mechanism (with different scatterers) operates on Mercury, volume scattering of centimeter and decimeter wavelength radiation requires that the ice layer be pure and at least several meters thick (Butler *et al.* 1993).

Would this layer of ice be detected by radar if buried beneath a thin regolith cover? Butler *et al.* (1993) suggests that a regolith cover may explain differences in the radar cross section of the deposits between observations of Mercury at different spatial resolutions, and between observations of Mercury and Mars. Butler *et al.* (1993) found relatively low radar reflectivities compared to those observed on Mars' south polar residual ice cap. The difference could arise if the ice deposits were unresolved or if some energy was absorbed by a regolith cover. If due only to the latter, Butler *et al.* (1993) estimate that a regolith cover with a

density of $\sim 1000 \text{ kg m}^{-3}$ would be 0.5 m thick. The higher-resolution Arecibo maps revealed that the actual ice coverage within the features described by Bulter *et al.* (1993) may have been as little as 10%. The tradeoff between coverage and absorption, quantified in Fig. 10 of Butler *et al.* (1993), indicates that the regolith layer is probably less than 0.5 m thick. A regolith cover between 0.1 and 0.5 m thick would be sufficient to dampen surface temperature variations without absorbing a significant percentage of the radio signal.

C. Deposition and Burial

Explanations of how subsurface ice is deposited and buried are speculative. How might a relatively pure layer of water ice be emplaced? Water ice is delivered to the surfaces of Mercury and the Moon by comets, asteroids, meteorites, interplanetary dust, solar wind reduction of crustal Fe^0 , and outgassing. Deposits like those thought to be present on Mercury must be emplaced faster than the rates of contamination and loss. An episodic source, such as comets, seems more likely to produce pure ice deposits than a continuous source. Gradually-emplaced deposits would be mixed with micrometeoritic material and dust. Morgan and Shemansky (1991) argue that impact vaporization and interstellar H Ly α would destroy deposits from continuous sources as quickly as they accumulate. Several lines of reasoning favor comets, or even one large comet, as most likely to produce ice deposits on Mercury or the Moon. More work needs to be done to understand the retention of volatiles after a comet impact, the possible formation of a temporary atmosphere (and a protective ionosphere), and the migration of water to

the poles in a collisional atmosphere. Killen *et al.* (1997) argue that extinct comet nuclei are the most likely of all sources to deliver large amounts of water to Mercury's poles.

How are the deposits buried, and what controls the depth of burial? Gardening by micrometeorites, which disturbs the regolith and erodes crater walls, is an important and ubiquitous process on the surfaces of both planets. Ice deposits might be covered by ejecta or by mass wasting. Killen *et al.* (1997) estimate that local meteoritic impacts and lateral transport of impact debris will form a 1-cm layer in 50 million years. The resulting cover probably would spatially vary in thickness.

Another possibility is that sublimation results in a self-sealing residue. A slightly dirty ice deposit might sublimate until its contaminant load forms a layer that thermally or diffusively limits sublimation of the underlying ice. The final thickness of the layer would be the attenuation depth of the temperature oscillation if the layer is primarily an insulating layer. Because the diffusion rate is proportional to the regolith temperature, the final thickness of a diffusion-limited residue also may be the attenuation depth of temperature oscillations (see Figs. 4 and 10 of Salvail and Fanale 1994). This process requires that a large initial volume of ice is lost to sublimation in order to build the residue.

V. ICE DEPOSITS ON MERCURY AND THE MOON

The radar observations of Mercury, when compared to the results of our model, argue that volume of volatiles preserved at its poles is limited by the

availability of storage sites. In other words, Mercury's cold traps are full. Nearly every crater that is observed on images to have an undegraded rim and was shown to have regions where temperatures permit the stability of water ice is also associated with a radar feature. The condensation and survival of ice in warmer, lower-latitude craters further argues for a large supply of water. The fullness of Mercury's cold traps could also be explained by a very recent comet impact or other unexpectedly high supply rates.

Very recent data from the neutron spectrometer aboard the Lunar Prospector mission are consistent with a 1% mixing ratio of water in the polar regions (William Feldman, personal communication). The instrument senses the top 0.5 m of the lunar surface. Although none of the lunar radar or spacecraft experiments have decisively ruled out the presence of large quantities of ice, it is useful to consider factors that could result in differences between the amounts of ice detected at the poles of the Mercury and the Moon.

From a thermal standpoint, the possibility of lunar ice deposits is favorable. Our model results for craters observed near the Moon's poles, shown in Figs. 13, 16, and 17, suggest that lunar cold traps are larger and colder than those within craters on Mercury thought to contain ice. A small increase in the obliquity of either planet would greatly reduce the amount of permanently shaded area and lead to the loss of any deposits. The Moon may have had a significantly larger obliquity in its early history (Ward 1975). Whether ancient obliquity variations affect present ice concentrations depends on the time history of the sources of volatiles.

Because of the similarity between the two planets and their proximity in the solar system, source mechanisms themselves do not differ greatly between them. The mass flux due to comet, asteroid, and meteorite impacts is roughly the same on both planets. These bodies will have larger impact velocities at Mercury that may result in less retention of volatiles. If impacts of large comets are the primary sources of water ice and occur on billion-year timescales (Arnold 1979), the abundance of ice at a given epoch could vary greatly between the planets.

The lack of polar topography may limit the total volume of deposits, but not their detectability. The radar features on Mercury are confined to permanently shaded areas within polar impact craters. There may be fewer impact craters or other terrain to form permanently shaded area near the Moon's poles. Cold traps would still be detected as long as they are large enough to capture migrating water molecules (Butler 1997) and are resolved by the detection technique.

Loss from sputtering by energetic particles may be more significant on the Moon. The Moon is not shielded by a magnetic field from the solar wind. It also passes repeatedly through the Earth's geotail where the directions of particles are more isotropic (Lanzerotti *et al.* 1981).

It may be possible that meter-thick deposits are present on both planets but not detectable on the Moon by the same techniques used for Mercury. Mercury-like deposits, if mixed with regolith, would not be detected by radar. Buried, pure deposits may be masked on the Moon if the regolith is more opaque at radar wavelengths (Jeanloz *et al.* 1995).

VI. CONCLUSIONS

The primary results of this work are that (i) our model-calculated zones of water ice stability on Mercury support the interpretations of radar experiments, and (ii) similarly cold sites exist near the Moon's poles. We constructed a thermal model that calculates temperatures within bowl-shaped and flat-floored polar impact craters. We applied this model to craters on Mercury and the Moon, incorporating the latest estimates of their locations. We find that while sunlit polar caps are not stable on the surfaces of either planet, large water ice deposits are stable within flat-floored craters up to 10° latitude from the poles of Mercury and 13° latitude from the poles of the Moon. Water ice deposits are stable in all craters on Mercury associated with radar features, although lower-latitude deposits must be protected from extreme daytime temperatures. We suggest that a thin regolith layer covers these deposits, protecting them from extreme temperatures. A regolith cover could also limit losses by sputtering, ablation from interstellar UV, and sublimation, and is implied independently by the radar observations.

Several groups propose to use ground based radar and spacecraft UV spectroscopy, neutron spectrometers, and radar to study potential ice deposits on Mercury and the Moon. Polar orbiting radar systems have the distinct advantage of being able to probe at depth and create maps from an ideal viewing geometry. Radar mapping with supporting image and topographic data will yield the best dataset to compare with theory and models. The results of neutron spectrometers, which do not resolve individual deposits, are less informative but are necessary to

determine composition. UV spectroscopy and other methods that search for trace exospheric signatures of condensed volatiles may be ambiguous if the deposits are not in diffusive contact with the exosphere. In the long term, *in situ* devices that can withstand the extremely cold temperatures near these deposits will best determine their nature and composition.

Acknowledgments. The idea for this project originated in discussions with David Paige and Stephen Wood. We thank J. K. Harmon, Tim Colvin, Jean-Luc Margot, Nick Stacy, Don Campbell, and their respective colleagues for sharing their results. We benefited from the comments of Dewey Muhleman, Martin Slade, and two anonymous reviewers. We thank A. P. Ingersoll for interest and support of this project.

References

- Allen, C. W. 1973. *Astrophysical Quantities*, The Althone Press, London.
- Arnold, J. R. 1979. Ice in the lunar polar regions. *J. Geophys. Res.* **84**, 5659-5668.
- Arnold, J. R. 1979. Ice in the lunar polar regions. *J. Geophys. Res.* **84**, 5659-5668.
- Bryson III, C. E., V. Cazcarra, and L. L. Levenson 1974. Sublimation rates and vapor pressures of H₂O, CO₂, N₂O, and Xe. *J. Chem. Eng. Data* **19**, 107-110.
- Butler, B. J. 1997. The migration of volatiles on the surfaces of Mercury and the Moon. *J. Geophys. Res.* **102**, 19283-19291.
- Butler, B. J., D. O. Muhleman, and M. A. Slade 1993. Mercury: Full disk radar images and the detection and stability of ice at the north pole. *J. Geophys. Res.* **98**, 15003-15023.
- Cremers, C. J., and R. C. Birkebak 1971. Thermal conductivity of fines from Apollo 12. *Proc. 2nd Lun. Sci. Conf.* **3**, 2311-2315.
- Cuzzi, J. N. 1974. The nature of the subsurface of Mercury from microwave observations at several wavelengths. *Astrophys. J.* **189**, 577-586.
- Davies, M. E., D. E. Gault, S. E. Dwornik, and R. G. Strom (eds.) 1978. *Atlas of Mercury*, NASA Scientific and Technical Information Office, Washington D.C.

- Davies, M. E., T. R. Colvin, M. S. Robinson, and K. Edwards 1996. Mercury's polar regions: Locations of radar anomalies (ice). *Bull.--Am. Astron. Soc.* **28**, 1115.
- Goldstein, R. M., and G. A. Morris 1975. Ganymede: Observations by radar. *Science* **188**, 1211-1212.
- Goral, C. M., K. E. Torrance, D. P. Greenberg, and B. Battaile 1984. Modeling the interaction of light between diffuse surfaces. *Computer Graphics* **18**, 213-222.
- Hagfors, T., I. Dahlstrøm, T. Gold, S.-E. Hamran, and R. Hansen 1997. Refraction scattering in the anomalous reflections from icy surfaces. *Icarus* **130**, 313-322.
- Haldemann, A. F. C. 1997. *Interpreting radar scattering: Circular-polarization perspectives from three terrestrial planets*. Ph.D. Dissertation, California Institute of Technology.
- Hapke, B. 1990. Coherent backscatter and the radar characteristics of outer planet satellites. *Icarus* **88**, 407-417.
- Harmon, J. K., M. A. Slade, R. A. Velez, A. Crespo, M. J. Dreyer, and J. M. Johnson 1994. Radar mapping of Mercury's polar anomalies. *Nature* **369**, 213-215.
- Harmon, J. K., and M. A. Slade 1992. Radar mapping of Mercury: Full-disk images and polar anomalies. *Science* **258**, 640-643.

- Heiken, G., D. Vaniman, and B. M. French 1991. *Lunar Sourcebook*, Cambridge University Press, New York.
- Hodges, R. R. 1980. Lunar cold traps and their influence on argon-40. *Proc. Lunar Planet. Sci. Conf.* **11th**, 2463-2477.
- Ingersoll, A. P., T. Svitek, and B. C. Murray 1992. Stability of polar frosts in spherical bowl-shaped craters on the Moon, Mercury, and Mars. *Icarus* **100**, 40-47.
- Jeanloz, R., D. L. Mitchell, A. L. Sprague, and I. de Pater 1995. Evidence for a basalt-free surface on Mercury and implications for internal heat. *Science* **268**, 1455-1456.
- Jenniskens, P., and D. F. Blake 1996. Crystallization of amorphous water ice in the solar system. *Astrophys. J.* **473**, 1104-1113.
- Keihm, S. J., and M. G. Langseth, Jr. 1973. Surface brightness temperatures at the Apollo 17 heat flow site: Thermal conductivity of the upper 15 cm of regolith. *Proc. Lunar Sci. Conf. 4th, Geochim. Cosmochim. Acta Suppl.* **4**, 2503-2513.
- Killen, R. M., J. Benkhoff, and T. H. Morgan 1997. Mercury's polar caps and the generation of an OH exosphere. *Icarus* **125**, 195-211.
- Langseth, M. G., S. J. Keihm, and K. Peters 1976. Revised lunar heat-flow values. *Proc. Lunar Sci. Conf.* **7**, 3143-3171.

- Langseth, M. G., S. P. Clark, J. Chute, and S. Keihm 1972. The Apollo 15 Lunar heat flow measurement. In *Thermal Characteristics of the Moon* (J. W. Lucas, Ed.), pp. 205-232. MIT Press, Cambridge.
- Lanzerotti, L. J., W. L. Brown, and R. E. Johnson 1981. Ice in the polar regions of the Moon. *J. Geophys. Res.* **86**, 3949-3950.
- Lide, D. R. (Ed.) 1993. *CRC Handbook of Chemistry and Physics, 74th ed.* CRC Press, Boca Raton.
- Linsky, J. L. 1966. Models of the lunar surface including temperature-dependent thermal properties. *Icarus* **5**, 606-634.
- Ledlow, M. J., J. O. Burns, G. R. Gisler, J. Zhao, M. Zeilik, and D. N. Baker 1992. Subsurface emissions from Mercury: VLA radio observations at 2 and 6 centimeters. *Astrophys. J.* **348**, 640-655.
- Margot, J. L., D. B. Campbell, R. F. Jurgens, M. A. Slade, and N. J. Stacy 1997. High resolution topographic maps of the lunar south pole. *Bull.--Am. Astron. Soc.* **29**, 986.
- Mitchell, D. L., and I. de Pater 1994. Microwave imaging of Mercury's thermal emission at wavelengths from 0.3 to 20.5 cm. *Icarus* **110**, 2-32.
- Morgan, T. H., and D. E. Shemansky 1991. Limits to the lunar atmosphere. *J. Geophys. Res.* **96**, 1351-1367.
- Morrison, D. 1970. Thermophysics of the planet Mercury. *Space Sci. Rev.* **11**, 271-301.

- Moses, J. I., and D. B. Nash 1991. Phase transformations and the spectral reflectance of solid sulfur: Can metastable sulfur allotropes exist on Io? *Icarus* **89**, 277-304.
- Muhleman, D. O., B. J. Butler, A. W. Grossman, and M. A. Slade 1991. Radar images of Mars. *Science* **253**, 1508-1513.
- Nozette, S., C. L. Lichtenberg, P. Spudis, R. Bonner, W. Ort, E. Malaret, M. Robinson, and E. M. Shoemaker 1996. The Clementine bistatic radar experiment. *Science* **174**, 1495-1498.
- Paige, D. A., S. E. Wood, and A. R. Vasavada 1992. The thermal stability of water ice at the poles of Mercury. *Science* **258**, 643-646.
- Pike, R. J. 1988. Impact craters on Mercury. In *Mercury* (F. Vilas, C. R. Chapman, and M. S. Matthews, Eds.), pp. 165-273. University of Arizona Press, Tucson.
- Potter, A. E. 1995. Chemical sputtering could produce sodium vapor and ice on Mercury. *Geophys. Res. Lett.* **22**, 3289-3292.
- Rawlins, K., J. I. Moses, and K. J. Zahnle 1995. Exogenic sources of water for Mercury's polar ice. *Bull.--Am. Astron. Soc.* **27**, 1117.
- Rignot, E. 1995. Backscatter model for the unusual radar properties of the Greenland Ice Sheet. *J. Geophys. Res.* **100**, 9389-9400.
- Salvail, J. R., and F. P. Fanale 1994. Near-surface ice on Mercury and the Moon: A topographic thermal model. *Icarus* **111**, 441-455.

- Schubert, G., M. N. Ross, D. J. Stevenson, and T. Spohn 1988. Mercury's thermal history and the generation of its magnetic field. In *Mercury* (F. Vilas, C. R. Chapman, and M. S. Matthews, Eds.), pp. 429-460. Univ. of Arizona Press, Tucson.
- Siegel, R., and J. R. Howell 1981. *Thermal Radiation Heat Transfer*, Hemisphere Publishing Corporation, Washington.
- Slade, M. A., B. J. Butler, and D. O. Muhleman 1992. Mercury radar imaging: evidence for polar ice. *Science* **258**, 635-640.
- Sprague, A. L., D. M. Hunten, and K. Lodders 1995. Sulfur at Mercury, elemental at the poles and sulfides in the regolith. *Icarus* **118**, 211-215.
- Stacy, N. J. S., D. B. Campbell, and P. G. Ford 1997. Arecibo radar mapping of the lunar poles: A search for ice deposits. *Science* **276**, 1527-1530.
- Thomas, G. E. 1974. Mercury: Does its atmosphere contain water? *Science* **183**, 1197-1198.
- Ward, W. 1975. Past orientation of the lunar spin axis. *Science* **189**, 377-379.
- Watson, K., B. C. Murray, and H. Brown 1961. The behavior of volatiles on the lunar surface. *J. Geophys. Res.* **66**, 3033-3045.

**3. JOVIAN ATMOSPHERIC DYNAMICS
FROM GALILEO IMAGING**

Published as:

Belton M. J. S., and 33 colleagues 1996. Galileo's first images
of Jupiter and the Galilean Satellites. *Science* **274**, 377-384.

and

Vasavada, A. R., and 13 colleagues 1998. Jovian atmospheric dynamics
from Galileo imaging: The Great Red Spot, equatorial region, and
White Ovals. *Icarus*, in press.

I. INTRODUCTION

During its first six orbits of Jupiter, the Galileo spacecraft imaged several atmospheric features on Jupiter including the Great Red Spot, the southern boundary of the Equatorial Zone, a “5- μm hotspot” similar to the Galileo Probe entry site, and two of the classic White Ovals. In this paper, we present imaging data of these features and discuss their appearance and dynamics derived from cloud motions. Galileo extends our view of Jupiter’s atmosphere past Voyager, providing new observations of the poorly-understood system of jets, vortices, and turbulence in giant planet atmospheres. Galileo’s Solid State Imaging (SSI) system produces images similar in spatial resolution to the best Voyager observations, but with greater temporal resolution and in both visible and near infrared wavelengths. The shorter time between observations reduces the error in wind measurements caused by changes in cloud morphology. In active regions, cloud morphology varies over the one-hour interval between Galileo observations (Belton *et al.* 1996). A companion paper (Banfield *et al.* 1998) discusses the vertical cloud structure derived from the imaging dataset. Galileo observed other features during the remaining orbits of its primary mission, and imaged jovian lightning and aurora. These observations will be addressed in future papers.

In the following sections, we describe the observations, image processing, and wind measurement techniques. We then discuss our findings in the context of previous observations. Unless otherwise stated, we use planetocentric latitudes, System III west longitudes, and positive velocities in the northward and eastward

directions. Horizontal, rotational motion of atmospheric features is called cyclonic (anticyclonic) when the projection of the rotation axis onto the north rotational pole has the same (opposite) sign as the planetary rotation axis, e.g., counter-clockwise in the northern hemisphere. The positions and velocities of Jupiter's zonal jets are taken from the Voyager 2 analysis by Limaye (1986).

II. METHODS OF OBSERVATION AND ANALYSIS

A. Imaging Strategy for Jupiter's Atmosphere

The strategy for observing Jupiter with the SSI aboard the Galileo orbiter was to acquire spatial, spectral, and temporal coverage of interesting atmospheric features, each covering a small area on Jupiter's disk (Belton *et al.* 1992, 1996). A time series of multispectral image mosaics, called a feature track, is collected near perijove for one target during each orbit. Mosaics are acquired at four times as the feature rotates with Jupiter below the spacecraft. The feature is observed once (defined as time=0 h) when it is near the center of the illuminated crescent (not the central meridian because the phase angle is near 50°). It is then observed three more times as it moves from near the terminator (time~9 h), to the center (time~10 h), and to the limb (time~11 h) on the subsequent (or previous) rotation of Jupiter. The horizontal resolution is about 30 km pix^{-1} (42 pix deg^{-1}) at the equator, comparable to one vertical atmospheric scale height. Mosaics are obtained in four spectral bands of reflected sunlight by using narrow filters centered at 410 nm (violet), 756 nm (near-infrared continuum), 727 nm (methane absorption band),

and 889 nm (strong methane absorption band). Specifics of the feature track observations are listed in Table I.

The resulting set of mosaics is useful for the study of cloud motions, vertical structure, and center-to-limb variations while meeting the limitations imposed by the spacecraft's impaired tape storage and downlink capabilities. The images that compose the mosaics are reduced to 400×400 pixels (by summing 2×2 boxes) before onboard tape storage and are compressed using a lossy (~12:1) algorithm before transmission to Earth. Throughout the paper, when we use 'pixel', we are referring to summed pixels. The first images of Jupiter, the Great Red Spot mosaics, were transmitted with a compression ratio of ~18:1 and contain artifacts that appear as 8×8-pixel boxes. Later images have few noticeable artifacts. Multiple passes are made through Galileo's tape recorder during playback so that transmission errors can be corrected and especially interesting parts of the summed images can be re-transmitted with lossless compression.

B. Photometric Calibration, Navigation, and Mapping

Photometric calibration, image navigation, and mapping are performed using the VICAR software package developed at the Multi-mission Image Processing Lab of the Jet Propulsion Laboratory. The goal is to create calibrated map projections of the feature track mosaics, removing the effects of the camera, observation, and illumination geometries so that cloud positions can be easily measured. VICAR routines convert raw pixel values to normalized reflectivities, averaging over known camera blemishes and single-pixel cosmic ray hits (Klaasen

Table I. Galileo Feature Track Mosaics

Target	Mosaic Center	Resolution ^a	Spacecraft Event Time
Feature	(lat,lon)	(km pix ⁻¹)	
GRS	(-20,316)	30-36	349605600-349674322
Belt/Zone	(-5,279)	24-30	368388600-368456368
Hotspot	(5,336)	23-29	374456522-374521468
White Ovals	(-31,107)	22-28	383548622-383619422

^a Resolution in km per pixel in the image plane at the 1 bar level.

et al. 1997). The trend in reflectivity across an image due to the solar incidence angle, i , and emergent angle, e , is removed to first order using a Minnaert correction (Minnaert 1941) with a different constant, k , for each wavelength. The correction factor is defined as,

$$f = F/F_0 = (\cos i)^k (\cos e)^{k-1}$$

where F is the corrected reflectivity and F_0 is the normalized reflectivity at $i=0$, $e=0$. This correction is applied in order to maximize the contrast due to cloud opacity variations and does not affect our wind measurements.

Image navigation determines the true pointing of the SSI telescope. Deviations of the camera's optical axis from its commanded position resulted in images that are offset from their predicted locations. We have found both systematic and random offsets. Without fixed geometric markers on Jupiter (e.g., impact craters), one must use the overlap of images within a mosaic, Jupiter's limb, and independent measurements of cloud motions to estimate the true pointing. Aligning the overlap regions within a mosaic provides a relative navigation of high accuracy (~ 1 pixel) and removes the random component of the uncertainty. The VICAR module NAV fits Jupiter's limb to determine absolute navigation, but the limb is present only on one timestep of each feature track. We assume that the limb becomes optically thick at 100 mb in 756-nm images, and use the planetary radius-pressure relation from Lindal *et al.* (1981). The limb-derived correction is about 20 pixels in each of the feature tracks, or about 0.5° degrees of latitude or longitude at the sub-spacecraft point. This correction corresponds to an

angular offset of 0.02° about the axes of the camera perpendicular to the optical axis. We do not correct for offsets about the optical axis.

In order to extend the absolute navigation derived from the limb to the mosaics at other timesteps where no limb is visible, we find an atmospheric feature (cloud, vortex, or jet) visible at all timesteps and use it as a moving tiepoint. The velocity assigned to the moving tiepoint is taken from Voyager or Hubble Space Telescope (HST) velocity or drift rate measurements. The directions and magnitudes of the corrections are similar for the different timesteps and to the limb-derived correction, suggesting that the pointing offset derived by fitting the limb is a systematic error present through the entire feature track. Using the above techniques, we estimate that the error in our absolute navigation is a few pixels between mosaics at different timesteps, predominantly in the longitude direction. Jupiter's banded clouds and weak meridional winds minimize the uncertainty in latitude. Relative velocities are unaffected by the uncertainty in the velocity of the moving tiepoint. The relative positions of clouds within a mosaic are accurate to one pixel, but the field of zonal velocities derived from pairs of Galileo mosaics is uncertain by an additive constant applied to the entire field.

Navigation of Voyager narrow-angle images was aided by simultaneous wide-angle images that included the planetary limb. The accuracy was limited by the factor of 7.5 difference in focal lengths between the two telescopes. The initial and final uncertainties in our navigation are slightly better than those of Voyager, although we may have larger uncertainties in our derived velocities because of the

shorter time between images. A Galileo wide angle camera would have removed the uncertainty in the position of our mosaics that do not contain Jupiter's limb, but would have been sparingly used with Galileo's limited storage and downlink capabilities.

The calibrated and navigated images are mapped to a uniform grid of latitude and longitude (simple cylindrical projection) and compiled into mosaics. Overlapping pixels are averaged. The scale of the maps is 25-35 km pix^{-1} at the equator and is similar to the spatial resolution of the raw images.

C. True and False Color Mosaics

We used the spectral coverage of the feature tracks to create the true and false color mosaics shown in Fig. 1-4. A color mosaic that approximates Jupiter's appearance at visible wavelengths is constructed by displaying the 756-nm mosaic in red, the 410-nm mosaic in blue, and a linear combination of the previous two in green. We were able to roughly approximate the hues and variance of a true-color HST image using $G = R \times 0.57 + B \times 0.49$, where G, R, and B are the reflectivities in the green, red, and blue mosaics.

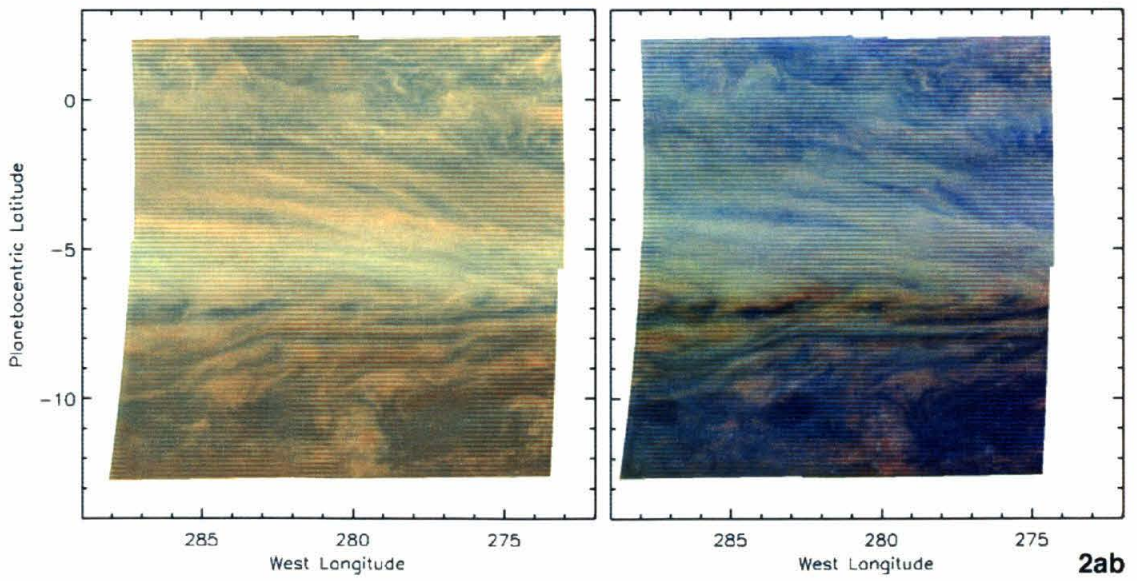
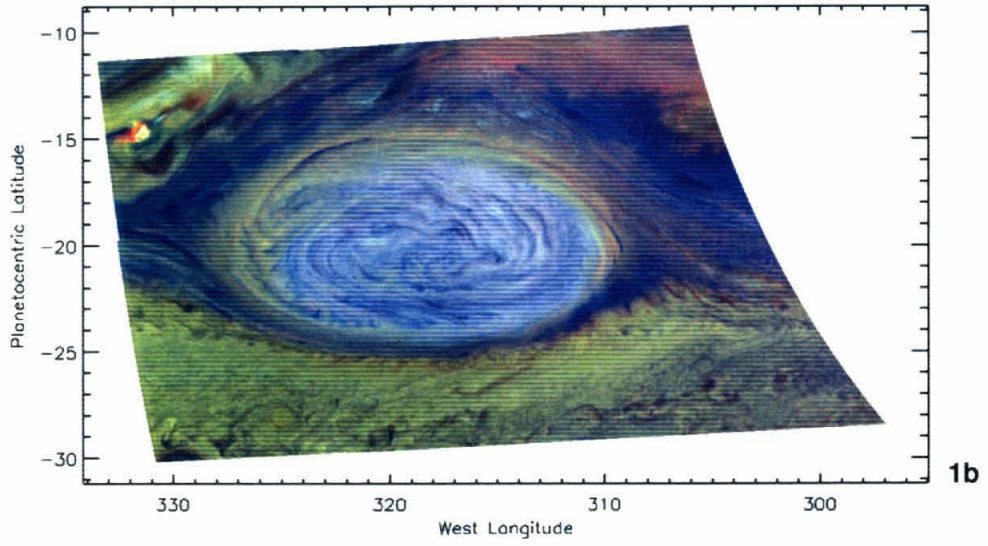
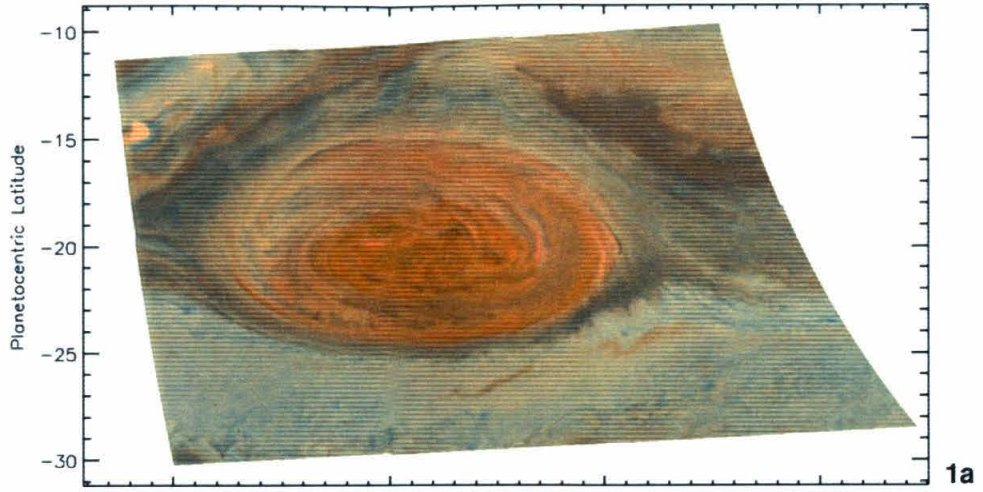
The SSI detects reflected sunlight at three near-infrared wavelengths, two of which are absorbed by methane in Jupiter's atmosphere. A false-color mosaic that reveals information about cloud heights is constructed by displaying the continuum 756-nm mosaic in red, the moderately-absorbed light at 727-nm mosaic in green, and the strongly-absorbed light at 889-nm mosaic in blue. Each mosaic is forced to have the same average brightness and standard deviation. Sunlight at the

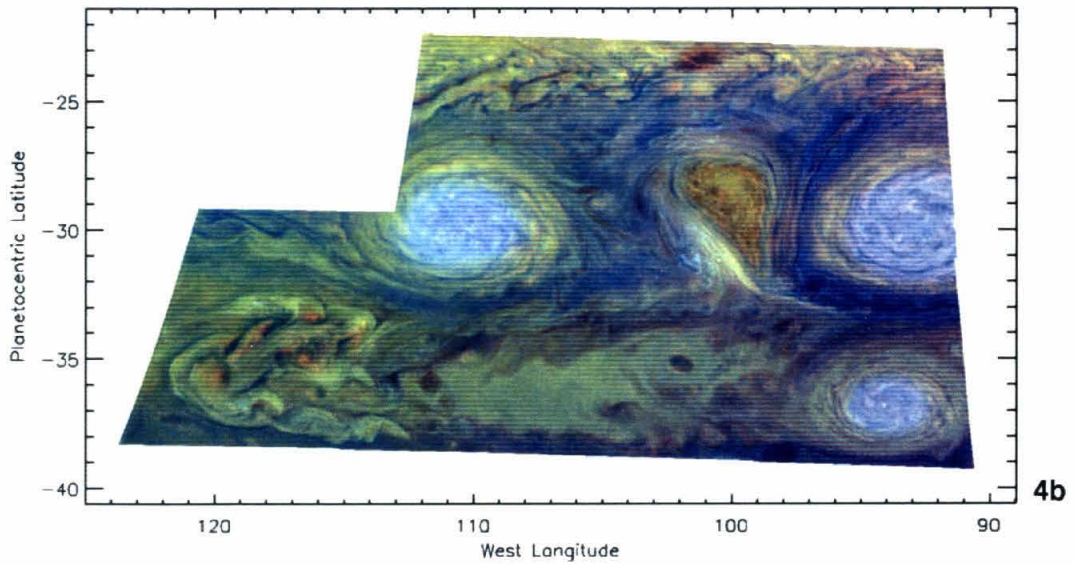
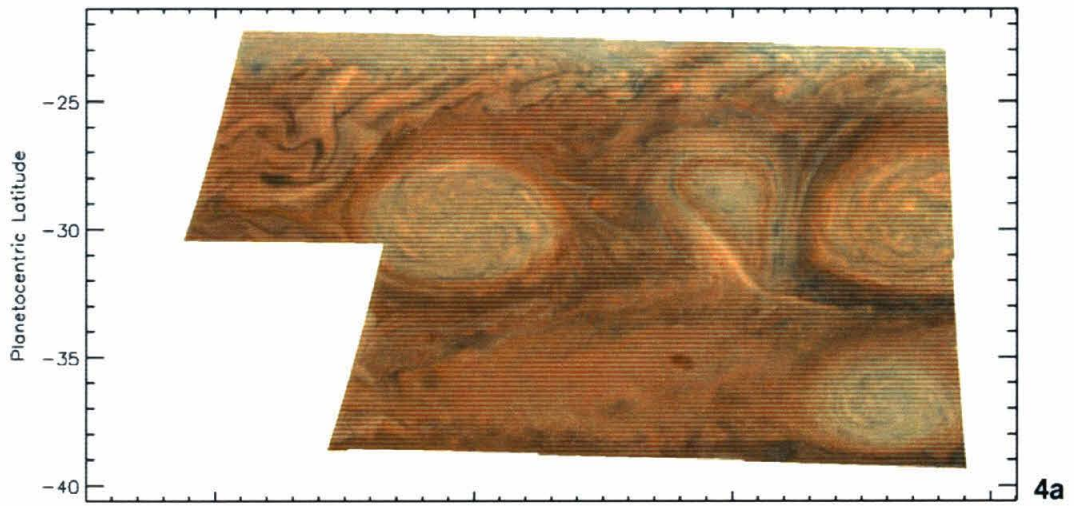
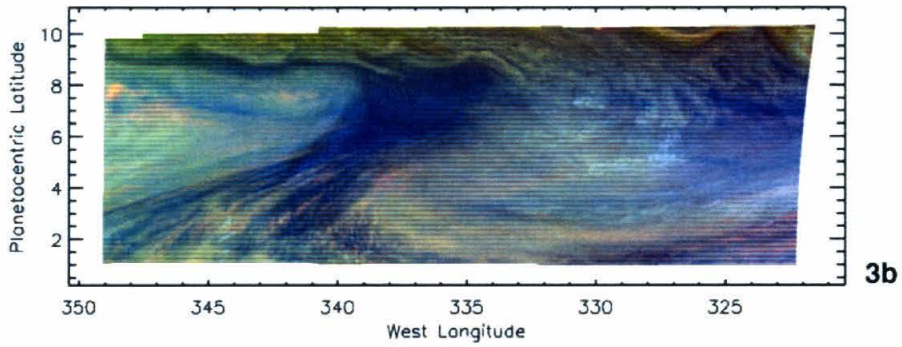
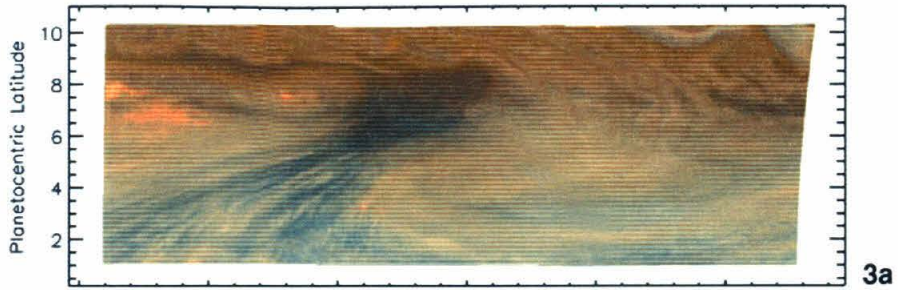
Figure 1. (a) True color 2×3-image mosaic of the Great Red Spot that approximates its appearance at visible wavelengths. It was constructed by displaying the 756-nm mosaic in red, the 410-nm mosaic in blue, and a linear combination of 756 nm and 410 nm in green. One degree of latitude is ~1200 km. (b) False color mosaic constructed by displaying the 756-nm, 727-nm, and 889-nm mosaics in red, green, and blue, respectively. The colors reveal information about the heights and opacities of cloud and haze layers in the atmosphere, as described in the text.

Figure 2. (a) True color 2×2-image mosaic of the south equatorial region. One degree of latitude or longitude is ~1200 km. (b) False color mosaic.

Figure 3. (a) True color 1×3-image mosaic of the north equatorial region. One degree of latitude or longitude is ~1200 km. (b) False color mosaic.

Figure 4. (a) True color 1×3 + 1×2-image mosaic showing White Ovals DE (left) and BC (right), and the cyclonic feature between them. One degree of latitude is ~1200 km. (b) False color 1×2 + 1×3-image mosaic.





continuum wavelength is able to penetrate to the deepest clouds, causing them to appear red. Higher clouds that are also detected at 727 nm appear yellow (red + green). Sunlight at 889 nm is reflected from high, optically thin hazes that appear bluish, or purple if over deep clouds. High, optically thick clouds appear white. Banfield *et al.* (1998) examine the vertical cloud structure in detail.

D. Measuring Wind Velocities

Wind velocities are measured from the mapped 756-nm mosaics by comparing the positions of clouds at different timesteps (e.g., Ingersoll *et al.* 1979). This method assumes that clouds are passive tracers of atmospheric mass motions, not propagating waves (Smith *et al.* 1979). The agreement of Galileo and Voyager wind data with Earth-based measurements with much lower spatial and temporal resolution strongly argues for the validity of this assumption. Jupiter's winds consist of zonal jets that vary in magnitude with latitude, interspersed with vortices of a range of sizes. Vortices locally modify the velocity and direction of neighboring zonal jets, confusing the measurement of jet zonal velocities (Beebe *et al.* 1996). This effect has been overcome in the large Earth-based and Voyager datasets by averaging zonal wind measurements over longitude and time (e.g., Limaye 1986). Because Galileo's observations are restricted in time and longitude, our wind field is an instantaneous sampling of the combined effects of zonal winds and vortices.

Our calculations assume that observed cloud motions represent winds at a pressure level of one bar in Jupiter's atmosphere. This level is an oblate spheroid

with equatorial and polar radii of 71492 km and 66854 km, respectively. Vertical cloud structure derived from Galileo images suggests that the contrast in 756-nm images arises predominantly from opacity variations in a physically thin, lower tropospheric cloud deck at 750 ± 200 mb (Banfield *et al.* 1998). The slightly lower cloud height used in our work introduces negligible errors.

We track cloud motions both manually and automatically. A human operator takes manual measurements by matching cloud features on a pair of maps displayed either side-by-side or blinking. We also use an unsupervised digital correlator developed by Jean Lorre at JPL. This software finds the maximum of a two-dimensional cross-correlation using a rectangular box of pixels and computationally efficient search algorithms. The box size must be large enough to result in a unique correlation. The manual technique yields more accurate measurements in cases where the horizontal scale of velocity variations is smaller than the box size, while the automatic technique produces a finely-sampled, evenly-spaced grid of measurements in a short time.

Most previous measurements of jovian wind velocities were made on image pairs separated in time by one jovian rotation (about ten hours). The larger displacement of the clouds permits a more precise measurement, but in practice the changing morphology of the clouds does not allow accurate determinations of their locations (Mitchell *et al.* 1981). We are more successful in matching cloud features between maps separated by one hour. Maps with a spatial resolution of 30 km pix^{-1}

have a one-pixel measurement uncertainty of 0.8 m s^{-1} and 8 m s^{-1} over ten and one hours, respectively.

III. APPEARANCE AND DYNAMICS

A. The Great Red Spot

The SSI imaged the Great Red Spot (GRS) on June 26, 1996. True and false color mosaics are shown in Fig. 1. The GRS is Jupiter's largest anticyclonic vortex, measuring approximately 22000 km by 11000 km, or 19° longitude by 10° latitude. The GRS is distinguished by its spiral cloud patterns and the relatively cloud-free ring around it. The GRS lies in the South Tropical Zone, an anticyclonic shear zone between the westward jet at 17.5°S at the southern edge of the South Equatorial Belt (SEB), and the eastward jet at 23.7°S at the northern edge of the South Tropical Belt. These jets are deflected around its perimeter. The SEB jet is deflected northward into the eastward south equatorial current, resulting in a cyclonic turbulent zone to the northwest of the GRS characterized by folded cloud filaments with large height variations and rapid, presumably convective outbursts. Such features are apparent in Fig. 1 and are described in Belton *et al.* (1996) and Banfield *et al.* (1998). The northern part of the relatively cloud-free collar around the GRS is wider and more time-variable than its southern counterpart, which is more laminar and featureless.

Wind velocities were measured on maps with time separations of 1.2 and 10.2 hours. Many cloud features changed morphology over the longer interval, limiting its usefulness. The automatic method resulted in more than 10^5 tiepoints

between the 1.2-h pair. These images contain data compression artifacts and required a relatively large (41 pixels on a side or $\sim 1^\circ$) correlation box. The images were over-sampled by shifting the correlation box by 3 pixels between correlations. A tiepoint vector was rejected if a) the correlation coefficient was less than 0.7, b) its length differed from that of adjacent vectors by 30%, or c) its direction differed from that of adjacent vectors by 30° . We determined empirically that these constraints selectively removed spurious correlations. The filtering is performed on over-sampled tiepoints and therefore removes bad tiepoints without smoothing the resulting velocity field. Empirical tests on images of Jupiter showed the effective resolution of the automatic tracking method to be $\sim 0.25^\circ$ when using a 1° box. Manual measurements better resolved the fine structure in the velocity field.

The zonal velocity profile of the GRS is shown in Fig. 5. Automatic measurements within $\pm 1.5^\circ$ degrees longitude of 319° were averaged in 0.25° latitude bins to create the profile. Most bins contain between 100 and 200 measurements. A westward GRS drift rate of 3.9 m s^{-1} derived from recent Earth-based observations (R. Beebe, personal communication) was used to navigate the images and has been subtracted from the profile. The anticyclonic rotation of the GRS is clearly seen. As noted in previous studies, the velocity structure is annular; the velocity peaks within a ring surrounding a more quiescent center (Mitchell *et al.* 1981; Sada *et al.* 1996). Manual measurements indicate a maximum tangential velocity near 150 m s^{-1} both north and south of the center. There are few trackable features between $24\text{--}26^\circ\text{S}$ or north of 14°S . A similarly-constructed meridional

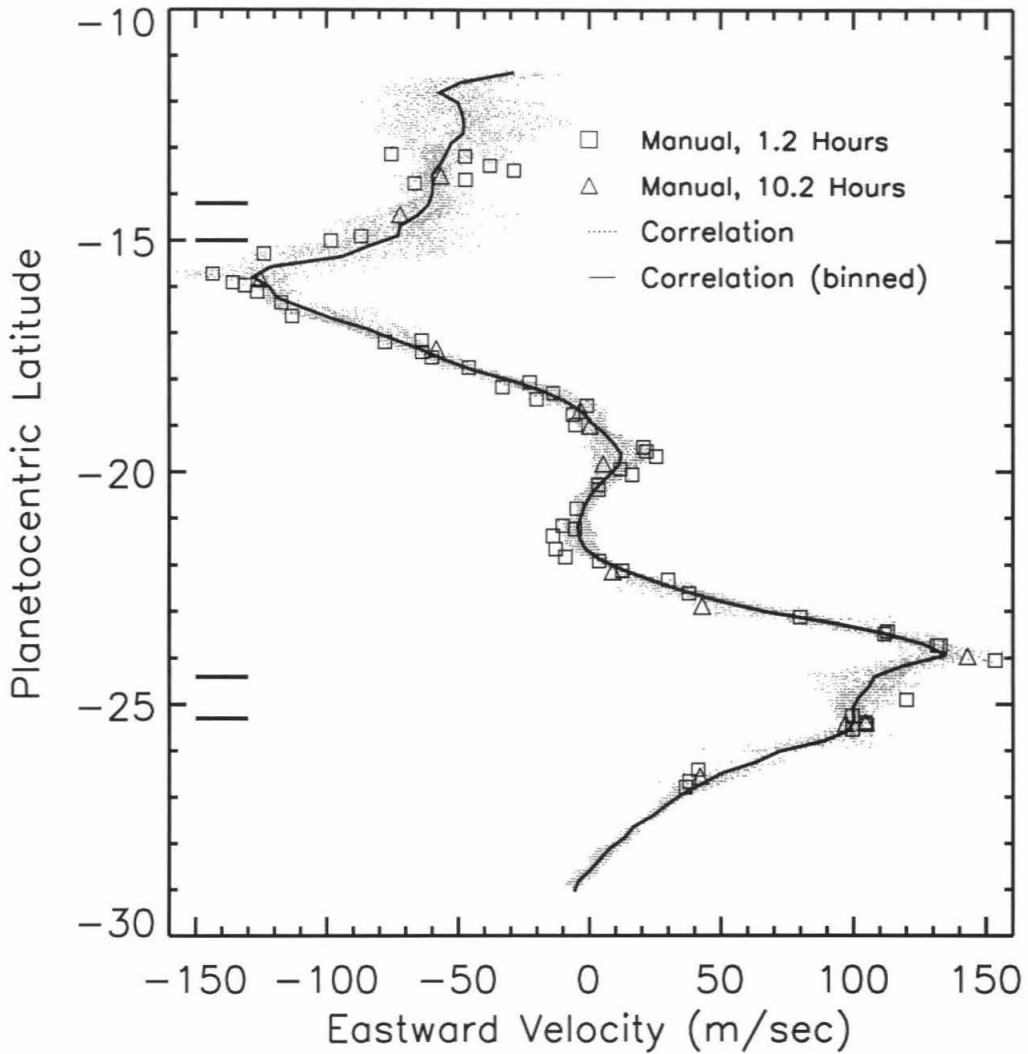


Figure 5. Zonal velocity profile of the Great Red Spot. Automatic measurements within $\pm 1.5^\circ$ longitude of the central meridian of the GRS were averaged in 0.25° latitude bins to create the profile. Manual measurements are also shown. The horizontal lines on the left edge of the plot indicate the visible boundary of the GRS. The inner set of lines marks the extent of the more diffuse clouds that appear associated with the GRS and not with the background flow.

velocity profile centered at 20.3°S has maximum velocities of -94 and 98 m s⁻¹ at 326.8°W and 311°W, respectively.

Figure 6 compares Galileo and Voyager 1 measurements. The velocity distribution along the central meridian of the GRS has not changed significantly since Voyager. Sada *et al.* (1996) found that peak velocities and collar widths differed north and south of the center. However, they constrained the latitude range of their measurements based on a visual determination of the interface between the GRS and the ambient flow, and subsequently may have missed the southern velocity maximum. Without latitude constraints on our measurement area, we find symmetric peak velocities. We believe that both our northern and southern maxima are associated with the circulation of the GRS and not the background flow. Based on a visual estimation of the boundary of the GRS (marked by the horizontal lines in Fig. 5), we find the northern semi-minor axis to be 25% longer (in km) than the southern. The jet maximum in the north is 25% further from the center.

An interesting result of the Galileo measurements is the reversal of the sense of rotation within the center of the GRS implied by Fig. 5. The reversed rotation is cyclonic. We confirmed this result by manually tracking cloud features throughout the central region. Figure 7 reveals that the cyclonic rotation occurs along the wavy interface between the center and collar of the GRS. It has an average velocity near 20 m s⁻¹. Sada *et al.* (1996) found a relatively small cyclonic vortex within the center of the GRS on Voyager 1 and 2 images. Their Voyager 2

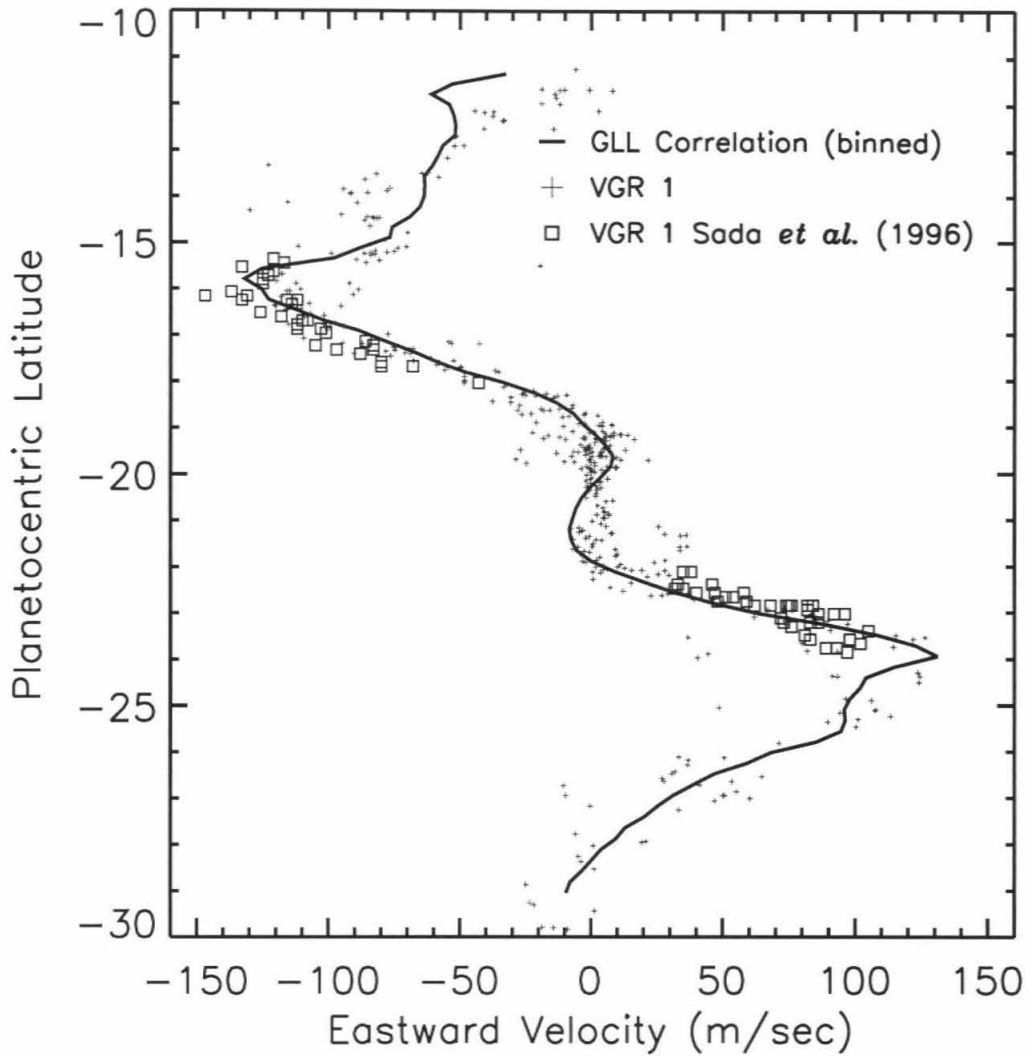


Figure 6. Comparison of the zonal velocity profile of the Great Red Spot between Galileo and Voyager. Manual measurements from Voyager images are shown with those from Galileo. The measurements marked by the (+) symbols were made by the Voyager imaging team and published by Dowling and Ingersoll (1988).

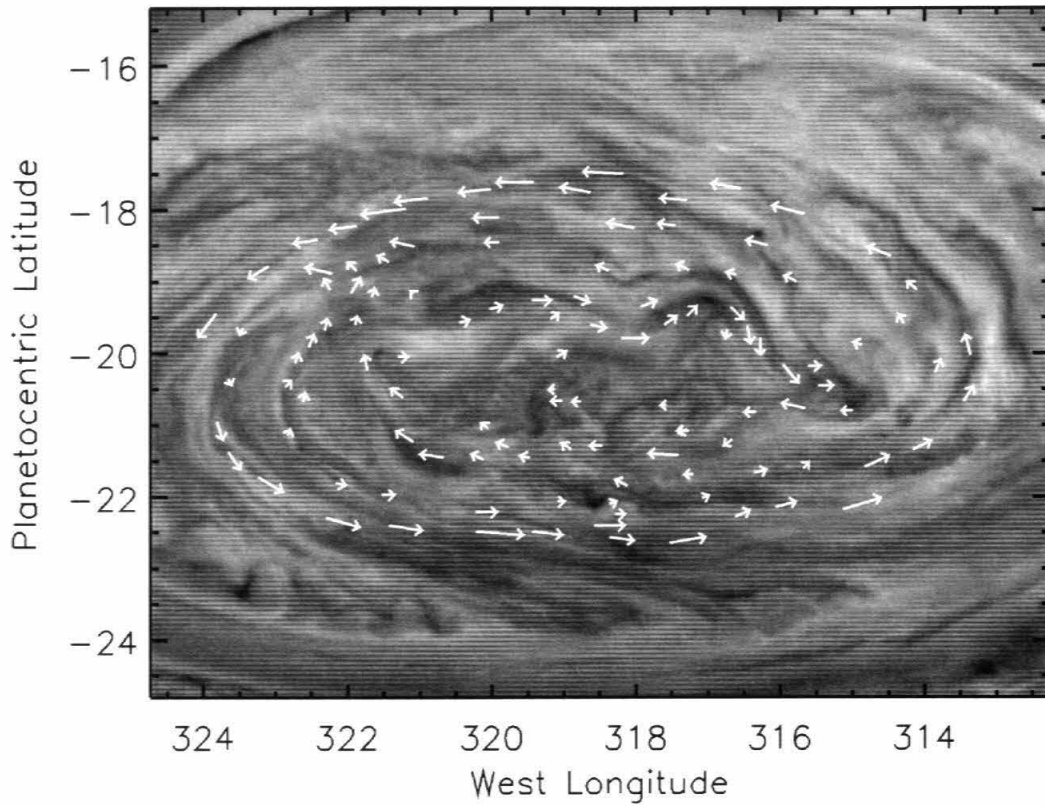


Figure 7. Manual measurements revealing the reversed rotation within the center of the Great Red Spot. The reversed rotation occurs in a narrow current on the wavy boundary between the GRS center and collar. The longest vector shown is 70 m s^{-1} . The vectors are exaggerated by a factor of 2.5 and displayed on a 756-nm mosaic.

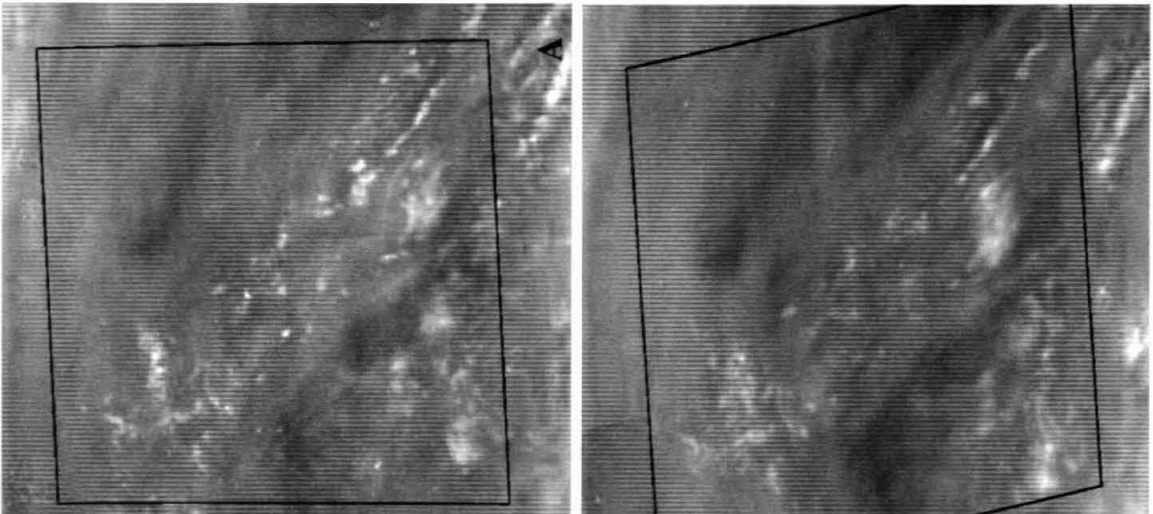
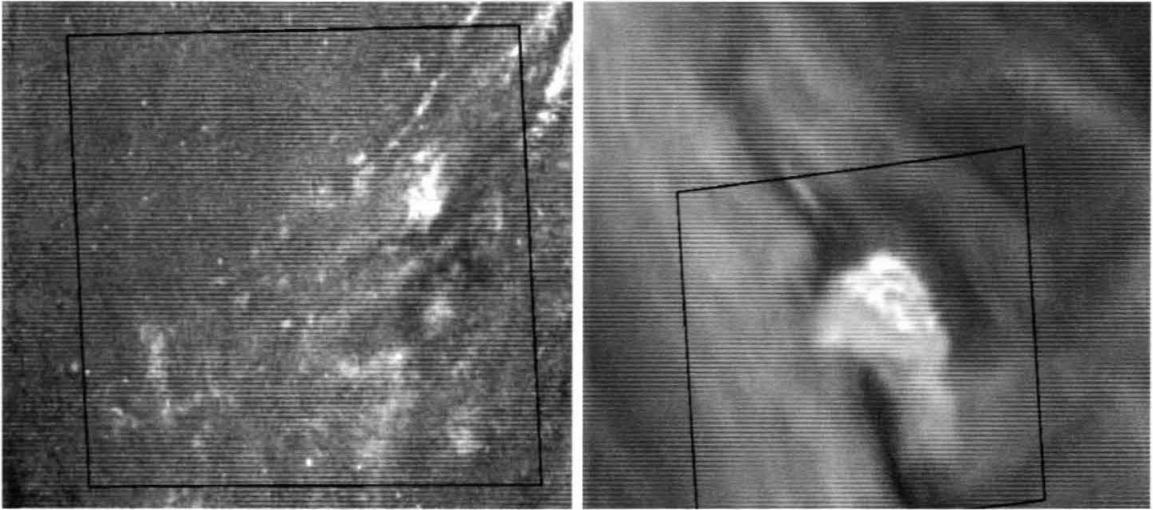
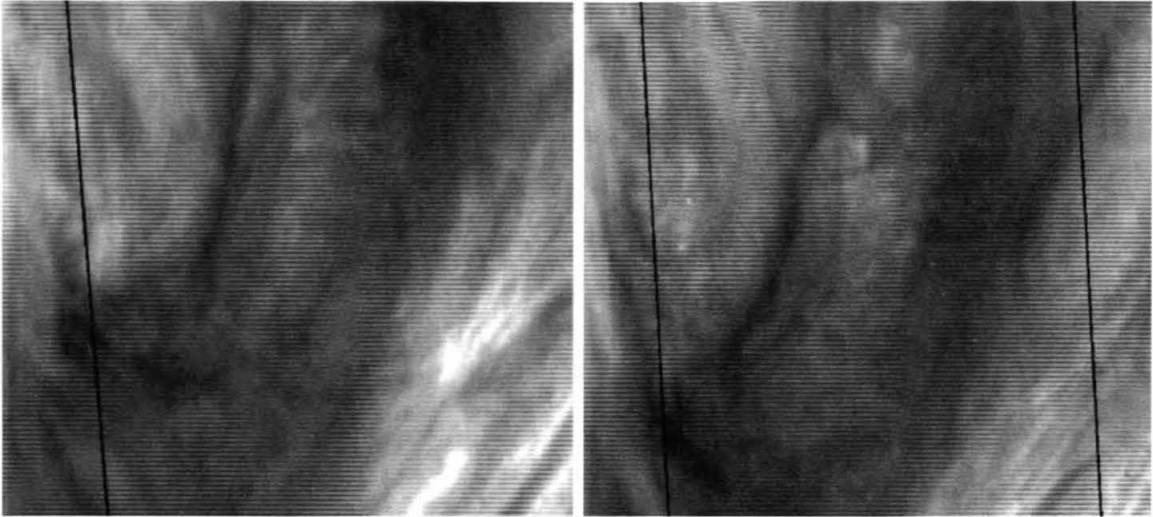
measurements and our own study of Voyager image pairs with one and ten-hour time intervals find cyclonic motion along only the southern center-collar boundary. The complete circuit evident in the Galileo images may be a transient state of the GRS. There is no evidence that our measurements are affected by wave motion or motion at a different height.

Several dynamic features near the Great Red Spot are shown in Fig. 8. Panels A-C show two regions where relatively high clouds are observed to grow and dissipate over timescales of hours. Such rapid changes in cloud morphology were not expected previous to the Galileo mission. Panel D shows a single cloud feature that spans several pressure scale heights from its broad base to its bright peaks. The large and rapid vertical motions implied by these features are strong evidence for moist convection in Jupiter's atmosphere.

B. The Southern Equatorial Region

The SSI observed the region near the south equatorial jet (6°S) on November 5, 1996. True and false color mosaics are shown in Fig. 2. This jet is the boundary between the Equatorial Zone (EZ) to the north and the South Equatorial Belt (SEB) to the south. Nearly pure zonal cloud motion is observed in this region. The sharp velocity maximum within the jet is marked by chevron-shaped cloud streaks. The cyclonic SEB contains patchy clouds in the lower troposphere and circular clearings in the tropospheric haze layer (Banfield *et al.* 1998).

Figure 8 (next page). Dynamic features near the Great Red Spot. Panel A shows a convectively active region northwest of the GRS imaged at 727 nm. The image is approximately 6000 km on a side and is centered at 13°S planetocentric latitude and 314°W longitude. The black frame indicates the region returned with lossless compression. Panel B is the same region imaged 70 minutes later. Over this time scale, most cloud features have advected to the northwest following the local wind field. Some cloud features have changed dramatically in appearance, suggesting rapid vertical motions possibly driven by moist convection at these or deeper levels. Panel C shows the relative height of these features by their brightness at 889 nm. A tall atmospheric structure spanning 30 km in height is shown in Panel D at 756 nm. Panels E and F show a mesoscale wave at 410 nm that dissipates over the 9-hour timescale between the two images. The approximately north-south wave crests, spaced ~300 km apart, are not aligned with the northwest local wind as indicated by other tracers.



Wind velocities were measured using the automatic correlator on a mosaic pair separated by 1.5 h. Because the velocity is predominantly zonal, the measurements were averaged in 0.25° latitude bins to create a zonal velocity profile, shown in Fig. 9. In order to navigate the images, we forced the jet to have a peak velocity of 155 m s^{-1} , as measured on high resolution Voyager and HST images (Beebe *et al.* 1996). The shape of the zonal velocity profile does not depend on the absolute navigation. The jet maximum is at 6.5°S , similar to the location reported in Beebe *et al.* (1989) but slightly southward of that in Limaye (1986). The difference is larger than the uncertainty in fitting Jupiter's limb.

The profile of Limaye (1986) has a maximum jet velocity of 128 m s^{-1} . It represents an average of many measurements on lower-resolution Voyager maps and may not resolve the narrow jet maximum. In order to confirm the peak speed of the jet, we processed two Voyager 1, narrow-angle, orange-filter images taken 9.4 h apart, each having a limb for absolute navigation. The spatial resolution is similar to that of the Galileo observations. We find a peak speed of 150 m s^{-1} . If this is also the speed of the jet in the Galileo era, it implies that the EZ near 0° latitude has slowed by more than 20 m s^{-1} . The difference in zonal velocity between the EZ and the jet maximum of 87 m s^{-1} in the Galileo data is greater than the difference of 60 m s^{-1} in our Voyager data and the difference of 63 m s^{-1} in the Voyager data of Beebe *et al.* (1989). The slower EZ is within the range of values measured by Beebe *et al.* (1996), and may signify a temporally fluctuating EZ.

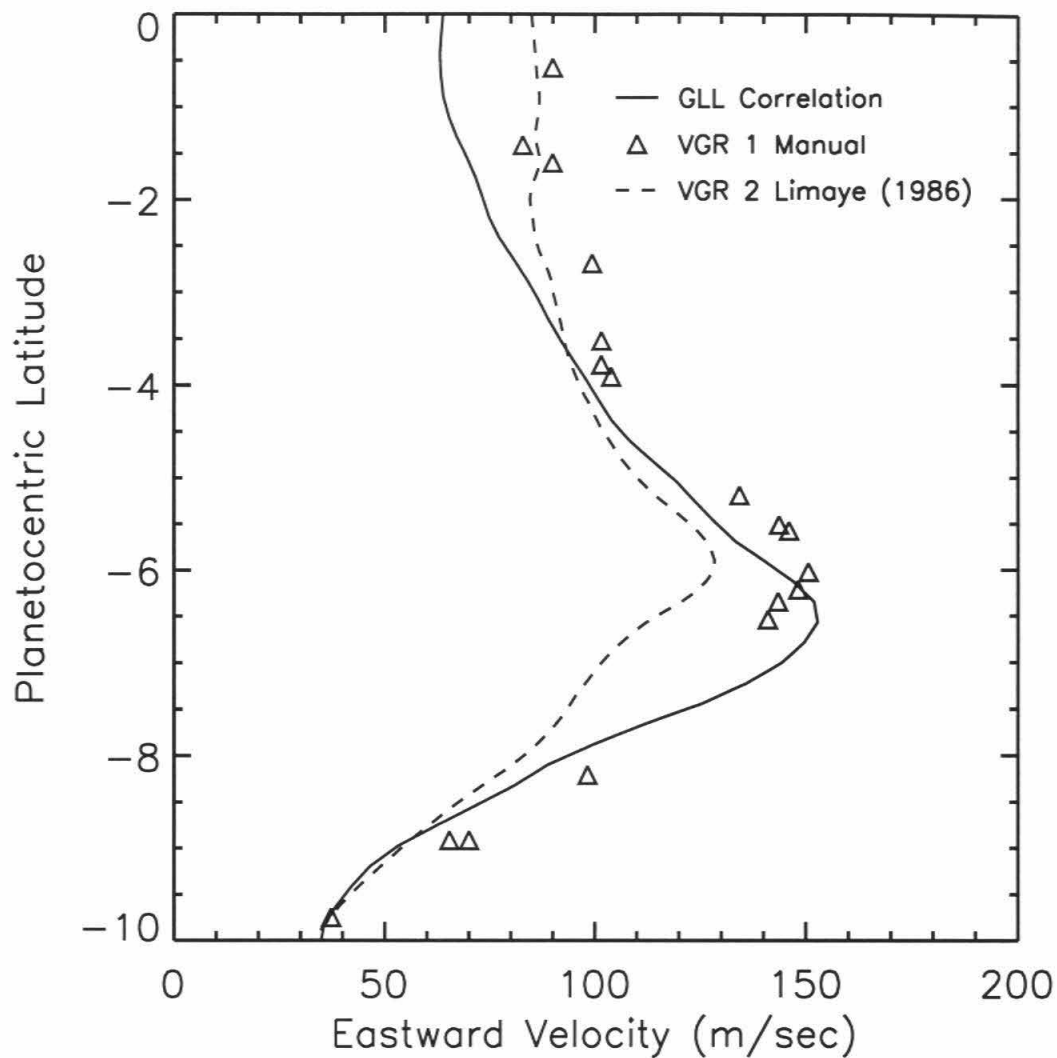


Figure 9. Comparison of the zonal velocity profile of the south equatorial region between Galileo and Voyager. The zonal velocity difference between 0°S and 6.5°S is at least 20 m s⁻¹ larger in the Galileo measurements.

Galileo may be detecting motion at a different altitude than Voyager, but no evidence for vertical shear in horizontal velocity is seen.

C. The Northern Equatorial Region

The SSI observed the region near the north equatorial current (6°N) on December 17, 1996. True and false color mosaics are shown in Fig. 3. The observations follow a “5- μm hotspot” similar to the Galileo Probe entry site. The relatively dark hotspot is bordered on the north by the North Equatorial Belt (NEB). Rotational motion, time-variable clouds, waves, and multi-level cloud decks make this region dynamically complex.

Throughout this century, the northern half of the EZ has been characterized by a series of regularly spaced ($\sim 30^\circ$ longitude) “dark projections” interleaved with bright white, oval-shaped or plume-shaped clouds (Reese and Beebe 1976; Rogers 1995). Figure 3 shows one dark projection and one large, oval-shaped cloud immediately to the southeast. These dark projections are regions of decreased cloud opacity and appear as bright spots on 5- μm thermal emission images. Usually, only the southern and western boundaries of the oval-shaped clouds are well-defined. The hotspots translate at the speed of the north equatorial current ($\sim 100 \text{ m s}^{-1}$). There are temporal variations in individual hotspots, but the spatial pattern is stable over months to years (Ortiz *et al.* 1998). Bright, presumably convective plumes sometimes appear west of the hotspots, producing white clouds expanding to the southwest for periods of months or years (Reese and Beebe 1976; Smith *et al.* 1979). The relationship between the plumes and the hotspots is

complex and not well understood. The hotspot observed by the SSI significantly increased in brightness at 5 μm during the three weeks before Galileo's observation (Orton *et al.* 1997).

Figure 10 is a map of wind vectors created by interpolating 1.1-h measurements from our automatic correlator to a coarse grid. The measurements were transformed to the reference frame of the northern edge of the hotspot by subtracting a zonal velocity of 78 m s^{-1} from all points. The presence of multi-level cloud layers, vertical wind shear, and featureless cloud streaks made tracking clouds difficult both automatically and by eye. The white cloud material west of the hotspot is rotating cyclonically and moves eastward 40 m s^{-1} faster than the hotspot. We detect a strong ($30\text{-}50 \text{ m s}^{-1}$) southwest-to-northeast current along the streaks leading towards the hotspot. The current appears to be associated with an anticyclonically rotating, oval-shaped cloud southeast of the hotspot. There is little detected motion away from the hotspot, however.

The depleted volatile abundances measured by the Galileo Probe within a different hotspot may be the result of local meteorology (Niemann *et al.* 1996, Showman and Ingersoll 1998), including horizontal convergence and downwelling of dry air over hotspots. There are two possible interpretations of our measurements. The first is massive convergence and downwelling into the hotspot indicated by the northeast flow into the hotspot and the lack of cloud motion away from the hotspot. If jovian air enters along the southern boundary of the $5000 \times 2000\text{-km}$ hotspot at 40 m s^{-1} , the convergence rate is 10^{-5} s^{-1} . The implied

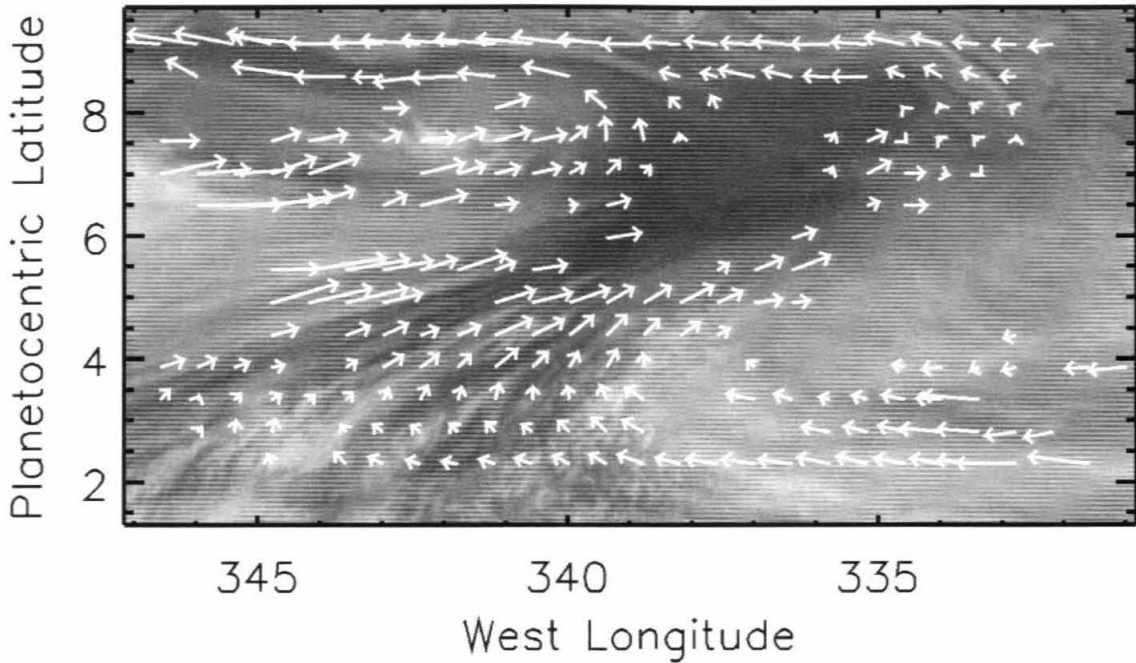


Figure 10. Wind measurements near the north equatorial jet. The dark feature is a 5-micron hotspot similar to the Galileo Probe entry site. The wind vectors are plotted in a reference frame fixed to the hotspot. The northeast current towards the hotspot has a peak magnitude of 50 m s^{-1} . The vectors are exaggerated by a factor of 6 and displayed on a 756-nm mosaic.

vertical velocity is 1 m s^{-1} if the vertical divergence is spread over 100 km. These numbers are highly uncertain, however.

The alternative interpretation is that a rotating, oval-shaped cloud is present southeast of the hotspot and that trackable features exist only on its southern and western edges. The rotation of these ovals, with the hotspots lying in the intervening shear zones, has been inferred from their shape (R. Beebe, personal communication), but not detected until the present study. From our images, it appears that trackable cloud features evaporate as they approach the hotspot on the western edge of the rotating oval. Features on the northern edge are obscured by the diffuse NEB clouds that are drifting southwest over the oval. In this interpretation, most of the convergence qualitatively seen in Fig. 10 would be an illusion, although some downwelling may be responsible for the evaporation of the cloud streaks.

It is interesting to compare the cloud morphologies of the northern and southern edges of the EZ. The cloud morphology near the jet south of the equator (Fig. 2) resembles the pattern of hotspots and plume-like clouds seen north of the equator (Fig. 3), but at a smaller scale and inverted with respect to latitude. The size and longitudinal wavenumber of hotspots north of the equator has been observed to vary with time (Reese and Beebe 1976; Ortiz *et al.* 1998). Historical reports indicate that the appearance of the southern boundary of the EZ was similar to the present northern boundary before 1910 (Rogers 1995). Perhaps

similar, but time-variable structures exist at the northern and southern boundaries of the EZ and have properties determined by the velocities of the bounding jets.

D. The White Ovals

The SSI observed the region near two of the White Ovals on February 19, 1997. True and false color mosaics are shown in Fig. 4. The anticyclonic White Ovals DE (110.5°W) and BC (92.5°W) are separated by a teardrop-shaped cyclonic vortex. The mosaics also show a smaller anticyclonic vortex at (37°S , 94°W) and a turbulent cyclonic vortex at (35°S , 118°W). The ovals DE and BC have been studied since their origin in 1939. Their recent behavior is reported by Simon *et al.* (1998). The ovals formed within the South Temperate Zone (STZ), but slowly have become embedded within the southern portion of the South Temperate Belt (STB). The westward jet at 29°S , which is the southern boundary of the STB, is deflected northward around the ovals. The centroid of the teardrop-shaped vortex lies within the STB, bordered to the north by an eastward jet at 23.7°S . The cyclonic South-STB and the anticyclonic South-STZ lie poleward of the White Ovals.

Figure 11 is a map of wind vectors created by interpolating 1.4-h measurements from our automatic correlator to a coarse grid. The eastward jets at 23.7°S and 32.6°S are apparent in the map. The westward jet normally at 29°S has been deflected north of BC off the right edge of the mosaic. It appears to be completely deflected southward between the cyclonic feature and BC, re-connecting with the eastward jet at 32.6°S . The jet at 29°S is absent between ovals

BC and DE. The cyclonic feature interacts more strongly with the eastward jet south of the White Ovals than similar features did in the Voyager era (Rogers 1995). This interaction may be a result of the current compact configuration of vortices (Simon *et al.* 1998). The northern extent of the jet at 32.6°S impinges on the cyclonic feature, creating bright thick clouds and deflecting that jet northward and around the cyclonic feature.

Measurements within $\pm 1^{\circ}$ longitude of the central meridian of oval DE were averaged in 0.25° latitude bins to create the zonal velocity profile shown in Fig. 12. Manual measurements were taken to verify the shape of the profile near the maxima. The northern and southern maxima are -82 and 108 m s^{-1} , respectively. A symmetric profile is possible within the errors introduced by the uncertainty in absolute navigation. As noted in previous studies (Mitchell *et al.* 1981), there is no evidence (from appearance or wind measurements) for a quiescent central region as seen in the GRS profile. Measured velocities along the western and eastern edges of the cyclonic feature reach 84 and 104 m s^{-1} , respectively.

IV. DISCUSSION AND CONCLUSIONS

The Galileo imaging dataset of Jupiter's atmosphere is compact and well-designed for the study of cloud motions and vertical structure with high spatial and temporal resolutions. We have presented new velocity measurements near Jupiter's Great Red Spot, the equatorial region, and two White Ovals. The overall similarity of our results to Voyager measurements attests to the stability of jets and vortices

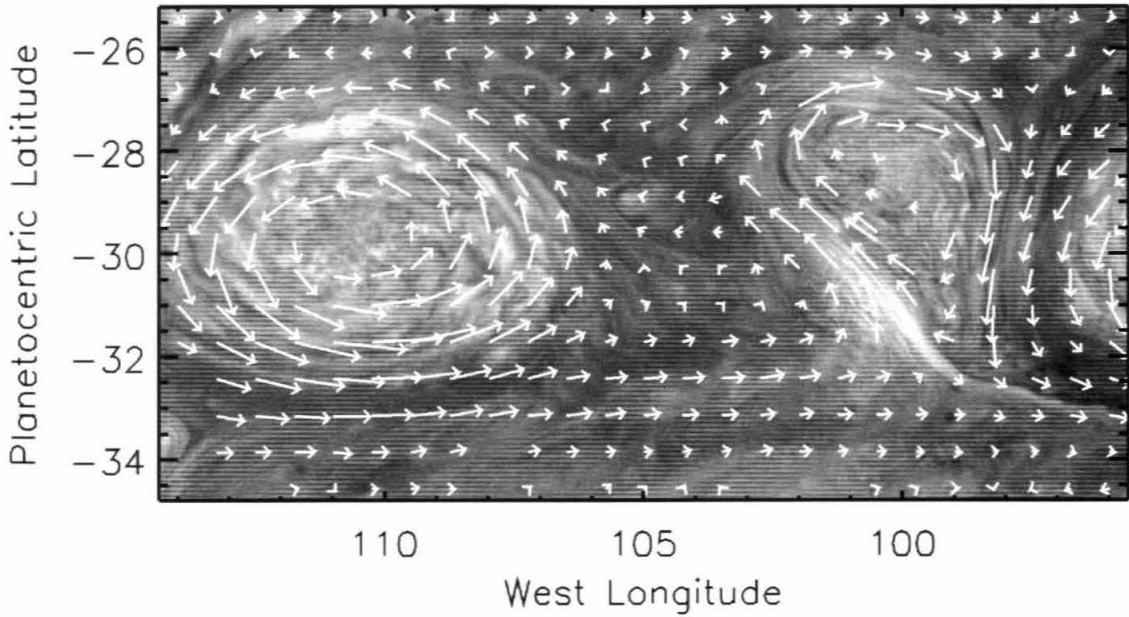


Figure 11. Wind measurements of White Oval DE and the neighboring cyclonic vortex. Both features have peak tangential velocities near 100 m s^{-1} . The vectors are exaggerated by a factor of 2.5 and displayed on a 756-nm mosaic.

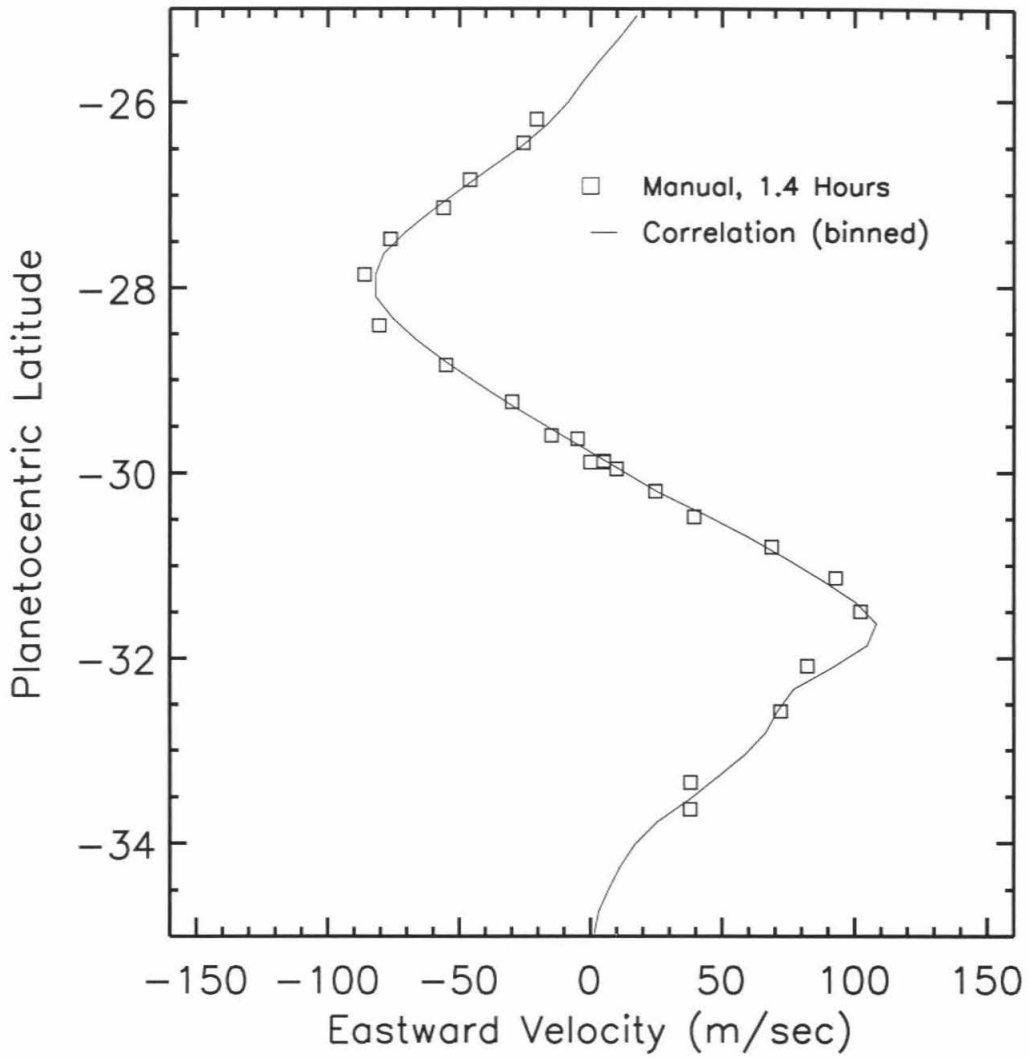


Figure 12. Zonal velocity profile of White Oval DE. Automatic measurements within $\pm 1^\circ$ longitude of the central meridian of DE were averaged in 0.25° latitude bins to create the profile. Manual measurements are also shown.

in Jupiter's atmosphere. The counter-rotating interior of the GRS and the dynamics near a Galileo Probe entry site analog are important new results. Galileo's unique ability to image at near-infrared wavelengths provides the third dimension (Banfield *et al.* 1998).

The results and interpretations presented here are not exhaustive. Many images contain temporally variable clouds, multiple cloud layers, and waves. Careful work comparing cloud motions with vertical structure derived from SSI and other Galileo instruments will result in better constraints on vertical motions and vertical shear in the wind field. Maps of vorticity and horizontal divergence will help determine the connection between the dynamics of the visible cloud deck and the jovian interior.

The Galileo imaging dataset also holds information about the dynamics of giant planet atmospheres that can be unlocked only with careful numerical modeling. Appropriate questions for future modeling work include: 1) Under what conditions is an annular vortex like the Great Red Spot stable? 2) Is the presence of a counter-rotating center possible? 3) Can a series of large (semi-major axis near 20000 km) anticyclonic ovals be reproduced in models close to the equator? 4) What leads to the presumably convective activity in cyclonic regions such as northwest of the GRS and west of hotspots? Several groups are already using Earth-based, Galileo Orbiter, and Probe data to understand the nature of 5- μm hotspots. Many more questions will certainly be raised by the remaining Galileo observations.

Acknowledgments: We thank the Multimission Image Processing Lab at JPL, and especially Helen Mortensen, for their support of the imaging team. Joe Spitale and Lisa Gaskell helped with the image processing at Caltech. Adam Showman, James Cho, Sarah Stewart, and two anonymous reviewers provided helpful comments. This work was supported by NASA's Planetary Atmospheres Program and the Galileo Project.

References

- Banfield, D., P. J. Gierasch, M. Bell, E. Ustinov, A. P. Ingersoll, A. R. Vasavada, R. A. West, and M. J. S. Belton 1998. Jupiter's cloud structure from Galileo imaging data. *Icarus*, in press.
- Beebe, R. F., G. S. Orton, and R. A. West 1989. Time-variable nature of the jovian cloud properties and thermal structure: An observational perspective. In *Time-Variable Phenomenon in the Jovian System* (M. J. S. Belton, R. A. West, and J. Rahe, Eds.), pp. 245-288. NASA SP-494.
- Beebe, R. F., A. A. Simon, and L. F. Huber 1996. Comparison of Galileo probe and Earth-based translation rates of Jupiter's equatorial clouds. *Science* **272**, 841.
- Belton, M. J. S., and 22 colleagues 1992. The Galileo solid-state imaging experiment. *Space Sci. Rev.* **60**, 413-455.
- Belton, M. J. S., and 33 colleagues 1996. Galileo's first images of Jupiter and the Galilean satellites. *Science* **274**, 377-385.
- Dowling, T. E., and A. P. Ingersoll 1988. Potential vorticity and layer thickness variations in the flow around Jupiter's Great Red Spot and White Oval BC. *J. Atmos. Sci.* **45**, 1380-1396.
- Ingersoll, A. P., R. F. Beebe, S. A. Collins, G. E. Hunt, J. L. Mitchell, P. Muller, B. A. Smith, and R. J. Terrile 1979. Zonal velocity and texture in the jovian atmosphere inferred from Voyager images. *Nature* **280**, 773-775.

- Klaasen, K. P., M. J. S. Belton, H. H. Breneman, A. S. McEwen, M. E. Davies, R. J. Sullivan, C. R. Chapman, G. Neukum, and C. M. Heffernan 1997. Inflight performance-characteristics, calibration, and utilization of the Galileo solid-state imaging camera. *Opt. Eng.* **36**, 3001-3027.
- Limaye, S. S. 1986. Jupiter: New estimates of the mean zonal flow at the cloud level. *Icarus* **65**, 335-352.
- Lindal, G. F., and 11 colleagues 1981. The atmosphere of Jupiter: An analysis of the Voyager radio occultation measurements. *J. Geophys. Res.* **86**, 8721-8727.
- Minnaert, M. 1941. The reciprocity principle in lunar photometry. *Astrophys. J.* **93**, 403-410.
- Mitchell, J. L., R. F. Beebe, A. P. Ingersoll, and G. W. Garneau 1981. Flow fields within Jupiter's Great Red Spot and White Oval BC. *J. Geophys. Res.* **86**, 8751-8757.
- Niemann, H. B., and 12 colleagues 1996. The Galileo probe mass spectrometer: Composition of Jupiter's atmosphere. *Science* **272**, 846-849.
- Ortiz, J. L., G. S. Orton, S. T. Stewart, and B. M. Fisher 1998. Time evolution and longitudinal persistence of 5- μ m hot spots at the Galileo Probe entry latitude. *J. Geophys. Res.*, in press.
- Orton, G. S., and 17 colleagues 1997. Atmospheric structure of Jupiter from radiometric observations of the Galileo Photopolarimeter-Radiometer (PPR) and ancillary earth-based observations. *Bull.--Am. Astron. Soc.* **29**, 1005.

- Reese, E., and R. Beebe 1976. Velocity variations of an equatorial plume throughout a jovian year. *Icarus* **29**, 225-229.
- Rogers, J. H. 1995. *The Giant Planet Jupiter*, Cambridge Univ. Press, Cambridge, UK.
- Sada, P. V., R. F. Beebe, and B. J. Conrath 1996. Comparison of the structure and dynamics of Jupiter's Great Red Spot between the Voyager 1 and 2 encounters. *Icarus* **199**, 311-335.
- Showman, A. P., and A. P. Ingersoll 1998. Interpretation of Galileo probe data and implications for Jupiter's dry downdrafts. *Icarus*, in press.
- Simon, A. A., R. F. Beebe, P. J. Gierasch, A. R. Vasavada, M. J. S. Belton, and the Galileo Imaging Team, 1998. Global context of the Galileo-E6 observations of Jupiter's White Ovals. *Icarus*, in press.
- Smith, B. A., and 21 colleagues 1979. The Jupiter system through the eyes of Voyager 1. *Science* **204**, 951-972.